Astronomy & Astrophysics manuscript no. sn2011dh-2-astro-ph-v1
January 14, 2016
©ESO 2016

arXiv:1408.0731v1 [astro-ph.SR] 4 Aug 2014

The Type IIb SN 2011dh - 2 years of observations and modelling of the lightcurves.

M. Ergon[1], A. Jerkstrand[2], J. Sollerman[1], N. Elias-Rosa[3], C. Fransson[1], M. Fraser[4,2], A. Pastorello[3], R. Kotak[2], S. Taubenberger[5], L. Tomasella[3], S. Valenti[6,7], S. Benetti[3], G. Helou[8], M.M. Kasliwal[9], J. Maund[2], S.J. Smartt[2], and J. Spyromilio[10]

[1] The Oskar Klein Centre, Department of Astronomy, AlbaNova, Stockholm University, 106 91 Stockholm, Sweden
[2] Astrophysics Research Centre, School of Mathematics and Physics, Queens University Belfast, Belfast, BT7 1NN, UK
[3] INAF, Osservatorio Astronomico di Padova, vicolo dell'Osservatorio n. 5, 35122 Padua, Italy
[4] Institute of Astronomy, University of Cambridge, Madingley Road, Cambridge, CB3 0HA
[5] Max-Planck-Institut für Astrophysik, Karl-Schwarzschild-Str. 1, D-85741 Garching, Germany
[6] Las Cumbres Observatory Global Telescope Network, 6740 Cortona Dr., Suite 102, Goleta, CA 93117, USA
[7] Department of Physics, University of California, Santa Barbara, Broida Hall, Mail Code 9530, Santa Barbara, CA 93106-9530, USA
[8] Infrared Processing and Analysis Center, California Institute of Technology, Pasadena, CA 91125, USA
[9] Observatories of the Carnegie Institution for Science, 813 Santa Barbara St, Pasadena, CA 91101, USA
[10] ESO, Karl-Schwarzschild-Strasse 2, 85748 Garching, Germany

Submitted to Astronomy and Astrophysics

ABSTRACT

We present optical and near-infrared (NIR) photometry and spectroscopy as well as modelling of the lightcurves of the Type IIb supernova (SN) 2011dh. Our extensive dataset spans 2 years, and complemented with Spitzer mid-infrared (MIR) data, we use it to build a 3-732 days optical to MIR bolometric lightcurve. To model the <400 days bolometric lightcurve we use a hydrodynamical model grid, which allows us to determine the errors in the derived quantities, and a bolometric correction determined with steady-state NLTE modelling. We obtain similar results using the <100 days and <400 days bolometric lightcurves, and using the latter we find a helium core mass of $3.1^{+0.7}_{-0.4}$ $M_\odot$ for SN 2011dh. We present 100-500 days bolometric and photometric lightcurves for the Jerkstrand et al. (2014) steady-state NLTE models. The preferred 12 $M_\odot$ (initial mass) model, presented and found to give a good agreement with observed nebular spectra in Jerkstrand et al. (2014), shows a good overall agreement with the observed lightcurves, although some discrepancies exist. Time-dependent NLTE modelling shows that after 600 days a steady-state assumption is no longer valid. The radioactive energy deposition in this phase is likely dominated by the positrons emitted in the decay of ^{56}Co, but what energy source is dominating the emitted flux is unclear. We find an excess in the K and the MIR bands developing between 100 and 250 days, during which an increase in the optical decline rate is also observed. A local origin of the excess is suggested by the depth of the He I 20581 Å absorption. Steady-state NLTE models with a modest dust opacity in the core (τ = 0.44), turned on during this period, reproduce the observed behaviour, but an additional excess in the Spitzer 4.5 μm band remains. CO first overtone band emission is detected at 206 days, and possibly at 89 days, and assuming the additional excess to be dominated by CO fundamental band emission, we find fundamental to first overtone band ratios considerably higher than observed in SN 1987A. The profiles of the [O I] 6300 Å and Mg I] 4571 Å lines show a remarkable similarity, suggesting these lines to originate mainly from the O/Ne/Mg zone, and using small scale fluctuations in the line profiles we estimate a filling factor of $\lesssim$0.07 for the emitting material. This paper concludes our extensive observational and modelling work on SN 2011dh. The results from hydrodynamical modelling, steady-state NLTE modelling and stellar evolutionary progenitor analysis are all consistent, and suggest an initial mass of ~12 $M_\odot$ for the progenitor. We also extend our analysis to SNe 1993J and 2008ax, and the initial masses of $\lesssim$15 $M_\odot$ found for SNe 2011dh, 1993J and 2008ax, by hydrodynamical modelling and steady-state NLTE modelling of nebular spectra (Jerkstrand et al. 2014), suggest that all of these Type IIb SNe originates from binary systems, as previously established for SN 1993J.

Key words. supernovae: general — supernovae: individual (SN 2011dh) — supernovae: individual (SN 1993J) — supernovae: individual (SN 2008ax) — galaxies: individual (M51)

1. Introduction

Type IIb supernovae (SNe) are observationally characterized by a transition from Type II (with hydrogen lines) at early times to Type Ib (without hydrogen lines but with helium lines) at later times. The physical interpretation is that these SNe arise from stars that have lost most of their hydrogen envelope, either through stellar winds or interaction with a binary companion. Which of these production channels dominates is still debated but for SN 1993J, the prime example of such a SN, a companion star was detected by direct observations (Maund et al. 2004; Fox et al. 2014). The evolution of this binary system has been successfully modelled (Podsiadlowski et al. 1993; Stancliffe & Eldridge 2009), and it is widely accepted that the companion was responsible for the removal of the hydrogen envelope. Bright, nearby Type IIb SNe as 1993J, 2008ax and the recent 2011dh are essential to improve our understanding of this class. Observations of the progenitor star in pre-explosion images, a search

for the companion star when the SN has faded and multi-method modelling of high quality data, all provide important clues to the nature of Type IIb SNe and their progenitor stars.

In this paper we present an extensive optical and near-infrared (NIR) dataset, covering nearly two years, that we have obtained for SN 2011dh. The first 100 days of this dataset have been presented in Ergon et al. (2014a, hereafter E14a). Detailed hydrodynamical modelling of the SN using those data were presented in Bersten et al. (2012, hereafter B12) and steady-state NLTE modelling of nebular spectra in Jerkstrand et al. (2014, hereafter J14). Identification and analysis of the plausible progenitor star was presented in Maund et al. (2011, hereafter M11), and confirmation of the progenitor identification through its disappearance in E14a.

SN 2011dh was discovered on 2011 May 31.893 UT (Griga et al. 2011; Arcavi et al. 2011) in the nearby galaxy M51 at a distance of 7.8 Mpc (E14a). The SN has been extensively monitored from X-ray to radio wavelengths by several teams. Most observations cover the 3-100 days period, but late time data have been published by Tsvetkov et al. (2012), Van Dyk et al. (2013), Sahu et al. (2013), Shivvers et al. (2013) and Helou et al. (2013). As in E14a we focus on the ultra-violet (UV) to mid-infrared (MIR) emission. The explosion epoch (May 31.5 UT), the distance to M51 ($7.8^{+1.1}_{-0.9}$ Mpc) and the interstellar line-of-sight extinction towards the SN ($E(B\text{-}V)$=$0.07^{+0.07}_{-0.04}$ mag) used in this paper, are all adopted from E14a. The phase of the SN is expressed relative to this explosion epoch throughout the paper.

The nature of the progenitor star has been a key issue since the identification of a yellow supergiant in pre-explosion images, coincident with the SN (M11; Van Dyk et al. 2011). Recent progress in modelling of the SN (B12; J14; Shivvers et al. 2013), and the disappearance of the progenitor candidate (E14a; Van Dyk et al. 2013), strengthens the hypothesis that the progenitor was a yellow supergiant of moderate mass, as was originally proposed in M11. In this paper we present further modelling in support of this hypothesis. As shown in Benvenuto et al. (2013), a binary interaction scenario that reproduces the observed and modelled properties of the yellow supergiant is possible. Hubble Space Telescope (HST) observations that could detect or set useful constraints on the presence of a companion star are scheduled for Cycle 21.

The paper is organized as follows. In Sect. 2 and 3 we present and analyse our photometric and spectroscopic observations, respectively, and compare these to SNe 1993J and 2008ax. In Sect. 4 we model the lightcurves and in Sect. 5 we discuss the MIR evolution, our results on the nature of the progenitor star, and the implication of these on our understanding of Type IIb SNe. Finally, we conclude and summarize our results in Sect. 6.

2. Photometry

In E14a we presented our <100 days observations, and analysis and comparison to SNe 1993J and 2008ax. Here we present observations spanning 100-732 days in the optical, 100-380 days in the NIR and 100-1061 days in the MIR, and a continuation of the analysis and the comparison, focusing on the >100 days data. Hydrodynamical and steady-state NLTE modelling of these data are presented in Sect. 4. As discussed in E14a, the systematic errors stemming from the uncertainties in distance and extinction are large for all three SNe, which should be kept in mind when absolute quantities are compared. For SNe 1993J and 2008ax we adopt the same values and error bars for the distance and extinction as in E14a. The references for the photometric data of SNe 1993J and 2008ax used in the comparison are the same as specified in E14a. We note that the lack of S-corrected photometry for SN 1993J complicates the comparison, whereas for SN 2008ax, the S-corrected Johnson-Cousins (JC) photometry by Taubenberger et al. (2011) agrees reasonably well with the JC photometry by Tsvetkov et al. (2009).

2.1. Observations

The >100 days data were obtained with the Liverpool Telescope (LT), the Nordic Optical Telescope (NOT), Telescopio Nazionale (TNG), the Calar Alto 3.5m (CA 3.5m) and 2.2m (CA 2.2m) telescopes, the Asiago 67/92cm Schmidt (AS Schmidt) and 1.82m Copernico (AS 1.82m) telescopes, the William Herschel Telescope (WHT), the Albanova Telescope[1] (AT) and the United Kingdom Infrared Telescope (UKIRT). The late time dataset includes 61 epochs of optical imaging and 9 epochs of NIR imaging which, together with the early time observations, gives a total of 146 epochs of optical imaging and 32 epochs of NIR imaging. Spitzer has systematically been observing SN 2011dh under program ID 70207 (PI Helou), 90240 (PI Kasliwal) and 10136 (PI Kasliwal) and Helou et al. (2013) presented Spitzer photometry between 18 days to 625 days. E14a presented Spitzer photometry between 18 and 85 days (using an independent procedure) and in this paper we present observations up to 1061 days. Here and throughout the paper, we label the Spitzer 3.6 μm and 4.5 μm bands S_1 and S_2, respectively. The reduction and calibration procedures used for the late time data are the same as in E14a, and are described in detail therein, where we also provide a thorough discussion on the accuracy of the photometry. In Appendix A we discuss data reduction and calibration issues specifically related to the >100 days data.

The S-corrected optical and NIR magnitudes and their corresponding errors are listed in Tables 4, 5, and 6 and the Spitzer S_1 and S_2 magnitudes and their corresponding errors in Table 7. For completeness we also include the magnitudes for the first 100 days already published in E14a. The magnitudes for the <800 days period, including the SWIFT magnitudes published in E14a and S-corrected magnitudes for the HST observations published in Van Dyk et al. (2013), are shown in Fig. 1. We also show cubic spline fits using 3-5 point knot separation, error weighting and a 5 percent error floor or, when the sampling is sparse, linear interpolations, as well as extrapolations assuming a constant colour to adjacent bands. The extrapolation method used makes some sense in the early phase when the spectral energy distribution (SED) is dominated by the continuum, but less so in the late phase when it is dominated by lines, which should be kept in mind. In particular, the NIR magnitudes are extrapolated between ~400 and ~750 days, which introduce a large uncertainty in these magnitudes. Many calculations, throughout the paper, are based on these spline fits, interpolations and extrapolations. In these calculations the errors in the fitted splines have been estimated as the standard deviation and then propagated.

2.2. Photometric evolution

In Fig. 2 we show absolute optical and NIR magnitudes for SNe 2011dh, 1993J and 2008ax, and in Table 1 we tabulate the tail decline rates at 100, 200 and 300 days. Most striking is the sim-

[1] 1.0 m Nasmyth-Cassegrain telescope at Albanova, Stockholm University. Equipped with an Andor DV438 CCD camera with an E2V 20C CCD chip and Bessel-like *UBVRI* filters.

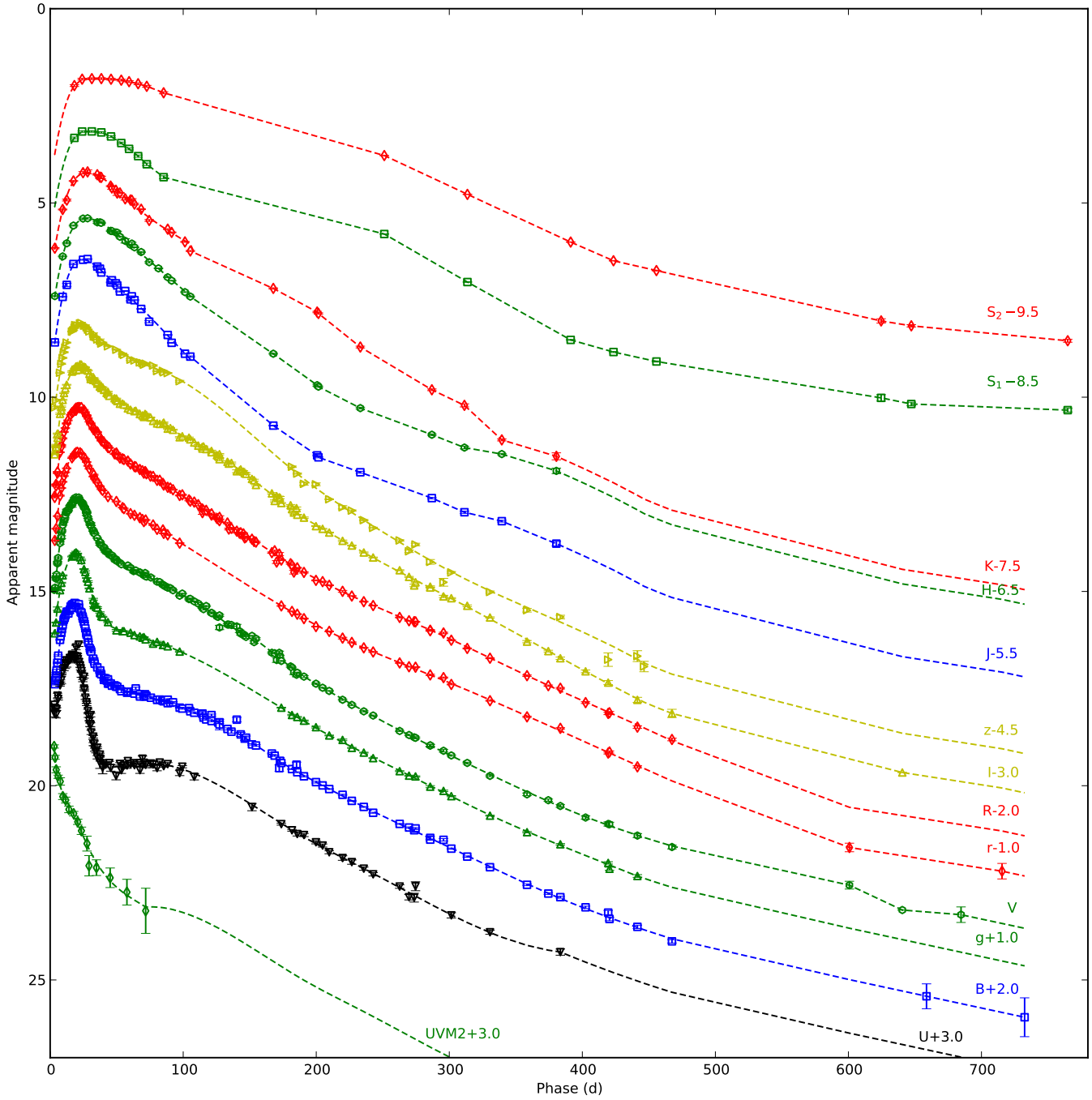

Fig. 1. Photometric evolution of SN 2011dh in the UV, optical, NIR and MIR. For clarity each band has been shifted in magnitude. Each lightcurve has been annotated with the name of the band and the shift applied. We also show combinations of spline fits, interpolations and extrapolations described in Sect 2.1 (dashed lines).

ilarity between the lightcurves, except for a shift towards higher luminosities for SNe 1993J and 2008ax, the shift being larger in bluer bands and negligible in the NIR, and most pronounced for SN 2008ax. As discussed in E14a, this difference could be explained by errors in the adopted extinctions.

Given the caveat that SNe 1993J and 2008ax are only partly covered in U and NIR, we find the following general trends. At 100 days the V, R and I-band decline rates are roughly twice the decay rate of ^{56}Co, and subsequently decrease towards 300 days. The U and B-band decline rates are significantly lower at 100 days, subsequently approach the other optical decline rates and then evolve similarly. The J and H-band decline rates are considerably higher than the optical at 100 days, subsequently approaches those and eventually become considerably lower. For SNe 2011dh and 1993J, the K band behaves quite differently than the other NIR bands. At 100 days the decline rate is significantly lower, but as it remains roughly constant, it subsequently approaches the other NIR decline rates and eventually becomes considerably higher. As seen in Fig. 1, the optical lightcurves of SN 2011dh flatten considerably after ~450 days, approaching a decline rate similar to, or lower than, the decay rate of ^{56}Co.

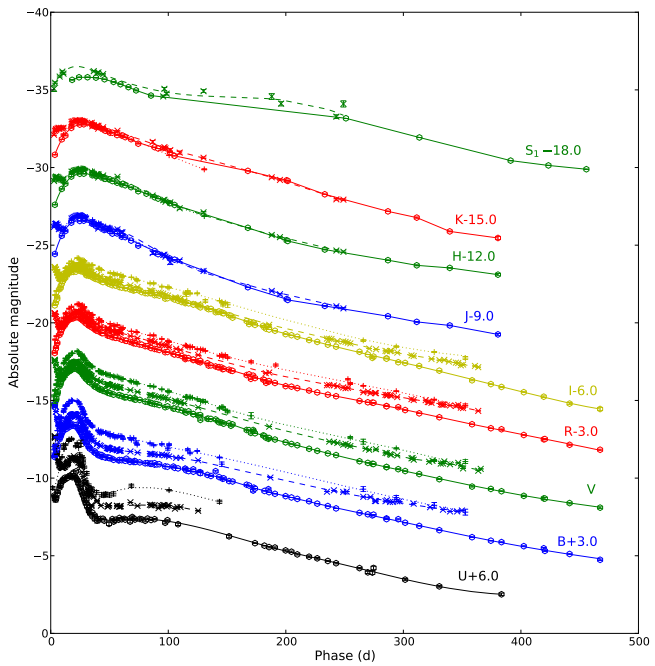

Fig. 2. Photometric evolution of SNe 2011dh (dots), 1993J (crosses) and 2008ax (pluses) in the optical and NIR. For clarity each band has been shifted in magnitude. Each lightcurve has been annotated with the name of the band and the shift applied. We also show combinations of spline fits, interpolations and extrapolations described in Sect. 2.1 (dashed lines).

Both SNe 2011dh and 1993J were also monitored in the MIR, SN 2011dh in the S_1 and S_2 bands and SN 1993J in the L band, which is similar to the S_1 band. For both SNe, a strong excess in the MIR develops between ~100 and ~250 days. For SN 1993J the MIR coverage ends at ~250 days, and for SN 2011dh the subsequent evolution is fairly similar to the evolution in the optical. After ~400 days, a considerable flattening of the MIR lightcurves is seen, similar to, but more pronounced than the flattening of the optical lightcurves. After ~750 days (not shown in Fig. 1) this trend continues and the MIR lighcurves become almost flat.

2.3. Bolometric evolution

As in E14a we use a combination of the spectroscopic and photometric methods, applied to wavelength regions with and without spectral information, respectively, when calculating the pseudo-bolometric lightcurves. The details of these methods have been described in E14a. Combinations of spline fits, interpolations and extrapolations (Sect. 2.1; Figs. 1 and 2) have been used to calculate the magnitudes. Here and throughout the paper, the wavelength regions over which the luminosity is integrated are specified as follows; UV (1900-3300 Å), optical (3300-10000 Å), NIR (10000-24000 Å) and MIR (24000-50000 Å).

Figure 3 shows the <500 days optical to NIR pseudo-bolometric lightcurves for SNe 2011dh, 1993J and 2008ax, as calculated with the photometric method, and in Table 2 we tabulate the decline rates at 100, 200 and 300 days. Given the caveat that SNe 1993J and 2008ax are not covered in NIR after ~250 and ~150 days, respectively, their optical to NIR pseudo-bolometric lightcurves are remarkably similar to the one of SN 2011dh, except for the shift towards higher luminosities discussed previously in Sect. 2.2. The decline rates decrease from ~0.020 mag day^{-1}, roughly twice the decay rate of ^{56}Co, at 100 days to ~0.015 mag day^{-1} at 300 days. There is however a significant increase in the decline rate between 150 and 200 days for SN 2011dh, even more pronounced in the optical pseudo-bolometric lightcurve, not seen for SNe 1993J and 2008ax. For SN 1993J the decline rate becomes increasingly lower towards 300 days as compared to SNe 2011dh and 2008ax, which is consistent with an increasing contribution from circum-stellar medium (CSM) interaction in this phase.

Figure 4 shows the <750 days UV to MIR pseudo-bolometric lightcurve for SN 2011dh, as calculated with the combined spectroscopic and photometric methods, and in Table 9 we tabulate the 3-400 days period (for which we have full optical to MIR

Table 1. Tail decline rates at 100, 200 and 300 days for SN 2011dh, compared to SNe 1993J and 2008ax, as measured from cubic spline fits.

SN	Band	Rate (100 d) (mag day^{-1})	Rate (200 d) (mag day^{-1})	Rate (300 d) (mag day^{-1})
2011dh	U	0.011	0.019	0.017
2011dh	B	0.014	0.018	0.017
2011dh	V	0.018	0.020	0.016
2011dh	R	0.021	0.018	0.016
2011dh	I	0.019	0.020	0.018
2011dh	J	0.036	0.018	0.011
2011dh	H	0.029	0.019	0.011
2011dh	K	0.020	0.020	0.024
1993J	U	0.006	...	...
1993J	B	0.011	0.017	0.012
1993J	V	0.019	0.019	0.017
1993J	R	0.022	0.015	0.013
1993J	I	0.022	0.019	0.013
1993J	J	0.041	0.016	...
1993J	H	0.033	0.018	...
1993J	K	0.022	0.024	...
2008ax	U	0.013	...	...
2008ax	B	0.015	0.018	0.016
2008ax	V	0.022	0.018	0.017
2008ax	R	0.023	0.016	0.015
2008ax	I	0.018	0.021	0.013
2008ax	J	0.035	...	...
2008ax	H	0.032	...	...
2008ax	K	0.033	...	...

Table 2. Tail decline rates at 100, 200, and 300 days for the optical to NIR pseudo-bolometric lightcurve of SN 2011dh, compared to SNe 1993J and 2008ax.

SN	Rate (100 d) (mag day^{-1})	Rate (200 d) (mag day^{-1})	Rate (300 d) (mag day^{-1})
2011dh	0.021	0.020	0.016
2008ax	0.020	0.017	0.015
1993J	0.021	0.017	0.013

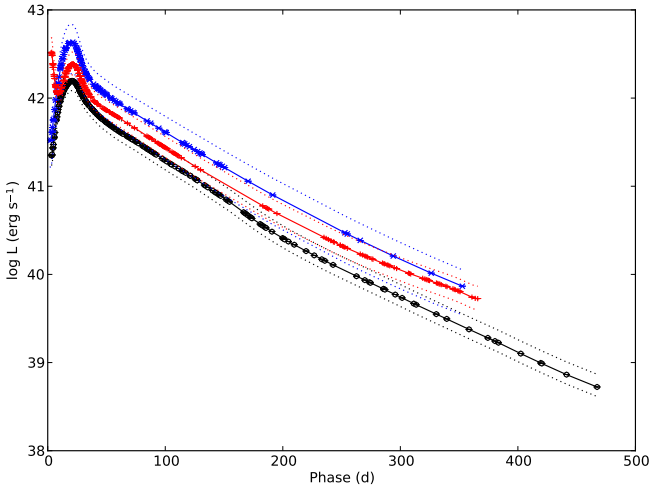

Fig. 3. Optical to NIR pseudo-bolometric lightcurve for SNe 2011dh (black circles and solid line), 1993J (red crosses and solid line) and 2008ax (blue pluses and solid line). The upper and lower error bars for the systematic error arising from extinction and distance (dotted lines) are also shown.

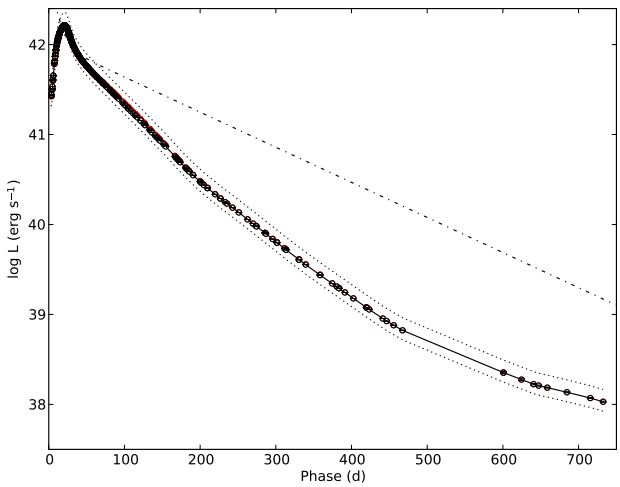

Fig. 4. UV to MIR pseudo-bolometric lightcurve for SN 2011dh (black circles and solid line). The upper and lower error bars for the systematic error arising from extinction and distance (black dotted lines) and the radioactive decay chain luminosity of 0.075 $M_\odot$ of ^{56}Ni (black dash-dotted line) are also shown.

coverage) for reference. The decline rates at 100, 200, 300 and 400 days are 0.021, 0.022, 0.015 and 0.016 mag day^{-1}, respectively, but the increase in decline rate between 150 and 200 days is not as pronounced as in the optical to NIR pseudo-bolometric lightcurve. Given the caveats that the NIR coverage ends at ~400 days, and the sampling and the measurement errors become worse after ~500 days, the UV to MIR pseudo-bolometric lightcurve shows a significant flattening after ~400 days, when the decline rate decreases to a value similar to, but lower than, the decay rate of ^{56}Co. This flattening is also observed in the optical and MIR pseudo-bolometric lightcurves, for which we have full coverage, and is discussed in more detail in Sect. 5.1.

Figure 5 shows the fractional UV, optical, NIR and MIR luminosities for SN 2011dh. We assume the late-time extrapolated fractions to stay constant and do not use the adjacent colour based extrapolations applied elsewhere. The early evolution was discussed in E14a, and after 100 days the most notable is the

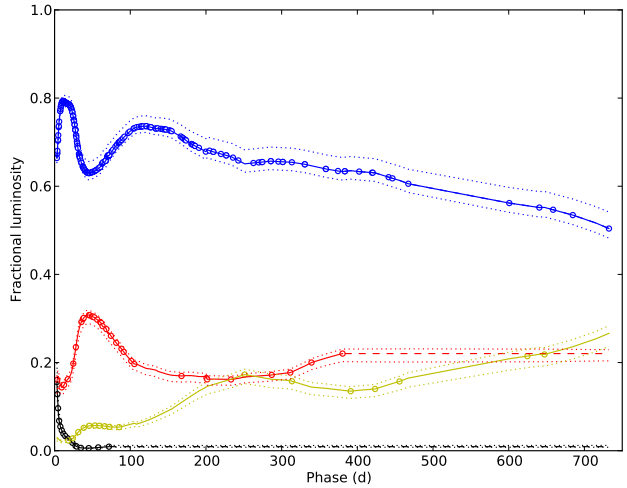

Fig. 5. Fractional UV (black dots), optical (blue dots), NIR (red dots) and MIR (yellow dots) luminosity for SN 2011dh. Interpolations and extrapolations are displayed as solid and dashed lines, respectively. The upper and lower error bars for the systematic error arising from extinction (dotted lines) are also shown.

strong increase in the MIR fraction between 100 and 250 days, together with a simultaneous decrease in the optical fraction. Also notable is the increase in the NIR fraction between 200 and 400 days caused by the evolution in the J and H bands. The evolution becomes quite uncertain after ~400 days when the NIR coverage ends, and ~500 days when the sampling and the measurement errors become worse, but there seems to be a continuous increase in the MIR fraction, at the expense of the optical fraction. Keeping the uncertainties in mind, it is worth noting the dominance of the optical luminosity even at ~750 days.

Figure 6 shows the evolution of the SED as calculated with the photometric method, overplotted with blackbody fits to the V, I, J, H and K photometry as well as the observed (interpolated) spectra. The early evolution was discussed in E14a, and after 100 days the most notable is again the strong excess developing in the MIR between 100 and 250 days. There is also a similar excess developing in the K band between 100 and 200 days, gradually fading away towards 300 days. The evolution in the K and MIR bands, as well as the behaviour of the pseudo-bolometric lightcurves between 150 and 200 days, are discussed in more detail in Sects. 4.2 and 5.2, where we compare the observed lightcurves to results from modelling.

3. Spectroscopy

In E14a we presented our <100 days observations, and analysis and comparison to SNe 1993J and 2008ax. Here we present observations spanning 100-415 days in the optical and 100-206 days in the NIR, and a continuation of the analysis and the comparison, focusing on the >100 days data. Steady-state NLTE modelling of these data, as well as a detailed analysis of the formation of the identified lines and the evolution of their fluxes, are presented in J14. Our analysis is complementary and focus mainly on the line profiles, and what can be learned about the distribution of the material from the different nuclear burning zones. Following J14 we subdivide the ejecta into a Fe/Co/He core surrounded by the Si/S zone, the oxygen-rich O/Si/S, O/Ne/Mg and O/C zones, and the helium and hydrogen envelopes. This onion-line structure corresponds to what is obtained in 1-D modelling (e.g. Woosley & Heger 2007),

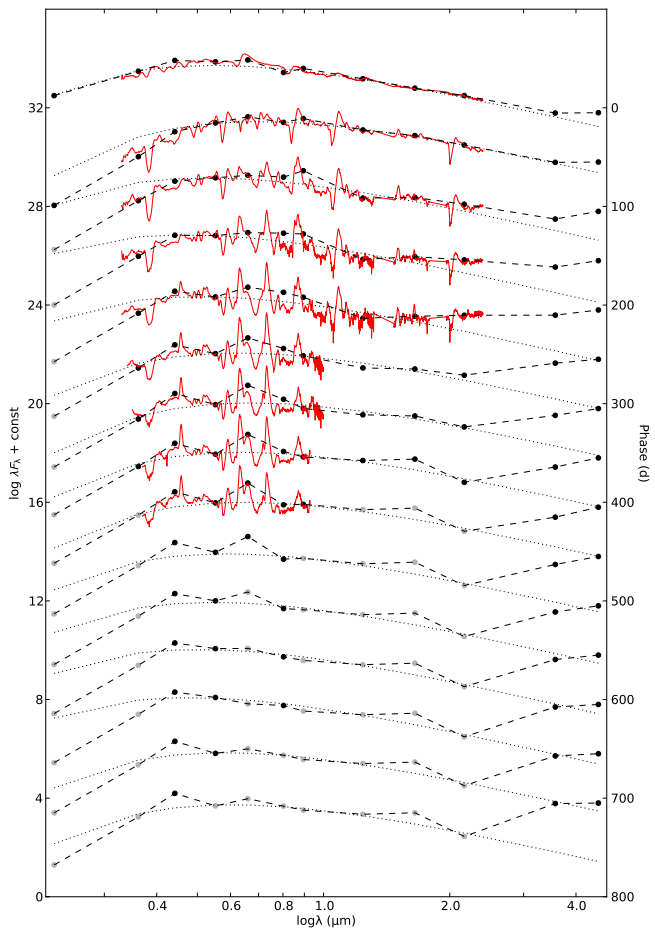

Fig. 6. The evolution of the SED as calculated with the photometric method (black dots and dashed lines) overplotted with blackbody fits to the V, I, J, H and K photometry (black dotted lines) as well as the observed spectra interpolated as described in Sect. 3.1 (red solid lines). Fluxes based on extrapolated magnitudes are displayed in shaded colour.

whereas in multi-D modelling hydrodynamical instabilities results in macroscopic mixing of these zones (e.g. Iwamoto et al. 1997). We adopt a recession velocity of 515 km s^{-1} for SN 2011dh, as estimated from the Hα velocity map in Shetty et al. (2007), which is slightly higher than the systematic recession velocity of M51 (472 km s^{-1}; Tully 1974). For SN 1993J and 2008ax we adopt the systematic recession velocities for M81 (−34 km s^{-1}; Tully et al. 2008) and NGC 4490 (565 km s^{-1}; Lavaux & Hudson 2011), respectively. The references for the spectroscopic data of SNe 1993J and 2008ax used in the comparison are the same as specified in E14a, but in addition we also include spectra for SN 2008ax from Milisavljevic et al. (2010), and unpublished spectra for SN 1993J obtained with the WHT and the Isaac Newton Telescope (INT) (P. Meikle et al.; private communication), described in J14.

3.1. Observations

The <100 days data were obtained with the NOT, the TNG, the WHT, the INT, the CA 2.2m, the AS 1.82m and the Gran Telescopio Canarias (GTC). Details of the late time spectroscopic observations, the telescope and instrument used, epoch and instrument characteristics are given in Table 8. The late time dataset includes 26 optical spectra obtained at 21 epochs and 2 NIR spectra obtained at 2 epochs which, together with the early time observations, gives a total of 81 optical spectra obtained at 47 epochs and 20 NIR spectra obtained at 12 epochs. The reductions and calibration procedures used for the late time data are the same as in E14a, and are described in detail therein.

All reduced, extracted and calibrated spectra will be made available for download from the Weizmann Interactive Supernova data REPository[2] (WISeREP) (Yaron & Gal-Yam 2012). Figure 7 shows the sequence of observed spectra, where those obtained on the same night using the same telescope and instrument have been combined. In addition to this, the 289, 292 and 293 days NOT spectra and the 228, 229, and 231 days INT spectra have been combined to increase the signal to noise ratio (SNR). For clarity some figures in this and the following sections are based on time-interpolations of the spectral sequence, as described in E14a. Interpolated spectra separated by more than half the sampling time from observed spectra are displayed in shaded colour, whereas interpolated spectra displayed in full colour are usually more or less indistinguishable from observed spectra. To further visualize the evolution, the spectra have been aligned to a time axis at the right border of the panels. Interpolated spectra were used in the calculations of the bolometric lightcurve (Sect. 2.3) and S-corrections. Figure 8 shows the interpolated optical and NIR spectral evolution of SN 2011dh for 5−425 days with a 20-day sampling. All spectra in this and subsequent figures have been corrected for redshift and interstellar extinction.

3.2. Line evolution

Figure 9 shows the (interpolated) evolution for all the lines identified in J14, and below we discuss selected lines element by element. Most of the identified lines are also marked Fig. 8. The evolution of the line fluxes were discussed in J14 and here we focus mainly on the line profiles, in particular the sizes of the line emitting regions and asymmetries, which we will return to in Sects. 3.4 and 3.5. To measure the sizes of the line emitting regions, we fit a simple model for optically thin line emission to the observed line profiles. The model includes an absorptive continuum opacity to mimic blue shifts caused by obscuration of receding side emission, and is only applied if the scattering contribution appears to be small. To measure asymmetries in the lines profiles, we calculate the first wavelength moment of the flux (center of flux). The details of the methods are given in Appendix B, where we also describe how the [O I] 6300,6364 Å line is decomposed and the treatment of other blended lines.

Hydrogen Some Hα emission arising from the hydrogen envelope is present in the preferred J14 steady-state NLTE model (12C; see Sect 4.2.2), but is increasingly dominated by [N II] 6548,6583 Å emission arising from the helium envelope after ∼150 days (J14). In the spectra of SN 2011dh, there is an emerging emission feature near the rest wavelength of Hα, increasing in strength towards 450 days (Fig. 9). Assuming this feature to originate from the [N II] 6548,6583 Å line, we find it to be well fitted by emission from a region with a radius of 5500 km s^{-1}, emitting mainly in the [N II] 6583 Å line, although the wings of the observed line profile may extend to ∼12000 km s^{-1} on the red side. Hα emission from the hydrogen-rich envelope is expected to result in a flat-topped line profile, at least 11000 km s^{-1} wide

[2] http://www.weizmann.ac.il/astrophysics/wiserep/

(E14a). The size of the line emitting region, as well as the extent of the wings, is instead consistent with emission from the helium envelope, in agreement with the results in J14. Similar features exists in the spectra of SNe 1993J and 2008ax, and for the latter Taubenberger et al. (2011) argued against a hydrogen envelope origin along similar lines. No detectable absorption is found in any of the hydrogen lines after ~150 days in the preferred J14 steady-state NLTE model. In the spectra of SN 2011dh, there is a dip in the [O I] 6300,6364 Å line profile after ~150 days (Figs. 9 and 10), that corresponds well to the early time Hα absorption minimum at ~11000 km s^{-1} (E14a). However, as discussed in Sect. 3.6, this feature repeats in a number of other lines, and is rather due to clumping/asymmetries in the ejecta.

Helium The identified lines are the He I 5016 Å, He I 6678 Å, He I 7065 Å, He I 10830 Å and He I 20581 Å lines, although the He I 10830 Å line is blended with the [S I] 10820 Å line (J14). The He I 6678 Å and He I 7065 Å lines are distinguishable at ~100 days, but then quickly disappear, possibly due to blends with other lines. The He I 5016 Å line shows a P-Cygni like profile and is present, at least, until ~300 days. The He I 10830 Å and He I 20581 Å lines show P-Cygni like profiles and are present, at least, until ~200 days (when our NIR coverage ends). In J14 we find the He I 10830 Å line to be optically thick at all times, the He I 20581 Å line at $\lesssim$300 days, and the He I 5016 Å line at $\lesssim$200 days, which is consistent with the observed P-Cygni like profiles, suggesting a significant contribution from scattering. The absorption extends to ~10000 km s^{-1} for the He I 20581 Å line and a bit further for the He I 10830 Å line. This is consistent with the ~11000 km s^{-1} estimated for size of the helium core in E14a.

Oxygen The identified lines are the [O I] 5577 Å, [O I] 6300,6364 Å, O I 7774 Å, O I 9263 Å, O I 11290,11300 Å and O I 13164 Å lines, although the O I 9263 Å line is blended with the [Co II] 9338,9344 Å line on the red side, the O I 11290,11300 Å line with the [S I] 11310 Å line, and the O I 13164 Å line with the [Fe II] 13210,13280 Å line on the red side (J14). The O I 7774 Å line shows a P-Cygni like profile at $\lesssim$300 days, suggesting a significant contribution from scattering, whereas none of the other oxygen lines show any sign of absorption. In J14 we find the O I 7774 Å line to be optically thick at $\lesssim$400 days, which is consistent with the observed P-Cygni like profile. The left panel of Fig. 10 shows line profile fits for the decomposed [O I] 6300 Å line for SN 2011dh. We measure the radius of the [O I] 6300,6364 Å line emitting region to 3400, 3100 and 2900 km s^{-1} at 202, 300 and 415 days, respectively. The line profile fits are quite good, but the observed emission is underestimated at low velocities and extends to at least ~5000 km s^{-1}, suggesting radially decreasing emissivity. The other oxygen lines are either too weak for a reliable measurement, optically thick or blended with other lines. The center of flux of the [O I] 6300,6364 Å line shows a blue-shift of ~800 km s^{-1} at 100 days, decreasing towards zero at 400 days, whereas the center of flux of the [O I] 5577 Å line shows a blue-shift of ~1300 km s^{-1} at 100 days, decreasing towards ~900 km s^{-1} at 200 days, when the line begins to fade away. We do not find any significant blue-shifts of the O I 11290,11300 Å or O I 13164 Å lines.

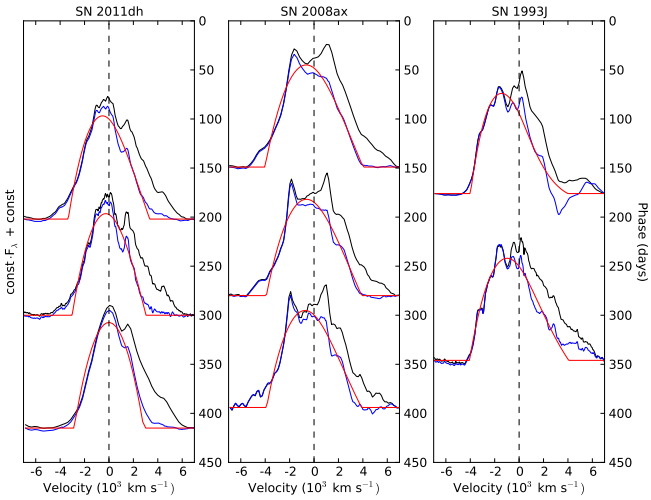

Fig. 10. [O I] 6300,6364 Å (black) and decomposed [O I] 6300 Å (blue) line profiles at selected epochs as compared to line profile fits (red) for SNe 2011dh (left panel), 2008ax (middle panel) and 1993J (right panel).

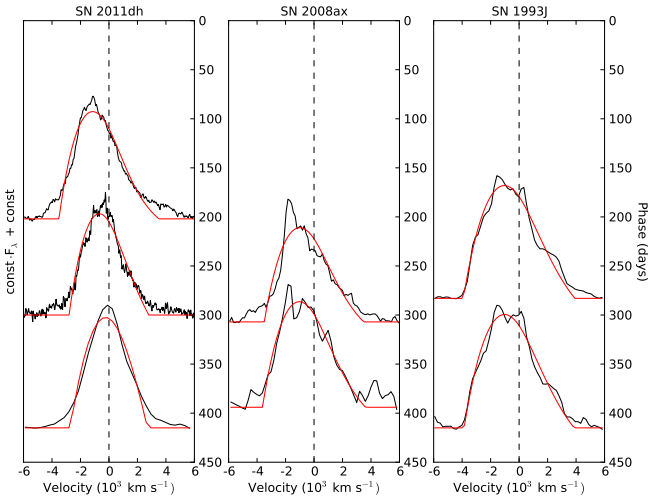

Fig. 11. Mg I] 4571 Å line profiles (black) at selected epochs as compared to line profile fits (red) for SNe 2011dh (left panel), 2008ax (middle panel) and 1993J (right panel).

Magnesium The identified lines are the Mg I] 4571 Å and Mg I 15040 Å lines, although the Mg I 15040 Å line is (weakly) blended with the Mg I 14800 Å line on the blue side (J14). None of these lines show any sign of absorption. The left panel of Fig. 11 shows line profile fits for the Mg I] 4571 Å line for SN 2011dh. We measure the radius of the Mg I] 4571 Å line emitting region to 3600, 2800 and 2700 km s^{-1} at 202, 300 and 415 days, respectively, and the radius of the Mg I 15040 Å line emitting region to 3500 and 3200 km s^{-1} at 89 and 206 days, respectively. The line profile fits of the Mg I] 4571 Å line are quite good, but the observed emission is underestimated at low velocities and extends to at least ~5000 km s^{-1}, suggesting radially decreasing emissivity. The center of flux of the Mg I] 4571 Å line shows a blue-shift of ~800 km s^{-1} at 200 days, decreasing towards ~100 km s^{-1} at 400 days. We do not find any significant blue-shift of the Mg I 15040 Å line.

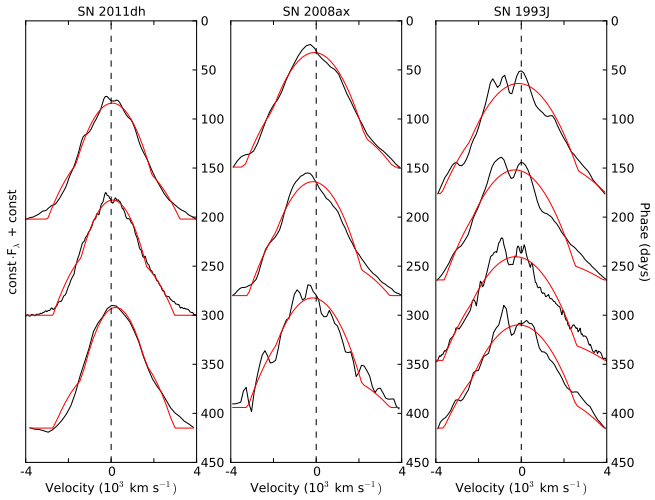

Fig. 12. [Ca II] 7291,7323 Å line profiles (black) at selected epochs as compared to line profile fits (red) for SNe 2011dh (left panel), 2008ax (middle panel) and 1993J (right panel).

Calcium The identified lines are the Ca II 3934,3968 Å, [Ca II] 7291,7323 Å and Ca II 8498,8542,8662 Å lines, although the [Ca II] 7291,7323 Å line is blended with the [Fe II] 7155 Å and [Ni II] 7377,7411 Å lines on the blue and red side, respectively, and the Ca II 8498,8542,8662 Å line with the [C I] 8727 Å line (J14). The Ca II 3934,3968 Å line is present in strong absorption, extending to ∼15000 km s^{-1}, throughout the evolution. The Ca II 8498,8542,8662 Å line shows an absorption component at ∼100 days, which quickly disappears, whereas the [Ca II] 7291,7323 Å line shows no sign of absorption. The left panel of Fig. 12 shows line profile fits for the [Ca II] 7291,7323 Å line for SN 2011dh. As the line appears to have extended wings we use a two-component region in the fit. We measure the radii of the [Ca II] 7291,7323 Å line emitting regions to 2400/9200, 2100/8700 and 2500/8700 km s^{-1} at 202, 300 and 415 days, respectively. The fitted 7291 to 7323 Å line ratio is 1.09, 1.05 and 0.39 at 202, 300 and 415 days, respectively. This is lower than the value of 1.5 expected for optically thin emission and local thermal equilibrium (LTE) populations, in particular at 415 days. The line profile fits are good in the inner region but worse in the wings, which are quite asymmetric, and the strong red-side wing might explain the low line ratios obtained. Fitting only the central part gives line ratios in better agreement with the expected value, and similar sizes of the line emitting regions. In J14 we find no substantial [Ca II] 7291,7323 Å emission from the helium envelope, which suggests that the wings could be explained by emission from other lines. Except for the [Fe II] 7155 Å line, which clearly contributes to the blue wing, the [Ni II] 7377,7411 Å line could contribute substantially to the red wing. A further contribution from the He I 7065 Å line to the blue wing is also possible. The center of flux for the Ca II 8498,8542,8662 Å line shows a red-shift increasing towards ∼1100 km s^{-1} at 400 days. As the center of flux is calculated with respect to the rest wavelength of the Ca II 8662 Å line (Appendix B), this suggests a significant contribution from the [C I] 8727 Å line to the flux.

Iron group The identified lines are the [Fe II] 7155 Å, [Fe II] 12567 Å and [Fe II] 16440 Å lines, although the [Fe II] 7155 Å line is blended with the [Ca II] 7291,7323 Å line on the red side, and the [Fe II] 16440 Å line is blended with the [Si I] 16450 Å line (J14). The identified cobalt lines are the [Co II] 9338,9344 Å, [Co II] 10190,10248,10283 Å and [Co II] 15475 Å lines, although the [Co II] 9338,9344 Å line is blended with the O I 9263 Å line on the blue side, the [Co II] 10190,10248,10283 Å line with the [S II] 10340,10370 Å line on the red side, and the [Co II] 15475 Å line with the Fe II 15340 Å line on the blue side (J14). None of the identified iron and cobalt lines shows any sign of absorption. We measure the radius of the [Fe II] 7155 Å line emitting region to 1600 and 1700 km s^{-1} at 300 and 415 days, respectively, and the radius of the [Fe II] 16440 Å line emitting region to 2300 and 2400 km s^{-1} at 89 and 206 days, respectively. As mentioned, the latter is likely to be blended with the [Si I] 16450 Å line, and it is unclear which line is dominating. The detection of the [Fe II] 12567 Å line is marginal and the line is too weak for a reliable measurement. We measure the radius of the [Co II] 10190,10248,10283 Å line emitting region to 1800 km s^{-1} at 89 and 206 days. The fitted 10190 to 10248 Å and 10190 to 10283 Å line ratios are 0.44/0.02, and 0.56/0.39, at 89 and 206 days, respectively. In the preferred J14 steady-state NLTE model, these ratios are 0.28/0.30 at 200 days, in reasonable agreement with the fitted values. The blending adds uncertainty to the measurement though, and the line is also blended with the [S II] 10340,10370 Å line on the red side. The other cobalt lines are either too weak for a reliable measurement or blended with other lines.

3.3. CO emission

The upper left panel of Fig. 13 shows the observed K-band spectrum at 206 days compared with the preferred steady-state NLTE model spectrum at 200 days, flux calibrated with the observed K-band flux at 206 days. The model (12F; see Sect. 4.2.2 and Appendix C) includes dust but not CO emission. The CO first overtone (Δv=2) emits between 2.25 and 2.45 μm and we have marked the location of the band heads, which are not sharp due to the Doppler broadening of the individual transitions contributing. There is a strong excess in this region as compared to the model spectrum, the integrated flux being 1.0×10^{-14} erg s^{-1} cm^{-2}. The contribution from this flux to the K-band flux is negligible though, due to the weak overlap with this band. We have used a simple LTE CO model described in Spyromilio et al. (1988) to provide a fit to the emission. The ratio of the band head emission is a diagnostic of the temperature of the CO, and the shape of the band heads a diagnostic of the expansion velocity of the CO gas. In the upper right panel of Fig. 13 we show the combined CO model and preferred steady-state NLTE model spectrum. The shape of the observed emission and the agreement with the simple CO model provides strong support for the identification of this feature with emission from the first overtone of CO. The temperature in the CO model is 2300 K and the emission region extends to 1500 km s^{-1}. The lower panel of Fig. 13 shows the observed H and K-band spectrum at 89 days. As this spectrum was obtained before 100 days, where the steady-state condition needed for the NLTE modelling is not satisfied, we instead use a blackbody fit to estimate the continuum. Although not as convincing as at 206 days, there is a clear excess in the region where we expect CO first overtone emission, the integrated flux being 7.2×10^{-14} erg s^{-1} cm^{-2}. The contribution from this flux to the K-band flux is again negligible. In the absence of a model for the underlying emission we have not tried to fit the excess emission with the LTE CO model, but the

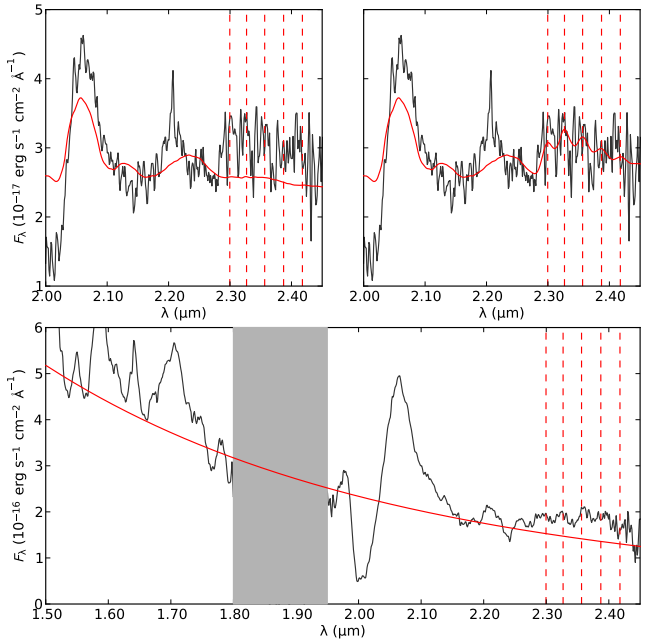

Fig. 13. Upper left panel: Observed (black solid line) and preferred steady-state NLTE model (red solid line) *K*-band spectra at 206 and 200 days, respectively. Upper right panel: The same, but with CO LTE model emission added to the steady-state NLTE model spectra. The CO overtone band heads have been marked by red dashed lines and the steady-state NLTE model spectra flux calibrated with the observed *K*-band flux at 206 days. Lower panel: Observed (black solid line) *H* and *K*-band spectrum at 89 days as compared to a blackbody fit to the continuum (red solid line).

structure of the feature shows a reasonable agreement with the expected positions of the band heads.

3.4. Line emitting regions

The sizes of the line emitting regions are related to the distribution of the material from the different nuclear burning zones, determined by hydrodynamical instabilities in the explosion. In J14 we found the Mg I lines to arise from the O/Ne/Mg zone, the O I lines to arise from the O/Ne/Mg zone and, depending on the amount of molecule (CO and SiO) cooling, the O/C and O/Si/S zones. We also found the [Ca II] 7291,7323 Å line to arise mainly from the Si/S zone and the Fe II and Co II lines to arise from the Fe/Co/He zone. The estimated radii of the Mg I and O I line emitting regions of 2900-3400 and 2700-3600 km s^{-1}, respectively, are similar, whereas the estimated radii of the [Ca II] 7291,7323 Å and the Fe II and Co II line emitting regions of 2100-2500 and 1600-2400 km s^{-1}, respectively, are progressively smaller (Sect. 3.2). This progression is consistent with the (unmixed) onion-like structure of the nuclear burning zones, and suggests incomplete mixing of the oxygen, Si/S and Fe/Co/He material. This is in agreement with results from multi-D hydrodynamical modelling, e.g. the 2-D hydrodynamical modelling of SN 1993J by Iwamoto et al. (1997), which shows significant differences in the distribution of the oxygen and Fe/Co/He material.

The left panel of Fig. 14 shows mirrored blue-side line profiles for the [O I] 6300 Å, Mg I] 4571 Å, [Ca II] 7291 Å and [Fe I] 7155 Å lines for SN 2011dh at 300 days. The blue side is less affected by obscuration as compared to the red side and contamination from the [O I] 6364 Å and [Ca II] 7323 Å lines to the [O I] 6300 Å and [Ca II] 7291 Å lines is probably modest. This figure nicely illustrates the different sizes of the line emitting regions discussed above, and also shows a remarkable similarity of the blue-side [O I] 6300 Å and Mg I] 4571 Å line profiles. This similarity persists also in small scale fluctuations (Sect. 3.6), and suggests these lines to arise mainly from the O/Ne/Mg zone, and the contributions from the O/C and O/Si/S zones to the [O I] 6300 Å flux to be modest.

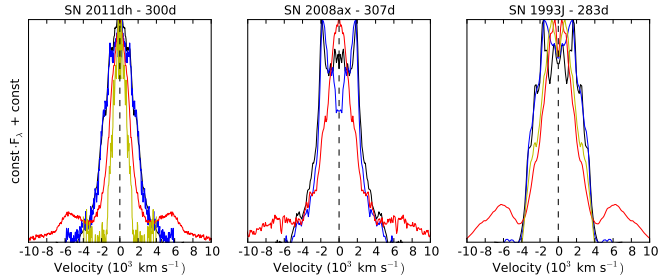

Fig. 14. Continuum subtracted mirrored blue-side profiles for the [O I] 6300,6364 Å (black), Mg I] 4571 Å (blue), [Ca II] 7291,7323 Å (red) and [Fe I] 7155 Å (yellow) lines for SNe 2011dh, 2008ax and 1993J at 300, 307 and 283 days respectively.

The middle and right panels of Figs. 10, 11, 12 and 14 show line profile fits and mirrored blue-side line profiles for SNe 2008ax and 1993J, respectively. For SN 1993J the estimated radii of the line emitting regions are 4000-4100 km s^{-1} for the [O I] 6300 Å line, 3700-3900 km s^{-1} for the Mg I] 4571 Å line and 3000-3400 km s^{-1} for the [Ca II] 7291,7323 Å line. For SN 2008ax the estimated radii of the line emitting regions are 3900-4000 km s^{-1} for the [O I] 6300 Å line, 3400-3600 km s^{-1} for the Mg I] 4571 Å line and 2600-3000 km s^{-1} for the [Ca II] 7291,7323 Å line. These radii are larger than those estimated for SN 2011dh, and larger for SN 1993J than for SN 2008ax. The radii of the Mg I] 4571 Å and the [O I] 6300 Å line emitting regions are similar, and the radius of the [Ca II] 7291,7323 Å line emitting region is smaller, suggesting incomplete mixing of the oxygen and Si/S material. This is supported by Fig. 14, and the similarity of the blue-side Mg I] 4571 Å and the [O I] 6300 Å line profiles is striking, suggesting these to arise mainly from the O/Ne/Mg zone.

As is also evident from Fig. 14, there are considerable differences in the shapes of line profiles between SNe 2011dh, 2008ax and 1993J. The profile of the [Ca II] 7291,7323 Å line is centrally peaked for all three SNe, whereas the peaks of the [O I] 6300 Å and Mg I] 4571 Å lines are considerably flatter for SNe 1993J and 2008ax. A thorough discussion of this interesting topic is, however, outside the scope of the paper. Finally, it is worth noting, that the double peaks of the [O I] 6300,6364 Å line profile for SN 2008ax (Fig. 10), seem to be well explained by a repetition of the blue peak, as suggested by Milisavljevic et al. (2010) and Taubenberger et al. (2011). As pointed out by Milisavljevic et al. (2010), the blue peak also seems to repeat in the Mg I] 4571 Å line (Fig. 11). Maurer et al. (2010) suggested absorption by high-velocity Hα to explain the double peaks which, given the negligible Hα absorption found at late times in J14, seems less likely. Our decomposition method assumes a [O I] 6300,6364 Å line ratio of 3 and is described in Appendix B.

3.5. Line asymmetries

Asymmetries in the line profiles may be caused by intrinsic asymmetries in the ejecta or radiative transfer effects. Both scattering and absorption may skew an initially symmetric line profile. Figure 15 shows the center of flux velocities for the [O I] 6300,6364 Å, [O I] 5577 Å, Mg I] 4571 Å and [Ca II] 7291,7323 Å lines for SNe 2011dh, 2008ax and 1993J. As discussed in Sect. 3.2 there is a blue-shift of the [O I] 6300,6364 Å, [O I] 5577 Å and Mg I] 4571 Å lines for SN 2011dh, which is also present, and even more pronounced, for SNe 2008ax and 1993J. For SN 2011dh this blue-shift disappears towards 400 days, but for SNe 2008ax and 1993J the blue-shift saturates at ~500 km s^{-1} after 200 days. In J14 we provide a thorough discussion of these blue-shifts, and suggest the cause to be line-blocking in the core. There is no significant blue shift in the O I 11300 Å, O I 13164 Å and [Mg I] 15040 Å lines for SNe 2011dh (Sect. 3.2) and 2008ax, in support of this hypothesis, as line-blocking is less effective in the NIR (J14). Milisavljevic et al. (2010) find the [O I] 6300,6364 Å, [O I] 5577 Å and Mg I] 4571 Å lines to be either symmetric or asymmetric towards the blue for a sample of 18 stripped envelope SNe, whereas Taubenberger et al. (2009) find a systematic blue-shift of the [O I] 6300,6364 Å line disappearing with time for another, partly overlapping, sample of 39 stripped envelope SNe. Both these results favours obscuration of the receding-side emission, and disfavours ejecta asymmetries as the explanation. However, to explain the saturation of the blue-shifts for SNe 2008ax and 1993J, the evolution of the core-opacity needs to be different for these SNe as compared to SN 2011dh.

Blue-shifts of the lines profiles can also be produced by dust in the ejecta. As discussed in Sect. 4.2, the preferred J14 steady-state NLTE model has a homogeneous dust opacity in the core, in order to explain the behaviour of the lightcurves for SN 2011dh between 100 and 250 days (Sect. 2.3). The version of the preferred model used in this work (12F) has an optical depth of 0.44, which is found to best reproduce the observed lightcurves, whereas the original version (12C) has an optical depth of 0.25. This lower value gives a worse reproduction of the lightcurves, but produce smaller blue-shifts, which, as discussed below, seems to be in better agreement with observations. Using our line profile model and assuming a size of the line-emitting region of 3000 km s^{-1} (Sect. 3.4), we find blue-shifts of the center of flux of 150 and 250 km s^{-1} for optical depths of 0.25 and 0.44, respectively. A comparison with observations is not straightforward, as the effects of dust and line blocking are hard to disentangle, and most lines are either blends, do not arise solely from the core, or are too weak for a reliable measurement. At 415 days, when the effect from line-blocking would be the least, the center of flux for the [O I] 6300,6364 Å and Mg I] 4571 Å lines, which arise solely from the core (J14), shows a red-shift of ~100 and a blue-shift of ~100 km s^{-1}, respectively. The absence of significant blue-shifts in these lines suggest a small optical depth and indicate that, if the optical depth is as high as 0.44, the dust can not be homogeneously distributed within the core. For SNe 1993J and 2008ax dust in the ejecta provides an alternative explanation for the saturation of the blue-shifts. Using our line profile model and assuming a size of the line-emitting region of 4000 km s^{-1} (Sect. 3.4), we find a blue shift of the center of flux of ~500 km s^{-1} to correspond to an optical depth of ~1. Neither SN 1993J nor SN 2008ax show a period with increased decline rates in the optical pseudo-bolometric lightcurve, which disfavours dust as the explanation, although SN 1993J show a MIR excess developing between 100 and 250 days, similar to that observed for SN 2011dh.

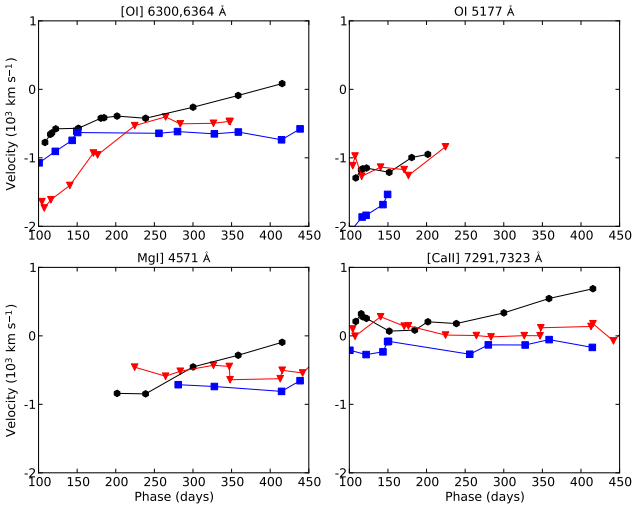

Fig. 15. Center of flux velocities for the [O I] 6300,6364 Å (upper left panel), [O I] 5577 Å (upper right panel) Mg I] 4571 Å (lower left panel), [Ca II] 7291,7323 Å (lower right panel) lines for SNe 2011dh (black dots), 2008ax (blue squares) and 1993J (red triangles).

3.6. Small scale fluctuations

Small scale fluctuations in the line profiles may provide evidence for a clumpy ejecta, as previously demonstrated for SNe 1987A (Stathakis et al. 1991; Chugai 1994) and 1993J (Spyromilio 1994; Matheson et al. 2000). In a simplified way we may represent the material of some nuclear burning zone by a number of randomly distributed clumps, having a typical size and occupying some fraction of the ejecta volume (filling factor). The small scale fluctuations in the line profiles then arise from statistical fluctuations in the distribution of the clumps, the RMS (Root Mean Square) of the fluctuations increasing with decreasing number of clumps and/or filling factor, and/or increasing size of the clumps. In the simplest case the ejecta is assumed to be a (globally) homogeneous sphere, which is in fact exactly how the core is represented in the steady-state NLTE modelling (Sect. 4.2).

Figure 16 shows small scale fluctuations in the [O I] 6300,6364 Å, [O I] 5577 Å, O I 7774 Å, Mg I] 4571 Å and Na I 5890,5896 Å lines at 202 and 300 days. The resolution is ~600 and ~250 km s^{-1} in the 202 and 300 days spectra, respectively. A 1000 km s^{-1} box average of the line profile was repeatedly (3 times) subtracted to enhance the small scale fluctuations. The method has been tested on the product of synthetic large and small scale structures, and the small scale structures are recovered with reasonable accuracy. In the upper left panel we show a comparison of the [O I] 6300 Å line profiles at 202 and 300 days. These are very similar and there is not much evolution of the small scale fluctuations in the line profile during this period. We identify 8 features marked A-H with a FWHM between 300 and 600 km s^{-1} present at both epochs. However, features G and H interpreted as belonging to the [O I] 6364 Å line, match very well with the E and F features interpreted as belonging to the [O I] 6300 Å line, so these are likely to be repetitions. Subtracting the [O I] 6364 Å flux using the method described in Appendix B, and minimizing the RMS of the small scale fluctua-

tions redwards 3000 km s^{-1}, we find a line ratio of 2.9 at 202 and 300 days to give a complete removal of features G and H. This ratio is in agreement with the value of 3 expected for optically thin emission and also with the results from J14.

In the upper right panel we show the decomposed [O I] 6300 Å line profiles at 202 and 300 days, and in the lower left panel we show a comparison to the Mg I] 4571 Å line profile at 300 days. All features except B are clearly identified in both line profiles and the agreement is good. The features on the red side are weaker for the Mg I] 4571 Å line, which is consistent with the larger red-side flux deficit for this line (Fig. 10), but the relative (normalized with the box-averaged line profile) strength of all features are similar. The good agreement suggests that the [O I] 6300 Å and Mg I] 4571 Å lines arise from the same nuclear burning zones. Given the findings in J14 this, in turn, suggests that the Mg I] 4571 Å and [O I] 6300 Å lines arise mainly from the O/Ne/Mg zone, and that the contributions from the O/Si/S and O/C zones to the [O I] 6300 Å flux are modest.

In the lower right panel we show a comparison of the decomposed [O I] 6300 Å line profile and the [O I] 5577 Å, O I 7774 Å and Na I 5890,5896 Å line profiles at 202 days. The E and F features are clearly identified in all of these line profiles, whereas the other features are only seen in the [O I] 6300 Å line profile. Since the E and F features are also the strongest, it is not clear if the absence of the other features is real, or if they are just too faint to be seen. The relative strength of the E and F features are similar for the [O I] 5577 Å, O I 7774 Å and [O I] 6300 Å lines, suggesting that all these lines arise mainly from the same nuclear burning zones, whereas the relative strength of these features for the Na I 5890,5896 Å line is a bit weaker, suggesting contributions from other nuclear burning zones. This is consistent with the results in J14, where all oxygen lines are found to arise from the oxygen zones and the Na I 5890,5896 Å line partly from the O/Ne/Mg zone.

The small scale fluctuations in the [Ca II] 7291,7323 Å line (not shown) do not match very well with those in the [O I] 6300 Å line, and the relative strength of the features seen is weaker. We were not able to correct for blending using repetitions of the features, which makes the interpretation less clear, and removal of the [Ca II] 7323 Å flux assuming a line ratio of 1.5, as expected for optically thin emission, does not improve the agreement with the [O I] 6300 Å line. The result is consistent with the findings in J14, were we found this line to arise mainly from other nuclear burning zones (Si/S). This is also suggested by the different sizes of the line emitting regions discussed in Sect. 3.4.

Shivvers et al. (2013) presented an analysis of the line profiles of the [O I] 6300,6364 Å, O I 7774 Å and Mg I] 4571 Å lines at 268 days. By decomposition of the [O I] 6300,6364 Å line profile into Gaussian profiles, assuming an [O I] 6300,6364 Å line ratio of 3, they found a good fit for one broad and two narrow profiles located at −400 and 1600 km s^{-1}. The two strongest features in our analysis, E and F, are located at ∼0 and ∼1500 km s^{-1}, and likely correspond to the two features found by Shivvers et al. (2013). They also find these features to repeat in the O I 7774 Å and Mg I] 4571 Å lines, in agreement with our analysis. The difference in velocity for the E feature is likely due to the different methods used.

Matheson et al. (2000) presented an analysis of the small scale fluctuations in the line profiles of SN 1993J. They found a good agreement between the fluctuations in the [O I] 6300 Å, [O I] 5577 Å and O I 7774 Å line profiles, which is in agreement

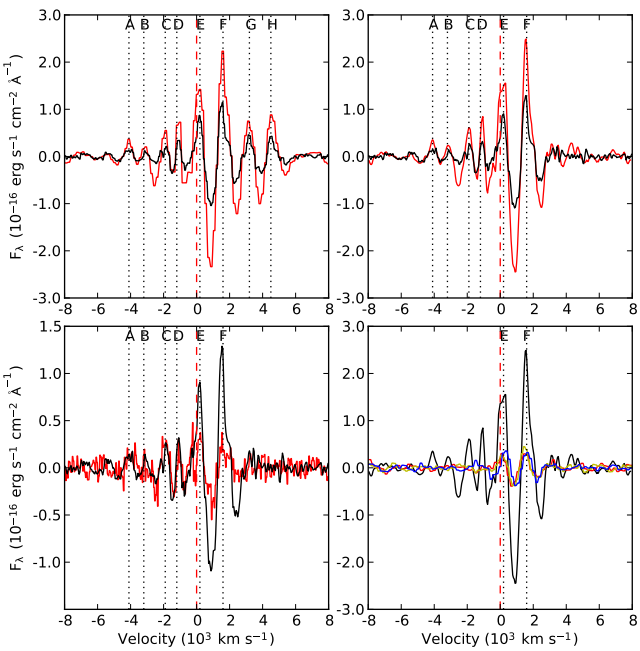

Fig. 16. Comparison of box average subtracted line profiles. The upper left panel shows the [O I] 6300,6364 Å line profile at 202 (red) and 300 (black) days. The upper right panel shows the decomposed [O I] 6300 Å line profile at 202 (red) and 300 (black) days. The lower left panel shows the decomposed [O I] 6300 Å line profile (black) and the Mg I] 4571 Å line profile (red) at 300 days. The lower right panel shows the decomposed [O I] 6300 Å line profile (black) and the [O I] 5577 Å (red), O I 7774 Å (green) and Na I 5890,5896 Å (blue) line profiles at 202 days.

with our results for SN 2011dh. However, they did not find a good agreement between the fluctuations in the [O I] 6300 Å and Mg I] 4571 Å line profiles, which is a bit surprising since we find an excellent agreement for SN 2011dh. One possible explanation is that the [O I] 6300 Å line is dominated by flux from the O/Ne/Mg zone for SN 2011dh, but not for SN 1993J (see above). Filippenko & Sargent (1989) presented an analysis of the small scale fluctuations in the line profiles of the Type Ib SN 1985F. Similar to our analysis they found repetitions of the identified features in the [O I] 6300 and 6364 Å lines, and a line ratio close to 3 using the strongest feature.

Matheson et al. (2000) applied the statistical model by Chugai (1994) to their spectra of SN 1993J, giving a filling factor of ∼0.06 for oxygen zone material, distributed within a sphere with 3800 km s^{-1} radius. Using their estimated typical clump size of 300 km s^{-1}, this corresponds to ∼900 clumps. The model requires the radius of the sphere containing the clumps, the typical size of the clumps and the RMS of relative flux fluctuations in lines originating from the clumps. In the case of SN 2011dh, we adopt a radius of the sphere containing the bulk of the oxygen zone material of ∼3500 km s^{-1}, based on the estimates of the O I and Mg I line emitting regions in Sect. 3.2. For SN 1987A a typical clump size of 120 km s^{-1} was estimated from the power spectrum of the [O I] 6300 Å line by Stathakis et al. (1991), using high-resolution spectroscopy, but it is not clear how this was done by Matheson et al. (2000). As we do not have high-resolution spectroscopy for SN 2011dh, we can only estimate an upper limit on the typical clump size, taken to be 300 km s^{-1}, the smallest size of the features seen. The RMS of the relative flux fluctuations in the inner part (±2000 km s^{-1}, see Chugai

(1994)) of the sphere, for both the decomposed [O I] 6300 Å and the Mg I] 4571 Å lines, was ~0.09 at 300 days. Using these estimates and applying Chugai (1994, eq. 11), we find an upper limit on the filling factor of oxygen zone material (within the sphere) of ~0.07, and a lower limit on the number of oxygen zone clumps of ~900. These values are similar to the values estimated by Matheson et al. (2000) for the clumping of oxygen zone material in SN 1993J.

4. Lightcurve modelling

In this section we discuss modelling of the bolometric and photometric lightcurves with HYDE, a hydrodynamical code described in Ergon et al. (2014b, herafter E14b) and summarized in Appendix D, and the nebular phase spectral synthesis code described in Jerkstrand et al. (2011, 2012) and J14, hereafter referred to as the steady-state NLTE code. In J14 we present spectra for a set of models, and here we present pseudo-bolometric and photometric lightcurves for the same models. HYDE is aimed for bolometric lightcurve modelling, and has the hydrodynamical and time-dependent capabilities needed to evolve the SN through the explosion and the diffusion phase. The steady-state NLTE code is aimed for spectral modelling, and contains solvers for the statistical and thermal equilibrium in each compositional zone, including computation of non-thermal rates and radiative transfer. It assumes steady-state in all equations, and is therefore limited to $\gtrsim$100 days. In this phase, the bolometric luminosity equals the radioactive energy deposition, which can be calculated using either code. Pseudo-bolometric and photometric lightcurves however, depend on the processing of the deposited energy, and can therefore only be calculated with the steady-state NLTE code.

Given the extensive photometric coverage for SN 2011dh, both in time and wavelength, consistent modelling of the lightcurves is highly desirable. Ideally, HYDE would be used to evolve a grid of initial stellar models through a parametrized explosion and the photospheric phase, and the resulting ejecta models then fed into the steady-state NLTE code and subsequently evolved. For the <100 days evolution we use the grid of SN models, constructed with HYDE and MESA STAR (Paxton et al. 2011, 2013), presented in E14b, but to evolve this 15×10×9×9 grid further with the steady-state NLTE code is not computationally feasible. To partly circumvent this problem we use two different methods. First, to extend the temporal coverage of the J14 steady-state NLTE models to early times, we evolve these through the <100 days period using HYDE in homologous mode. Secondly, to extend the temporal coverage of the hydrodynamical model grid to 400 days, we apply a bolometric correction (BC) determined with the steady-state NLTE code. Finally, after 600 days time-dependent effects becomes important (Sect. 5.1), and a steady-state assumption is no longer valid, so in this phase neither code apply.

4.1. Hydrodynamical modelling of the <100 days bolometric lightcurve

B12 presented a hydrodynamical model for SN 2011dh, that well reproduced the observed <100 days bolometric lightcurve and photospheric velocity evolution. Here we use the grid of SN models constructed with HYDE and MESA STAR (Paxton et al. 2011, 2013), presented in E14b, and the procedure described therein, to fit the <100 days UV to MIR pseudo-bolometric lightcurves and photospheric velocities of SNe 2011dh, 1993J and 2008ax. The UV to MIR BC is assumed to be negligible, and is likely >−0.15 mag at <100 days (Appendix C). The strength of the method, as compared to previous hydrodynamical modelling, is the ability to determine the errors in the model parameters arising from the uncertainties in the observed quantities, and the degeneracy of the solutions, issues previously discussed in E14a from approximate considerations. The progenitor and SN parameters are the helium core mass (M_{He}), the explosion energy (E), the mass of ^{56}Ni (M_{Ni}) and the distribution of it (Mix_{Ni}). The stellar models consists of bare helium cores without a hydrogen envelope, which is sufficient to determine the explosion energy, helium core mass and mass and distribution of the ^{56}Ni (E14b). This approximation is sound as long as the optical depth of the hydrogen envelope is $\ll$1, and the mass low enough not to (appreciable) decelerate the helium core. In the fit, equal weights are given to the diffusion phase lightcurve, the early tail lightcurve and the early photospheric velocity evolution. To estimate the radius, as done by B12, modelling of the early cooling phase, which depends on the hydrogen envelope, would be necessary, which is outside the scope of this paper. The UV to MIR pseudo-bolometric lightcurves for SNe 1993J and 2008ax, were constructed by assuming the same UV and MIR fractions as for SN 2011dh.

The upper and middle panels of Fig. 17 show the best-fit model bolometric lightcurve and photospheric velocity evolution, as compared to the observed UV to MIR pseudo-bolometric lightcurve and velocity evolution for the absorption minimum of the Fe II 5169 Å line for SNe 2011dh, 2008ax and 1993J. Table 3 gives the helium core mass, explosion energy, mass of ^{56}Ni and the distribution of it for the best-fit models, and the corresponding errors, calculated as described in E14b. A systematic error of 15 percent in the photospheric velocities has been assumed, which is similar to the average difference between the absorption minimum of the Fe II 5169 Å line and the thermalization radius, as estimated from blackbody fits for SN 2011dh (E14a). This error mainly propagates to the helium core mass and explosion energy, whereas the errors in the distance and extinction mainly propagate to the mass of ^{56}Ni (E14b). The derived parameters for SN 2011dh are in good agreement with the results in B12. The helium core mass and explosion energy derived for SNe 1993J and 2008ax are similar to what is derived for SN 2011dh, whereas the mass of ^{56}Ni differs significantly. The mixing of the ^{56}Ni is strong for all three SNe, and for SN 2011dh the fraction of ^{56}Ni outside 3500 and 6000 km s^{-1} is 53 and 8 percent, respectively. This is in rough agreement with the preferred steady-state NLTE model, although in this model the ^{56}Ni is confined within 6000 km s^{-1}. The derived explosion energy for SN 1993J is about half of that obtained in previous hydrodynamical modelling (e.g. Shigeyama et al. 1994). This is likely a consequence of the bare helium core approximation, as the more massive hydrogen envelope for this SN takes up about half of the explosion energy (Shigeyama et al. 1994). Assuming the absence of a hydrogen envelope to affect the photospheric velocity evolution but not the lightcurve, the helium core mass for SN 1993J would be underestimated by ~20 percent, and be closer to 4 than 3 $M_\odot$. We note that the velocity evolution of SN 2008ax is not well fitted, which could be explained by a worse correspondence between the absorption minimum of Fe II 5169 Å line and the photosphere, as compared to SNe 2011dh and 1993J.

The lower panels of Fig. 17 show contour plots of the standard deviation in the fit, normalized to that of the best-fit model, as a function of helium core mass and explosion energy. We also show the constraints M_{ej}^2/E=const and M_{ej}/E=const provided by

Table 3. Explosion energy, helium core mass, mass of the ^{56}Ni and the distribution of it for the best-fit models of SNe 2011dh, 1993J and 2008ax.

SN	E (10^{51} erg)	M_{He} ($M_\odot$)	M_{Ni} ($M_\odot$)	Mix_{Ni}
2011dh	0.55 (+0.35,-0.28)	3.31 (+0.60,-0.52)	0.075 (+0.028,-0.020)	1.05 (+0.10,-0.00)
2008ax	0.75 (+0.50,-0.38)	3.06 (+0.56,-0.44)	0.181 (+0.078,-0.105)	0.85 (+0.06,-0.03)
1993J	0.60 (+0.40,-0.30)	3.19 (+0.51,-0.50)	0.106 (+0.034,-0.028)	0.88 (+0.23,-0.12)

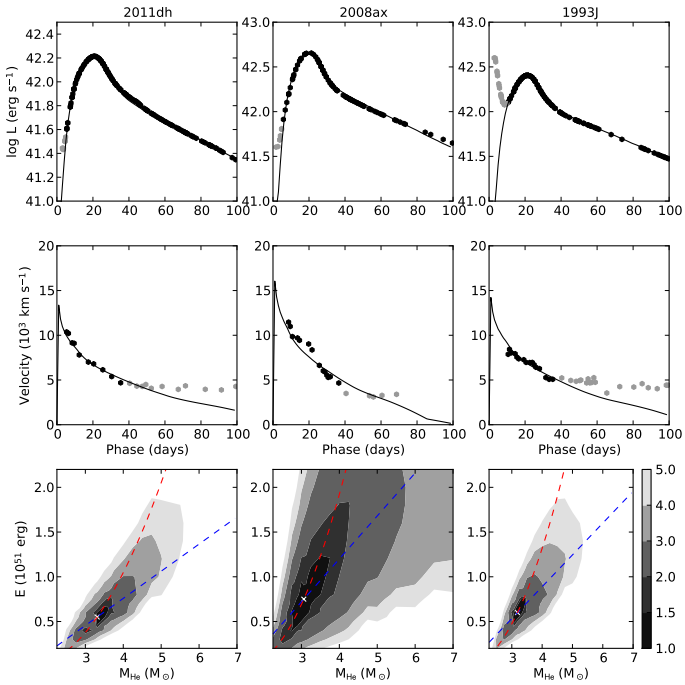

Fig. 17. Upper and middle panels: Bolometric lightcurve (upper panels) and photospheric velocity evolution (middle panels) for the best-fit models, as compared to the observed UV to MIR pseudo-bolometric lightcurve and velocity evolution for the absorption minimum of the Fe II 5169 Å line for SNe 2011dh (left panels), 2008ax (middle panels) and 1993J (right panels). Observations not included in the fit are displayed in grey. Lower panels: Contour plots showing the (grey-scale coded) standard deviation in the fits, normalized to that of the best-fit model, projected onto the E-M_{He} plane for SNe 2011dh (left panels), 2008ax (middle panels) and 1993J (right panels). We also show the constraints M_{ej}/E=const (blue) and M_{ej}^2/E=const (red) provided by the photospheric velocity evolution and the bolometric lightcurve, respectively.

the lightcurve and the photospheric velocity evolution, respectively (E14b). The less good fit of the photospheric velocity evolution for SN 2008ax is reflected in an extended degeneracy region, mainly along the M_{ej}^2/E=const curve. If we assume a good fit to correspond to a normalized standard deviation of <2, and also take into account the errors arising from the observed quantities (Table 3), we find an upper limit on the helium core mass for all three SNe of $\lesssim$4 $M_\odot$, corresponding to an upper limit on the initial mass of $\lesssim$15 $M_\odot$.

4.2. NLTE modelling of the 100-500 days pseudo-bolometric and photometric lightcurves.

Here we compare the pseudo-bolometric and photometric lightcurves for the J14 steady-state NLTE models to the observed 100-500 days pseudo-bolometric and photometric lightcurves. These models span a restricted volume of parameter space, and the degeneracy of the solution and the errors in the model parameters can not be quantified. The preferred model, presented in J14, and refined in this paper with respect to dust, has been chosen to give the best agreement with both nebular spectra and the bolometric and photometric lightcurves. In J14 we discuss the constraints on the model parameters provided by the nebular spectra, and here we discuss the constraints provided by the pseudo-bolometric and photometric lightcurves. The set of models (J14, table 3) varies in the following parameters: initial mass (12, 13 or 17 $M_\odot$), macroscopic mixing (medium or strong), density contrast (low or high), positron trapping (local or non-local), molecule cooling (complete or none) and dust (τ_{dust}=0 and 0.25). In this work we restrict ourself to the model families differing in a single parameter (J14, table 4), and two additional models (12E and 12F) described in Appendix C.7. These models differ from model 12C only in the absence (12E) and the properties (12F) of the dust. The effects of the model parameters on the model lightcurves are discussed in in Appendix C.

4.2.1. Model parameters

The initial mass parameter determines the ejecta mass, the density profile and the abundances. The 12, 13 and 17 $M_\odot$ models are constructed using results from 1-D stellar evolutionary and hydrodynamical modelling. The abundances are taken from Woosley & Heger (2007) and the ejecta divided into a core, a helium envelope (density profile from B12; private communication) and a hydrogen envelope ($\rho \propto v^{-6}$). The interfaces between these are fixed in velocity space at 3500 and 11000 km s^{-1}, based on observations and modelling (E14a, this paper), which determines the kinetic energy. The mass of ^{56}Ni is not varied in the models, and is fixed to 0.075 $M_\odot$ based on hydrodynamical modelling (B12, this paper). The macroscopic mixing and density contrast parameters mimics effects on the ejecta structure arising in multi-D hydrodynamical modelling. Macroscopic mixing of the nuclear burning zones occurs in the explosion due to hydrodynamical instabilities, and is represented in a statistical sense as a fully mixed core of constant average density. Incomplete mixing of the core, as we found evidence for in Sect. 3.4, have not been investigated. The strong mixing models differs from the medium mixed models only in that 50 percent of the Fe/Co/He material is mixed into the helium envelope. Expansion of the Fe/He/Co clumps occurs at early times due to radioactive heating, and is represented as a density contrast be-

tween the Fe/Co/He clumps and the surrounding material. The positron trapping parameter mimics the effect of a strong magnetic field on the positron opacity, assumed to be high enough in the presence of a magnetic field for the positrons to be locally absorbed. The modelling does not include a self-consistent treatment of the formation of molecules and dust in the ejecta, but the effects of these are included in a simplified way as described in Appendices C.5 and C.7. The effect of molecules is represented as the fraction of the cooling in the O/C and O/Si/S zones going into molecule (CO and SiO) emission. Dust absorption is represented as a grey absorptive opacity in the core, and the emission as blackbody emission, the temperature determined as described in Appendix C.7.

4.2.2. The preferred model.

The preferred model presented in J14 (12C) has an initial mass of 12 $M_\odot$, strong macroscopic mixing, local positron trapping, no molecule cooling, dust with $\tau_{\rm dust}$=0.25 and a high density contrast. However, in this work we use a refined version of the preferred model (12F), which differs only in the optical depth ($\tau_{\rm dust}$=0.44) and the temperature of the dust (Appendix C.8). The prefix "preferred" is used to distinguish from a best-fit model, as the one discussed in Sect. 4.1. It should be noted, that the good spectroscopic agreement found for model 12C in J14 does not necessarily apply to model 12F. However, for lines originating from the core, which are expected to be most affected by the higher optical depth of the dust, the flux would be ~17 percent lower and the blue-shifts ~100 km s^{-1} higher (Sect. 3.5), so the differences are likely to be small. Figures 18 and 19 show the 100-500 days preferred model and observed pseudo-bolometric lightcurves. In these figures and a number of figures that follows, we have normalized the luminosity with the decay chain luminosity of the mass of ^{56}Ni, which (to first order) removes the dependence on this quantity (Appendix C). The preferred model shows a good agreement with observations, the differences being $\lesssim$10 and $\lesssim$15 percent for the optical and optical to MIR pseudo-bolometric lightcurves, respectively. However, after ~400 days the observed optical pseudo-bolometric lightcurve flattens and starts to diverge from that of the preferred model. This flattening continues after 500 days and is discussed in Sect. 5.1. Figure 20 shows the preferred model and observed photometric lightcurves. The preferred model shows an overall good agreement with observations, the differences being mostly $\lesssim$0.3 mag, but there are some notable exceptions, as the U and S_2 bands. The discrepancy seen in the optical pseudo-bolometric lightcurve after ~400 days is also reflected in the B, g and V bands. The U band is particularly sensitive to the extinction, so the overproduction of this band could be an indication that the adopted value needs to be revised. The discrepancy decreases with time though, so the interpretation is not clear. The discrepancy in the S_2 band is discussed further in Sect. 4.2.4.

4.2.3. Calculation of the <100 days bolometric lightcurves with HYDE

Only after ~100 days, steady-state is satisfied and the NLTE code can be used. Therefore we use HYDE in homologous mode to produce 3-100 days bolometric lightcurves for the J14 models. The J14 models are first (homologously) rescaled to day one, and then evolved with HYDE through the 1-100 days evolution. The initial temperature profile at 1 day is adopted from the best-fit hydrodynamical model for SN 2011dh (Sect. 4.1),

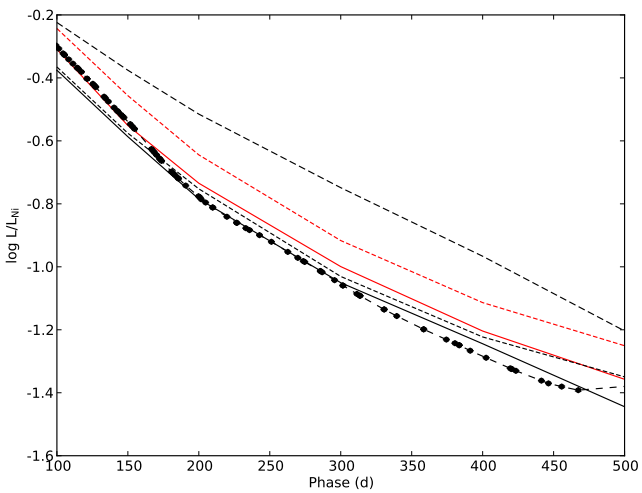

Fig. 18. The 100-500 days observed (black circles) and J14 model optical to MIR pseudo-bolometric lightcurves normalized to the radioactive decay chain luminosity of 0.075 $M_\odot$ of ^{56}Ni. Selected representatives (12A,12F,13A,13C,17A) of the model families differing in initial mass and macroscopic mixing are shown and displayed as follows: 12 $M_\odot$ (solid lines), 13 $M_\odot$ (short dashed lines), 17 $M_\odot$ (long dashed lines), medium mixing (red), strong mixing (black).

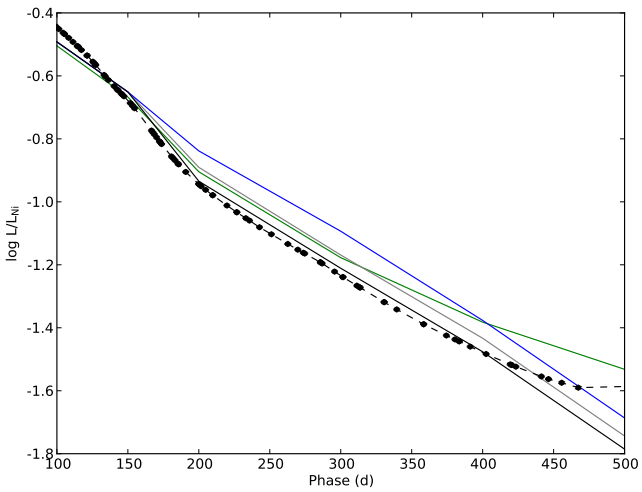

Fig. 19. The 100-500 days observed (black circles) and J14 model optical pseudo-bolometric lightcurves normalized to the radioactive decay chain luminosity of 0.075 $M_\odot$ of ^{56}Ni. The preferred model (12F; black solid line), model 12C (grey solid line) and model 12E (blue solid line), which differ only in the optical depth (12F; 0.44, 12C; 0.25, 12E; 0) and temperature of the dust, are shown together with model 12B (green solid line), which differs from model 12C only in the positron trapping (12C; local, 12B; non-local).

with the mixing of the ^{56}Ni adjusted to match that of the J14 models. The subsequent evolution is not sensitive to the choice of initial temperature profile, as it is powered by the continuous injection of radioactive decay energy. Figure 21 shows the 3-100 days bolometric lightcurves for the J14 model families differing in initial mass and macroscopic mixing, as compared to the observed optical to MIR pseudo-bolometric lightcurve. The other steady-state NLTE model parameters have no or negligible influence on the bolometric lightcurve (Appendix C). The optical to MIR BC for the J14 models is likely >−0.15 mag during this period (Appendix C), so the comparison is justified. The preferred model shows an overall agreement with observations, although

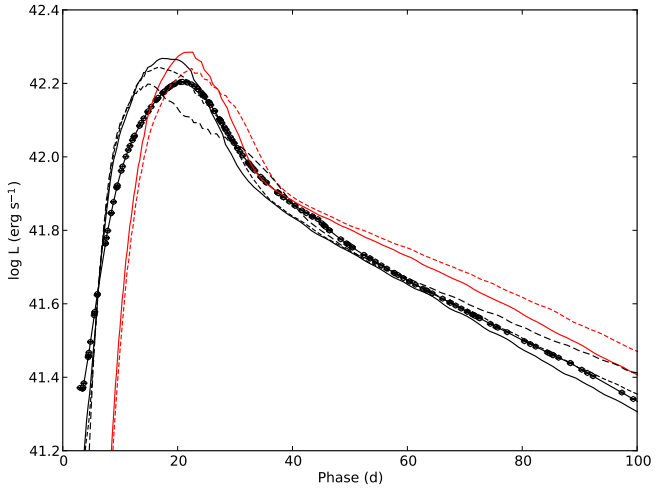

Fig. 21. The <100 days observed (black circles) and J14 model bolometric lightcurves as calculated with HYDE. The model families differing in initial mass and macroscopic mixing are shown and displayed as follows: 12 $M_\odot$ (solid lines), 13 $M_\odot$ (short dashed lines), 17 $M_\odot$ (long dashed lines), medium mixing (red), strong mixing (black).

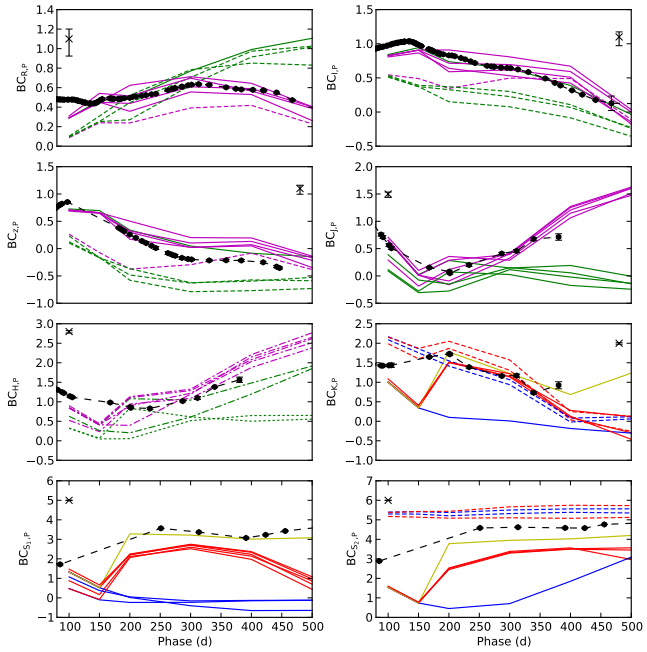

Fig. 22. The 100-500 days observed (black circles) and J14 model pseudo-BCs for selected bands and selected parameter families. The model parameter families are displayed as follows: complete molecule cooling (dashed lines), no molecule cooling (solid lines), high density contrast (dotted lines), low density contrast (dashed-dotted lines), local positron trapping (magenta), non-local positron trapping (green), $\tau_{\rm dust}$=0 (blue), $\tau_{\rm dust}$=0.25 (red), $\tau_{\rm dust}$=0.44 (yellow). 17 $M_\odot$ and medium mixing models are not displayed. To help reading the figures we display fitted magnitudes (Sect. 2.1) for well sampled bands. The error bars arising from the extinction is marked in the upper left or right corner.

the peak occurs a few days earlier and is overproduced by ~0.2 mag.

4.2.4. Constraints on the model parameters

The effects of the model parameters on the lightcurves are discussed in Appendix C, and here we discuss the constraints obtained from those on our choice of model parameters. As explained in Appendix C, a split of the lightcurve into a bolometric lightcurve and a BC, is useful for the analysis. The bolometric lightcurve depends only on the energy deposition, whereas the BCs depend on how this energy is processed. The energy deposition is independent of molecule cooling and dust and, within the parameter space covered by the J14 models, only weakly dependent on the density contrast and the positron trapping (Appendix C). Therefore the bolometric lightcurve depends significantly only on the initial mass and macroscopic mixing, whereas the BCs may depend on all model parameters. Observationally, the split into a bolometric lightcurve and a BC is not straightforward, as we do not know the former and can not calculate the latter. Natural substitutes are the optical to MIR pseudo-bolometric lightcurve and the quantity $BC_{X,P} = M_{Bol,P} - M_X$, which we will refer to as pseudo-BC, where $M_{Bol,P}$ is the optical to MIR pseudo-bolometric magnitude (Appendix C). As the spread among the model optical to MIR BCs is <±0.1 mag during the 100-400 days period (Appendix C), these quantities are well suited to trace the effects on the bolometric lightcurve and the BCs. Figure 22 shows the pseudo-BCs for selected bands and selected parameter model families. Keep in mind that, according to our definition, a larger pseudo-BC corresponds to a higher flux.

Initial mass Affects both the bolometric lightcurve and the BCs. Comparison of the <500 days model and observed optical to MIR pseudo-bolometric lightcurves clearly excludes the 17 $M_\odot$ model (Figs. 18 and 21). Due to larger optical depths for the thermal radiation and the γ-rays in this model, neither the diffusion peak (too wide) nor the late tail luminosity (too high) is well reproduced. There is no 17 $M_\odot$ model with medium mixing, but this would only increase the discrepancy (see below). The [O I] 6300,6364 Å line, which is sensitive to the initial mass (J14), contributes ~50 percent of the R-band flux, and the effect on BC_R is <0.41 mag. There is however a degeneracy with the effects of molecular cooling and positron trapping in the R band (Appendices C.4 and C.6), and neither $BC_{R,P}$ nor the other pseudo-BCs show a clear separation of the model families differing in initial mass. The effect on the [O I] 6300,6364 Å flux is larger than on the BC, and corresponds to a ~1 mag difference in the R-band magnitudes. As seen in Fig. 20, the R-band magnitudes show a clear separation of the 17 $M_\odot$ and 12-13 $M_\odot$ model families. At <300 days the constraint from the R-band lightcurve on the initial mass, is at least as good as the one obtained from the optical to MIR pseudo-bolometric lightcurve. The choice of the initial mass is mainly motivated by the agreement with nebular spectra discussed in J14, but the optical to MIR pseudo-bolometric and R-band lightcurves seem to exclude a 17 $M_\odot$ model.

Macroscopic mixing Affects both the bolometric lightcurve and the BCs. Comparison of the <500 days model and observed optical to MIR pseudo-bolometric lightcurves clearly excludes medium mixing models (Figs. 18 and 21). Due to the more centrally concentrated Fe/Co/He material in these models, the rise to peak luminosity is much worse reproduced (too late), and the late tail luminosity also differs (too high). The effect on the BCs is mostly small (Appendix C.2), and none of the pseudo-BCs show a clear separation of the model families differing in macroscopic mixing. The choice of strong mixing is motivated by the

optical to MIR pseudo-bolometric lightcurve, and in particular the rise to peak luminosity. Naively this is in contradiction with the small size of the Fe/Co/He line emitting region (Sect. 3.2). However, the amount of high velocity Fe/Co/He material does not necessarily need to be high to reproduce the rise to peak luminosity, and further modelling is needed to resolve this issue.

Density contrast Only significantly affects the BCs. In general the effect on the BCs is small, but there is a strong effect on BC_H at >300 days, caused by the [Si I] 16450 Å line. However, there is a degeneracy with a similar effect on BC_H, caused by the positron trapping (see below), and it is not possible to constrain the density contrast alone. Our NIR coverage ends at ~400 days, but the observed evolution of $BC_{H,P}$ does not favour models with low density contrast and non-local positron trapping (Fig. 22). The choice of a high density contrast is mainly motivated by the agreement with nebular spectra discussed in J14, and is also consistent with the upper limit on the oxygen zone filling factor of ~0.07, derived from small scale fluctuations in the [O I] 6300,6364 Å and Mg I] 4571 Å lines (Sect. 3.6).

Positron trapping Only significantly affects the BCs. The effect is quite prominent at late times, when the positrons start to dominate the energy deposition, because locally trapped positrons deposit all their energy in the low temperature Fe/Co/He zone. This results in redder emission, and the luminosity of lines originating from this zone is boosted, whereas the luminosity of lines originating from other zones is reduced. Due to this, the optical BC (and thus the optical pseudo-bolometric lightcurve) decreases faster at >300 days for models with local trapping, which is in better agreement with the observed optical pseudo-bolometric lightcurve (Fig. 19). At >400 days, the observed optical decline rate starts to decrease, however, and models with local positron trapping start to diverge from observations. As discussed in Sect. 5.1, this could be a sign of additional energy sources, and is not necessarily in conflict with a scenario with locally trapped positrons. We find particularly strong line effects in BC_J and BC_H at >300 days, caused by the [Fe II] 12567 Å and [Fe II] 16440 Å lines, respectively. As discussed above, the effect on BC_H is degenerate with a similar effect caused by the density contrast. Our NIR coverage ends at ~400 days, but the observed evolution of $BC_{J,P}$ seems to be in better agreement with models with local positron trapping (Fig. 22). The choice of local positron trapping is motivated by the optical pseudo-bolometric lightcurve and the evolution of $BC_{J,P}$ at 300-400 days, although the decreasing optical decline rate observed at >400 days is a caveat. The constraints obtained from nebular spectra are not conclusive (J14).

Molecule cooling Only affects the BCs and results in a redistribution of cooling emission from the O/C and O/Si/S zones to the CO and SiO molecular bands. Our simplified treatment is described in Appendix C.5. The effect is strong in the S_2 band, which overlaps with the CO fundamental and SiO first overtone bands, and there is also a significant effect in the K band, which overlaps partly with the CO first overtone band. Both of these effects are degenerate with the effect of dust, but as we have NIR spectra we can disentangle the molecule and dust contributions in the K band. The CO first overtone emission detected at 206 days, and possibly at 89 days (Sect. 3.3), implies some amount of CO cooling in the O/C zone, but is ~2.5 and ~3.5 mag too faint, respectively, as compared to models with complete molecule cooling. Therefore the amount of CO cooling is either small or the CO fundamental to first overtone band ratio differs from that assumed in the models (Appendix C.5). The contribution from CO first overtone emission to the observed K-band flux is negligible (Sect. 3.3), so the observed excess in this band (Fig. 22) is rather due to dust. As compared to models with complete molecule cooling (with or without dust), the observed $BC_{S_2,P}$ is ~2 and 0.5-1.0 mag too small at 85 and >251 days (Fig. 22). On the other hand, as compared to the preferred model (without molecule cooling, but with dust), which shows the best agreement in the K and S_1 bands for a conceivable dust component (see below), the observed $BC_{S_2,P}$ is 0.5-1.0 mag too large (Fig. 22). As molecule emission in the S_2 band is likely to be dominated by the CO fundamental band (Appendix C.6), this suggests a small amount of CO cooling in the O/C zone at 85 days, increasing to an intermediate amount at >251 days. As compared to models with neither dust nor molecule cooling, the observed $BC_{S_2,P}$ is 2-4 mag too large, and these seem to be excluded (Fig. 22). We find particularly strong line effects in BC_I and BC_z at <300 days caused by the Ca II 8498,8542,8662 Å and [C I] 8727 Å lines. The former is affected by SiO cooling and the latter by CO cooling, but as both contribute to both the I and z bands, these effects can not be disentangled. The observed evolution of $BC_{I,P}$ and $BC_{z,P}$, shows a better agreement with models without molecule cooling (Fig. 22). This constraint is strong only at early times ($\lesssim$250 days), and as the constraint from the S_2 band suggests a substantial amount of CO cooling only at late times ($\gtrsim$250 days), a scenario where the amount of CO cooling is increasing with time is possible. We have chosen no molecule cooling for the preferred model, but neither this scenario nor complete molecule cooling shows a satisfactory agreement with observations, and in the O/C zone an intermediate amount of CO cooling, possibly increasing with time, seems likely.

Dust Only affects the BCs. As the dust absorbs the still quite hot radiation from the SN and re-emit it at a much lower temperature, there is a general tendency for decreased optical emission and increased K and MIR emission. Our simplified treatment is described in Appendix C.7, where the optical pseudo-bolometric lightcurve is used to constrain the optical depth, and fits to the K and S_1 bands are used to constrain the temperature. CO first overtone emission contributes negligible to the K band flux (Sect. 3.3), so the observed excess in this band can be solely attributed to dust emission. The preferred model (12F) and the original J14 models with dust, differ in the optical depth and the method used to determine the temperature. The preferred model has $\tau_{\rm dust}$=0.44 and the temperature is determined for each individual epoch, whereas the original J14 models with dust have $\tau_{\rm dust}$=0.25 and the temperature is constrained to scale as for a homologously expanding surface. In the preferred model, the optical BC becomes ~0.3 mag smaller at 200 days, roughly corresponding to the optical depth of the dust, and simultaneously, BC_K and the MIR BCs become ~1 and ~3 mag larger, respectively. The preferred model shows an overall good agreement with observations, and well reproduces the drop in the optical pseudo-bolometric lightcurve (Fig. 19) and the increase in $BC_{K,P}$ and $BC_{S_1,P}$ (Fig. 22), although the original J14 models with dust also qualitatively reproduce this behaviour. This shows, most importantly, that not only are the drop in the optical pseudo-bolometric lightcurve and the increase in BC_K and the MIR BCs simultaneous, the absorbed luminosity is also in good agreement with the emitted. The observed $BC_{S_2,P}$ is 0.5-1.0 mag too small

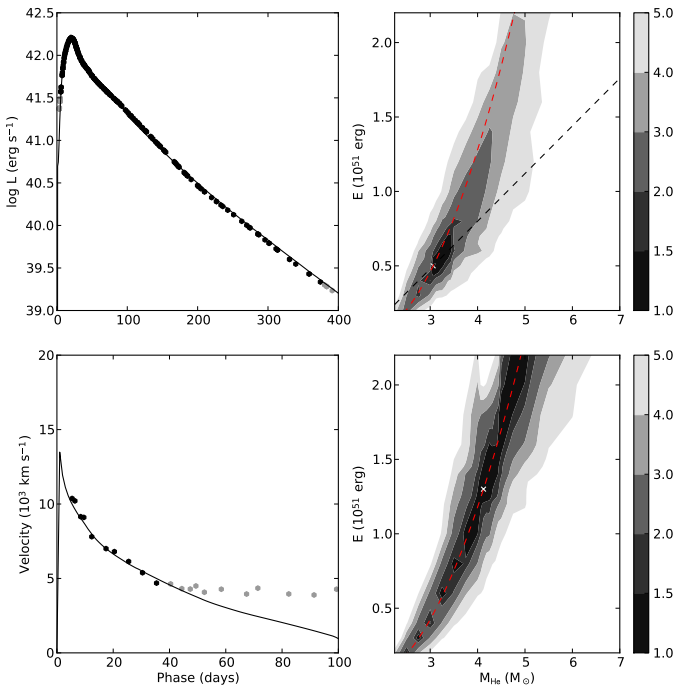

Fig. 23. Left panels: Optical to MIR pseudo-bolometric lightcurve (upper left panel) and photospheric velocity evolution (lower left panel) for the best-fit model as compared to the observed optical to MIR pseudo-bolometric lightcurve and velocity evolution for the absorption minimum of the Fe II 5169 Å line for SN 2011dh. Observations not included in the fit are displayed in grey. Right panels: Contour plots showing the (grey-scale coded) standard deviation in the fit, normalized to that of the best-fit model, projected onto the E-M_{He} plane for the case where the photospheric velocities were used (upper right panel) and not used (lower right panel). We also show the constraints M_{ej}/E=const (blue) and M_{ej}^2/E=const (red) provided by the photospheric velocity evolution and the bolometric lightcurve, respectively.

as compared to the preferred model which, as discussed above, suggests a contribution from molecule emission.

4.3. Hydrodynamical modelling of the <400 days bolometric lightcurve

Here we extend the temporal coverage of the hydrodynamical model grid to 400 days (which is the period for which we have full U to S_2 coverage), and make a fit of the observed optical to MIR pseudo-bolometric lightcurve of SN 2011dh to this extended model grid. The 100-400 days bolometric lightcurves are calculated using HYDE, whereas the 100-400 days optical to MIR BCs are determined with the steady-state NLTE code. In this phase we run HYDE in homologous mode, ignore the radiative transfer, and take the bolometric luminosity as the deposited radioactive decay energy (see Appendix C). As in Sect. 4.1, we assume the optical to MIR BC to be negligible during the 0-100 days period. The fitting is done by minimization of the square of the relative residuals, giving equal weights to the diffusion phase lightcurve, the early tail lightcurve, the late tail lightcurve and the early photospheric velocity evolution.

To determine how the BC varies in the parameter space of the hydrodynamical model grid is not computationally feasible. Instead, we take advantage of the fact that the BC varies with <±0.1 mag between the J14 steady-state NLTE models during the 100-400 days period (Appendix C), and use the BC for the preferred steady-state NLTE model for all hydrodynamical models. However, as the J14 models cover a restricted volume of the hydrodynamical parameter space, we need to justify this choice further. It is reasonable to assume that the BC depends mainly on the energy deposition per unit mass (determining the heating rate) and the density (determining the cooling rate). Furthermore, we know beforehand, that models giving a bad <100 days fit will not give a good <400 days fit. Inspecting the J14 models and the hydrodynamical models with a normalized standard deviation in the <100 days fit less than 3, we find that these hydrodynamical models do not span a wide range in (mass averaged) density or energy deposition per mass, and that the J14 models cover about half of this region. Although these quantities evolve quite strongly with time, they scale in a similar way for all models, and this conclusion holds for the full 100-400 days period. The effect of not varying the steady-state NLTE parameters that do not map onto the hydrodynamical parameter space (dust, molecule cooling, positron trapping and density contrast) is harder to constrain. The small spread in the BC for the J14 models during the 100-400 days period, make this caveat less worrying though.

The left panels of Fig. 23 show the best-fit model optical to MIR pseudo-bolometric lightcurve and photospheric velocity evolution, as compared to the observed optical to MIR pseudo-bolometric lightcurve and velocity evolution for the absorption minimum of the Fe II 5169 Å line. The parameters of the best-fit model are E=$0.50^{+0.42}_{-0.22}\times10^{51}$ erg, M_{He}=$3.06^{+0.68}_{-0.44}$ $M_\odot$, M_{Ni}=$0.075^{+0.028}_{-0.020}$ $M_\odot$ and Mix_{Ni}=$0.95^{+0.06}_{-0.04}$, in good agreement with the results from the <100 days bolometric lightcurve. The upper right panel of Fig. 23 shows a contour plot of the standard deviation in the fit, normalized to that of the best-fit model, as a function of helium core mass and explosion energy. The solution is slightly better constrained in helium core mass and slightly worse constrained in explosion energy, as compared to the <100 days fit, which probably just reflects the smaller weight given to the photospheric velocities. The lower right panel of Fig. 23 show the corresponding contour plot for the case when the fitting was done using the lightcurve alone. As discussed in E14b such a fit is completely degenerate along the M_{ej}^2/E=const curve for the <100 days lightcurve, and apparently this is also the case for the <400 days lightcurve. The main achievement using the <400 days lightcurve is to prove that we get a good fit and similar best fit values as for the <100 days lightcurve. Among other things this shows that other isotopes than ^{56}Co do not contribute substantially before 400 days.

5. Discussion

5.1. The >500 days lightcurves

Figure 24 shows the >200 days observed optical to MIR, optical plus MIR (excluding NIR), optical and MIR pseudo-bolometric lightcurves, as compared to the bolometric lightcurve, deposited ^{56}Co γ-ray and positron luminosity and deposited ^{57}Co luminosity for the preferred steady-state NLTE model. The best-fit hydrodynamical model produces very similar results. Between 467 and 601 days there are no observations and we can only speculate about the evolution, but between 601 and 732 days there is both optical and MIR observations. It is evident from the figure, that the deposited ^{56}Co luminosity is dominated by the positron contribution after ~450 days, and that the observed >600 days lightcurves are unlikely to be powered by the γ-rays emitted in the ^{56}Co decay. Shivvers et al. (2013) suggested that the SN has entered a phase powered by the positrons emitted in the ^{56}Co de-

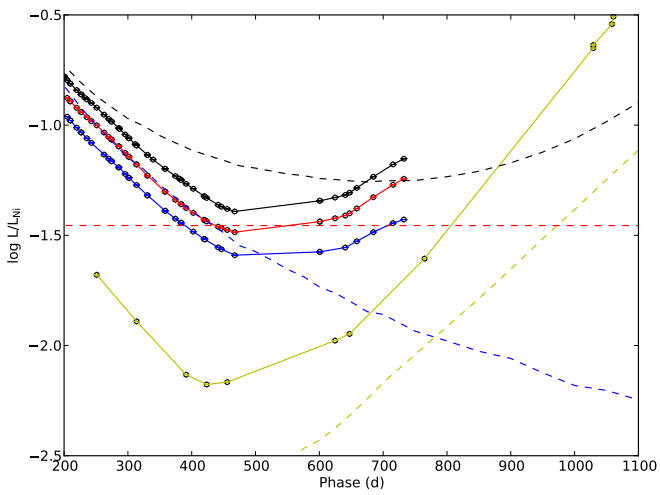

Fig. 24. The >200 days optical to MIR (black dots), optical plus MIR (red dots), optical (blue dots) and MIR (yellow dots) pseudo-bolometric lightcurves, as compared to the bolometric lightcurve (black dashed line), deposited ^{56}Co γ-ray (blue dashed line) and positron (red dashed line) luminosity and deposited ^{57}Co luminosity (yellow dashed line) for the preferred steady-state NLTE model (12F). The lightcurves have been normalized to the radioactive decay chain luminosity of 0.075 M$_\odot$ of ^{56}Ni.

cay after 300-350 days. Given our results, this suggestion seems to be roughly correct in the sense that the positron contribution dominates the deposited luminosity after ~450 days. However, as we discuss below, it is not clear that the positron contribution dominates the emitted luminosity, because there is a number of processes that could provide additional energy.

There is evidence for additional energy sources from the observed pseudo-bolometric lightcurves. The decline rates of the optical and optical to MIR pseudo-bolometric lightcurves are 0.0095 and 0.0088 mag day^{-1}, respectively, for the 467-601 days period, and 0.0069 and 0.0061 mag day^{-1}, respectively, for the 601-732 days period. The decline rate of the MIR pseudo-bolometric lightcurve is 0.0069, 0.0031 and 0.0006, for the 456-625, 625-765 and 765-1061 days periods, respectively. All pseudo-bolometric lightcurves show a trend of continued flattening, and the decline rates eventually become significantly lower than the decay rate of ^{56}Co. In particular, the MIR pseudo-bolometric lightcurve becomes almost flat after ~750 days. The evolution for the J14 models after 500 days was not discussed in Sect. 4.2, but all models show a decrease in the optical and optical to MIR BCs, corresponding to redder emission. This decrease is particularly strong for models with local positron trapping (as the preferred model), due to the increasing contribution from the low temperature Fe/Co/He zone. Assuming the bolometric luminosity of the preferred model to be a reasonable estimate of the actual bolometric luminosity, the actual optical and optical to MIR BCs would increase with ~0.6 mag between 467 and 732 days, which is in strong conflict with the behaviour of the models. Assuming instead, that the actual BCs do not increase, the actual bolometric luminosity at 732 days would be $\gtrsim$0.6 mag higher than the radioactive energy deposition in the preferred model. Even if we ignore the BCs, the observed optical plus MIR luminosity at 732 days equals the radioactive energy deposition in the preferred model, and the observed MIR luminosity at 1060 days is 1.1 mag higher. So both the observed decline rates and the observed luminosities suggest that additional energy sources are needed to power the >600 days lightcurves. Note that the flattening seems to begin at ~400 days, both in the MIR and the optical, so additional energy sources could be contributing already at this epoch.

If the recombination time scales become longer than the time scale of the ^{56}Co decay, the steady-state assumption required for the NLTE modelling is no longer valid. Some fraction of the deposited radioactive decay energy will then build up a reservoir of ionization energy, which through recombination emission could eventually dominate the emitted luminosity. This process, called freeze-out, is expected to occur first in the hydrogen and then in the helium envelope, and is an example of time-dependent effects that might violate the steady-state assumption in late phases. We use a time-dependent NLTE code (Kozma & Fransson 1992, 1998a,b) to test this assumption, and find that time-dependent effects start to become important at ~600 days, and after ~800 days they provide a dominant and increasing contribution to the optical flux. In the particular model tested, which is similar to the preferred model, this contribution is not enough to reproduce the observed lightcurves. However, due to clumping or asymmetries, low density components may exists in the ejecta, for which freeze-out would occur earlier. The 678 day spectrum of SN 2011dh presented by Shivvers et al. (2013), shows features not present in our last optical spectra that could be identified as the He I 6678 Å and 7065 Å lines, whereas the strong feature identified as Na I 5890,5896 Å by the authors could have a significant contribution from, or be fed by, the He I 5876 Å line. The possible presence of these lines is consistent with a substantial contribution from helium recombination emission due to freeze-out in the helium envelope.

CSM interaction became the dominant energy source at ~300 days for SN 1993J, giving rise to broad box-like Hα and Na I 5890,5896 Å lines and a considerable flattening of the lightcurves. The 678 day spectrum of SN 2011dh shows a feature that Shivvers et al. (2013) interpret as broad box-like Hα emission, but no broad box-like Na I 5890,5896 Å emission is seen. The interpretation of the broad feature as Hα emission is far from clear, as a number of other lines may contribute in this wavelength range (including the [N II] 6548,6583 Å line discussed in Sect. 3.2 and the He I 6678 Å line mentioned above), and the feature is much weaker than for SN 1993J at a similar epoch. Additional energy sources could also be provided by the decay of radioactive isotopes other than ^{56}Co. In the preferred steady-state NLTE model, the fractional bolometric luminosity deposited by the ^{57}Co decay is ~10 percent at 700 days and increasing. A higher mass of ^{57}Co than assumed in the preferred steady-state NLTE model would help explain the observed evolution and can not be excluded. A thermal echo from heated CSM dust could possibly power the MIR pseudo-bolometric lightcurve, but can not explain the behaviour of the optical pseudo-bolometric lightcurve. Another possibility is that the observed flux does not solely originates from the SN. A significant contribution by coincident stellar-like sources seems to be ruled out by the 678 day spectrum, however, which is clearly line dominated and have a minimum flux level close to zero. In summary we find observational and theoretical evidence that the contribution from positrons emitted in the ^{56}Co decay may not dominate the observed >600 days luminosity. A substantial contribution from time-dependent effects is likely, whereas contributions from CSM interaction and other radioactive isotopes can not be excluded. A substantial contribution from coincident sources seems to be ruled out by the 678 days spectrum, whereas a contribution from a thermal echo to the MIR luminosity can not be excluded.

5.2. Dust, molecules and the MIR evolution

There is a strong increase in the fractional MIR luminosity between 100 and 250 days, during which an increase in the decline rate of the optical pseudo-bolometric lightcurve is also observed (Sect. 2.3). The increase in fractional luminosity affects both MIR bands as well as the K band (Fig. 6). This behaviour is reminiscent of dust formation in the ejecta, where the dust would absorb the still quite hot radiation from the SN and re-emit it at a much lower temperature, and has previously been observed in SN 1987A (Suntzeff & Bouchet 1990). There is, however, an excess in the S_2 band, as compared to blackbody fits, developing already during the first hundred days (E14a). The S_2 band overlaps with both the CO fundamental band and the SiO first overtone band, so in this band molecule emission provides an alternative or complementary explanation. We detect a modest amount of CO first overtone emission at 206 days, and possibly at 89 days (Sect. 3.3), which implies at least some contribution from CO fundamental band emission to the S_2 flux. The contribution from CO first overtone emission to the K-band flux at these epochs is negligible though.

Our treatment of dust in the steady-state NLTE modelling (Sect. 4.2.4, Appendix C.7) is simplified and assumes a grey opacity in the core, turned on at 200 days. The absorbed luminosity is re-emitted as blackbody emission with a temperature determined from fits to the K and S_1 bands. The preferred model (12F), which has $\tau_{\rm dust}$=0.44, well reproduces both the drop in the optical pseudo-bolometric lightcurve and the increase in the fractional K and S_1 luminosities. This shows, most importantly, that the absorbed and emitted luminosities are in good agreement, and suggests a scenario where the emission arise from nearby, newly formed dust, presumably in the ejecta. Further support for a local origin of the emission is gained from spectra. In Fig. 25 we show the observed NIR spectrum at ~200 days, as compared to NIR spectra for the preferred model and model 12E (without dust) at 200 days, as well as the dust emission component for the preferred model. The observed flux at the absorption minimum of the He I 20581 Å line is a factor of ~2 below the model dust emission level[3], which suggests this emission to originate from $\lesssim$10000 km s^{-1}, and disfavours a thermal echo from heated CSM dust. Helou et al. (2013) showed that a thermal echo could explain the early (<100 days) MIR evolution, but were unable to reproduce the late evolution. Regardless of the location of the dust, the behaviour of the K and S_1 lightcurves is hard to explain without dust emission. The contribution from CO overtone emission to the K-band flux is negligible (Sect. 3.3), and at 250 days the discrepancy between observations and models without dust is ~1 and ~3 mag in the K and S_1 bands, respectively. Furthermore, the spectral comparison in Fig. 25 shows that the excess is mainly affecting the continuum and extends down to ~15000 Å at ~200 days. The small blue-shifts in the [O I] 6300,6364 Å and Mg I] 4571 Å lines at 415 days (Sect. 3.5) and the lack of a physical model for the temperature evolution are caveats though. A MIR excess developing between 100 and 250 days is also observed for SN 1993J (Sect. 2.3). The cause of this excess was suggested by Matthews et al. (2002) to be dust, but the absence of an increase in the optical pseudo-bolometric decline rate indicates that, if this emission is due to dust, it would rather arise from heated CSM dust. Except for SNe 2011dh and 1993J, we have found no reports of dust emission in Type IIb or stripped envelope SNe in the literature.

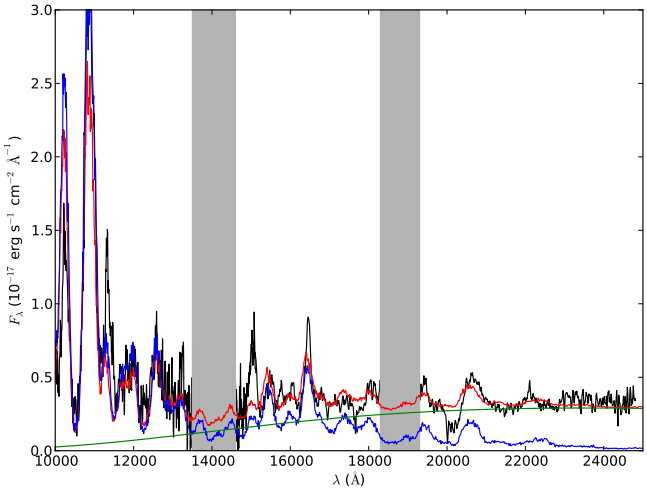

Fig. 25. Observed zJ and HK spectra at 198 and 206 days (black) compared to NIR spectra for the preferred model (12F; red) and model 12E (blue), which differs only in that $\tau_{\rm dust}$=0. The observed spectra were flux calibrated with the interpolated observed J, H and K magnitudes at 200 days and we also show the dust emission component for the preferred model (green).

Our treatment of molecules in the NLTE modelling (Sect. 4.2.4, Appendix C.5) only includes two extremes, no emission or complete dominance of the cooling in the O/C and O/Si/S zones by CO and SiO emission. This has some support in that molecules are efficient coolers and tend to dominate the cooling once formed, but is nevertheless simplified. Some amount of CO cooling in the O/C zone is implied by the CO first overtone emission detected at 206 days, and possibly at 89 days. This conclusion is supported by the observed excess in the S_2 band (Sect. 4.2.4). The dust contribution is found insufficient to reproduce the S_2 magnitudes, and these are 0.5-1.0 mag too bright as compared to the preferred model (which has no molecule cooling). If this excess is caused by molecule emission it is likely to be dominated by the CO fundamental band (Appendix C.6). Compared to models with complete molecule cooling, the CO first overtone emission is ~3.5 and ~2.5 mag too faint at 89 and 206 days, respectively, and the S_2 magnitudes are ~2 and 0.5-1.0 mag too faint at 85 and >251 days, respectively. This suggests a small amount of CO cooling in O/C zone at ~100 days, increasing to an intermediate amount at $\gtrsim$250 days. The observed CO first overtone and S_2 fluxes give an upper limit on the fundamental to first overtone band ratio. This can be improved by subtracting a model for the underlying emission, and assuming the excess to be dominated by CO fundamental band emission, this gives an estimate of the fundamental to first overtone band ratio. Using the preferred model for the underlying emission, keeping in mind that the S_2 magnitudes have to be interpolated between 85 and 251 days, we get upper limits of 6.8 and 16 and estimates of 4.5 and 7.7 at 89 and 206 days, respectively. These values are significantly larger than in the models (~1 and ~2, respectively), which assume the same fundamental to first overtone band ratio as was observed in SN 1987A. This assumption is far from obvious, as the conditions could be quite different in a Type IIb SN, and a higher value would naively suggest a lower temperature for the CO. Contributions to the S_2 excess from other processes, e.g. emission from heated CSM

[3] Note that the model dust emission has not been subject to radiative transfer (Appendix C.7), so the depth of the model He I 20581 Å absorption corresponds to that expected for a thermal echo.

dust, can not be excluded, however, and detailed modelling of the molecule emission is needed to settle this issue.

Further constraints on the amount of molecule cooling is gained from thermal lines originating in the O/C an O/Si/S zones, which will disappear if the molecule cooling is complete. The evolution in the I and z bands, which are sensitive to such lines, seems to exclude models with complete molecule cooling at $\lesssim$250 days (Sect 4.2.4). The likely presence of the C I 8727 Å line (Sect. 3.2), originating from the O/C zone (J14), seems to exclude complete CO cooling in the O/C zone also at late times. Finally, the remarkable similarity between the [O I] 6300 Å and Mg I] 4571 Å line profiles, suggests the contributions to the [O I] 6300 Å flux from the O/C and O/Si/S zones to be modest (Sect. 3.4), in turn suggesting a considerable amount of molecule cooling. Although the constraints are not conclusive, they are not necessarily inconsistent, and at least in the O/C zone, we find a small of amount of molecule (CO) cooling at ~100 days, increasing to an intermediate amount at $\gtrsim$250 days, quite likely. CO emission has been reported for the Type Ic SNe 2002ew (Gerardy et al. 2002) and 2007gr (Hunter et al. 2009), but for Type Ib and IIb SNe we have found no reports of CO emission in the literature. There is a feature near 23000 Å however, in the NIR spectra of SN 1993J (Matthews et al. 2002), that could be interpreted as a modest amount of CO first overtone emission.

5.3. The nature of the progenitor star

In M11, E14a, J14 and this paper we have investigated the nature of the progenitor star for SN 2011dh using a number of different and, at least partially, independent methods. Further modelling of our data have been presented by B12. In M11 we analyse direct observations of the putative progenitor by comparison of the observed magnitudes to predictions from stellar atmosphere and evolutionary models. The best match is found to be a yellow supergiant with an initial mass of 13±3 $M_\odot$ and a radius of ~270 $R_\odot$. In E14a we present observations of the disappearance of this star, confirming that it was the progenitor of SN 2011dh. This conclusion is complicated by the possible presence of dust in the SN ejecta with $\tau_{\rm dust}$ = 0.44 (Sect 5.2). If this dust resides in optically thick clumps there is a fair chance that the progenitor location is hidden behind such a clump. In this paper we present hydrodynamical modelling, which shows that a star with a helium core mass of $3.1^{+0.7}_{-0.4}$ $M_\odot$, exploded with an energy of $0.50^{+0.42}_{-0.22}\times10^{51}$ erg and ejecting $0.075^{+0.028}_{-0.020}$ $M_\odot$ of ^{56}Ni mixed out to high velocities, gives the best fit to the observed <400 days bolometric lightcurve and the photospheric velocity evolution. The use of a model grid allows us to determine the errors in the SN and progenitor parameters arising from the errors in the observed quantities and to constrain the degeneracy of the solution. Given this we find an upper limit on the initial mass of $\lesssim$15 $M_\odot$. B12 presented hydrodynamical modelling, which shows that a low-mass (~0.1 $M_\odot$) and extended (200-300 $R_\odot$) hydrogen-rich envelope seems to be required to reproduce the observed g-band lightcurve during the first 3 days. In E14a we estimate a hydrogen mass of 0.01-0.04 $M_\odot$ using a Monte-Carlo atmosphere code. This hydrogen mass is consistent with the B12 ejecta model, and we also find the interface between the helium core and the hydrogen envelope to be located at a velocity consistent with this model. In J14 and this paper we present steady-state NLTE modelling, which shows that a star with an initial mass of 12 $M_\odot$ well reproduces the observed 100-500 days spectral evolution and pseudo-bolometric and photometric lightcurves. Particular attention is paid to the [O I] 6300,6364 Å line, which is very sensitive to the initial mass of the star. To reproduce the flux in this line an initial mass of <17 $M_\odot$ seems to be required.

Overall the results obtained with the different methods are consistent and, even given the caveats of each individual method, it is likely that the progenitor star was of moderate initial mass ($\lesssim$15 $M_\odot$), and had a low-mass extended hydrogen rich envelope, most of which must have been lost, either through stellar winds or interaction with a binary companion. The moderate initial mass suggests that interaction with a binary companion is needed, as stellar winds of stars in this mass range are not strong enough to expel the hydrogen envelope before core-collapse. As we show in J14 and in this paper, using steady-state NLTE modelling of nebular spectra and hydrodynamical modelling of the bolometric lightcurves, SNe 2008ax and 1993J are likely to be of similar initial mass and have similar explosion energy as SN 2011dh, although the mass of the ^{56}Ni may differ significantly depending on the adopted distance and extinction. In particular, the upper bound on the initial mass for all three SNe is found to be $\lesssim$15 $M_\odot$, again suggesting that interaction with a binary companion have taken place. In the case of SN 1993J, this conclusion is supported by direct observations of the binary companion (Maund et al. 2004; Fox et al. 2014). Observations, that could detect or set useful constraints on the presence of a companion star for SN 2011dh, are scheduled for Cycle 21 at HST. Clearly there is growing evidence that the main production channel for Type IIb SNe are stars whose hydrogen envelope has been stripped by interaction with a binary companion. Modelling of the nebular spectra and hydrodynamical modelling of the bolometric lightcurves for a larger sample of Type IIb SNe, could provide further evidence for this hypothesis.

6. Conclusions

We present two years of optical and NIR photometric and spectroscopic observations for the Type IIb SN 2011dh. Together with SWIFT and Spitzer observations the data cover the UV to MIR wavelength range, although the photometric coverage ends at ~100 days in UV and at ~400 days in NIR, and the spectral coverage ends at ~200 days in NIR and at ~450 days in the optical. Particular attention is paid to the bolometric and photometric lightcurves, where we use steady-state NLTE modelling and hydrodynamical modelling to put constraints on the SN and progenitor parameters. We also provide a spectral analysis, mainly related to the line profiles, complementary to the steady-state NLTE modelling of nebular spectra presented in J14.

We analyse the <100 days pseudo-bolometric lightcurve of SN 2011dh, using a grid of hydrodynamical SN models based on bare helium core models (E14b). This method allows us to determine the errors in the model parameters arising from the uncertainties in the observed quantities, and the degeneracy of the solution. To extend the temporal coverage of the model grid to 400 days, we apply a bolometric correction determined with steady-state NLTE modelling. The results obtained using the <100 days and <400 days pseudo-bolometric lightcurves are similar, and using the latter we find a helium core mass of $3.1^{+0.7}_{-0.4}$ $M_\odot$, an explosion energy of $0.50^{+0.42}_{-0.22}\times10^{51}$ erg, and a mass of ^{56}Ni of $0.075^{+0.028}_{-0.020}$ $M_\odot$, in good agreement with the results obtained in B12. The <100 days pseudo-bolometric lightcurves of SNe 2008ax and 1993J are also analysed, and the best fit values for the helium core mass and explosion energy are similar to those of SN 2011dh. However, as a consequence of the bare

helium core approximation, the helium core mass and explosion energy for SN 1993J, which likely had the most massive hydrogen envelope, might be underestimated. We find an upper limit on the helium core mass for all three SNe of $\lesssim$4 $M_\odot$, corresponding to an upper limit on the initial mass of $\lesssim$15 $M_\odot$. Strong mixing of the ^{56}Ni is required for all three SNe to fit the rise to peak luminosity.

We analyse the 100-500 days pseudo-bolometric and photometric lightcurves of SN 2011dh, using the restricted set of steady-state NLTE models presented in J14. To extend the temporal coverage of these models, we construct <100 days bolometric lightcurves using HYDE (Appendix D) in homologous mode. The preferred 12 $M_\odot$ (initial mass) model, presented in J14, refined in this work with respect to the dust, and chosen to give the best agreement with both spectra and lightcurves, shows an overall agreement with the observed photometric and pseudo-bolometric lightcurves. The optical to MIR pseudo-bolometric lightcurve seems to exclude 17 $M_\odot$ and medium mixing models, and the optical pseudo-bolometric lightcurve and the fractional J luminosity at 300-400 days suggest local positron trapping. The simultaneous increase in the optical pseudo-bolometric decline rate and the fractional K and S_1 luminosities between 100 and 250 days is reproduced by the preferred model, which has a modest dust opacity in the core ($\tau_{\rm dust}$ = 0.44), turned on at 200 days. A local origin of the excess emission is supported by the depth of the He I 20581 Å absorption. We find the dust contribution insufficient to reproduce the S_2 magnitudes and, assuming this additional excess to be dominated by CO fundamental band emission, an intermediate amount of CO cooling in O/C zone is likely. This is consistent with the detected CO first overtone emission, although the fundamental to first overtone band ratios needs to be significantly higher than observed in SN 1987A.

The >500 days lightcurves can not be analysed with the steady-state NLTE code, as in this phase a steady-state assumption is no longer valid. In the preferred steady-state NLTE model the positron contribution dominates the ^{56}Co energy deposition after ~450 days. However, there is both observational and theoretical evidence that the >500 days lightcurves are dominated by additional energy sources. The optical and MIR decline rates start to decrease already at ~400 days, and at >600 days they are significantly lower than the decay rate of ^{56}Co, becoming almost flat in the MIR towards ~1000 days. In addition, the observed optical and MIR luminosities at >600 days, seem to be too high to be powered by the radioactive energy deposition alone. This is particularly true if the positrons are locally trapped, as suggested by the 300-400 days lightcurves. Modelling with a time-dependent NLTE code (Kozma & Fransson 1992, 1998a,b) shows that time-dependent effects become important at ~600 days, and after ~800 days they provide a dominant and increasing contribution to the optical luminosity. We find that substantial contributions from CSM interaction and other radioactive isotopes are less likely, but can not be excluded. A substantial contribution from coincident sources seems to be ruled out, whereas a contribution from a thermal echo to the MIR luminosity can not be excluded.

The line profiles of the important lines are analysed and we estimate progressively smaller sizes, ranging from ~3000 to ~1500 km s^{-1}, for the line emitting regions of oxygen, magnesium, [Ca II] 7291,7323 Å and iron, in all compared cases smaller than those of SNe 1993J and 2008ax. Given the findings in J14, these regions would correspond to the oxygen, O/Ne/Mg, Si/S and Fe/Co/He nuclear burning zones, and suggest incomplete mixing of the core material. The profiles of the [O I] 6300 Å and Mg I] 4571 Å lines show a remarkable similarity, suggesting that these lines arise from the O/Ne/Mg zone. We use repetitions of small scale fluctuations in the [O I] 6300 Å and [O I] 6364 Å lines to find a line ratio close to 3, consistent with optically thin emission, from 200 days and onwards. Applying the method of Chugai (1994) to these small scale fluctuations, we find an upper limit on the filling factor of the [O I] 6300 Å and Mg I] 4571 Å line emitting material of ~0.07, and a lower limit on the number of clumps of ~900.

This paper concludes our observational and modelling work on SN 2011dh presented in M11, E14a and J14. Further modelling of our data have been presented by B12. We have applied stellar evolutionary progenitor analysis, hydrodynamical modelling, SN atmosphere modelling and steady-state NLTE modelling to our extensive set of observational data. Although a number of issues remains unsolved, the main characteristics of the SN and its progenitor star found by the different methods are consistent. The progenitor star appears to have been of moderate ($\lesssim$15 $M_\odot$) initial mass, and the 3-4 $M_\odot$ helium core surrounded by a low-mass (~0.1 $M_\odot$) and extended (200-300 $R_\odot$) hydrogen envelope. In particular, we have found the initial masses of SNe 2011dh, 1993J and 2008ax to be $\lesssim$15 $M_\odot$, from both hydrodynamical modelling of the early bolometric evolution and steady-state NLTE modelling of the late spectral evolution. This limit is also supported by stellar evolutionary progenitor analysis for SNe 2011dh and 1993J (Maund et al. 2004, 2011). Given that the mass-loss rates for stars in this mass range are probably not strong enough to expel the hydrogen envelope before core-collapse, a binary origin for these SNe is strongly suggested.

7. Acknowledgements

This work is based on observations obtained with the Nordic Optical Telescope, operated by the Nordic Optical Telescope Scientific Association at the Observatorio del Roque de los Muchachos, La Palma, Spain, of the Instituto de Astrofisica de Canarias; the German-Spanish Astronomical Center, Calar Alto, jointly operated by the Max-Planck-Institut für Astronomie Heidelberg and the Instituto de Astrofísica de Andalucía (CSIC); the United Kingdom Infrared Telescope, operated by the Joint Astronomy Centre on behalf of the Science and Technology Facilities Council of the U.K.; the William Herschel Telescope and its service programme (proposals SW2011b21 and SW2012a02), operated on the island of La Palma by the Isaac Newton Group in the Spanish Observatorio del Roque de los Muchachos of the Instituto de Astrofisica de Canarias; the Copernico 1.82m Telescope and Schmidt 67/92 Telescope operated by INAF - Osservatorio Astronomico di Padova at Asiago, Italy; by the 3.6m Italian Telescopio Nazionale Galileo operated by the Fundación Galileo Galilei - INAF on the island of La Palma; the Liverpool Telescope, operated on the island of La Palma by Liverpool John Moores University in the Spanish Observatorio del Roque de los Muchachos of the Instituto de Astrofisica de Canarias with financial support from the UK Science and Technology Facilities Council; the AlbaNova telescope operated by the Department of Astronomy at Stockholm University and funded by a grant from the Knut and Alice Wallenberg Foundation. We acknowledge the exceptional support we got from the NOT staff throughout this campaign, we thank the Calar Alto Observatory for allocation of director's discretionary time and we thank Philip Dufton, Paul Dunstall, Darryl Wright and Lindsay Magill for assistance with the WHT observations.

The Oskar Klein Centre is funded by the Swedish Research Council. J.S. acknowledge support by the Swedish Research Council. S.J.S. thanks European Research Council under the European Union's Seventh Framework Programme (FP7/2007-2013)/ERC Grant agreement n° [291222] and STFC. A.P., L.T. and S.B. are partially supported by the PRIN-INAF 2011 with the project "Transient Universe: from ESO Large to PESSTO". M.F. acknowledges support by the European Union FP7 programme through ERC grant number 320360. N.E.R. acknowledges the support from the European Union Seventh Framework Programme (FP7/2007-2013) under grant agreement n° 267251 "Astronomy Fellowships in Italy" (AstroFIt). R.K. acknowledges observing time at the LT, NOT, TNG, and WHT via programme CCI-04. M.M.K. acknowledges generous support from the Hubble Fellowship and Carnegie-Princeton Fellowship.

We thank Melina Bersten for providing the post-explosion density profile for the He4R270 model (B12), for inspiration and a great contribution to the understanding of SN 2011dh. We thank Peter Meikle and Dan Milisavljevic for providing spectra on SN 1993J and SN 2008ax, respectively.

Appendix A: Data reductions and calibration

The reductions and calibration procedures used for the late time data are the same as described in E14a. Here we discuss data reduction and calibration issues specifically related to the >100 days data.

Appendix A.1: Template subtraction - 100-500 days optical and NIR observations

Comparison of photometry on the original images and on template subtracted images, shows that the background contamination is negligible before ~300 days, after which we have used photometry on template subtracted images. The optical templates were constructed by point spread function (PSF) subtraction of the SN from observations acquired after 600 days, and the NIR templates by PSF subtraction of the SN from the 339 days WHT observation, which is of excellent quality. For the last 380 days WHT observation we used PSF photometry.

Appendix A.2: S-corrections - 100-500 days optical and NIR observations

The accuracy of the late time photometry depends critically on the accuracy of the S-corrections. Figure A.1 shows the difference between colour and S-corrections for the Johnson-Cousins (JC) and 2 Micron All Sky Survey (2MASS) systems for most telescope/instrument combinations used. It is clear from this figure that S-corrections are necessary if good precision in the photometry is needed. For some telescope/instrument/band combinations, as for the CA-2.2m/CAFOS and NOT/ALFOSC *I* band and the CA-3.5m/O2000 *J* band, the differences become as large as 0.3-0.5 mag. In particular, the difference between the NOT/ALFOSC and CA-2.2m/CAFOS *I* band observations are ~0.8 mag at ~250 days, mainly due to the strong [Ca II] 7291,7323 Å and Ca II 8498,8542,8662 Å lines. As the spectral NIR coverage ends at ~200 days, we have assumed that the 2MASS S-corrections do not change during the 200-400 days period. This adds uncertainty to the 2MASS photometry after ~200 days, but as the 2MASS S-corrections, except for the CA-3.5m/O2000 *J* band, are generally small and evolve slowly, the errors arising from this approximation are probably

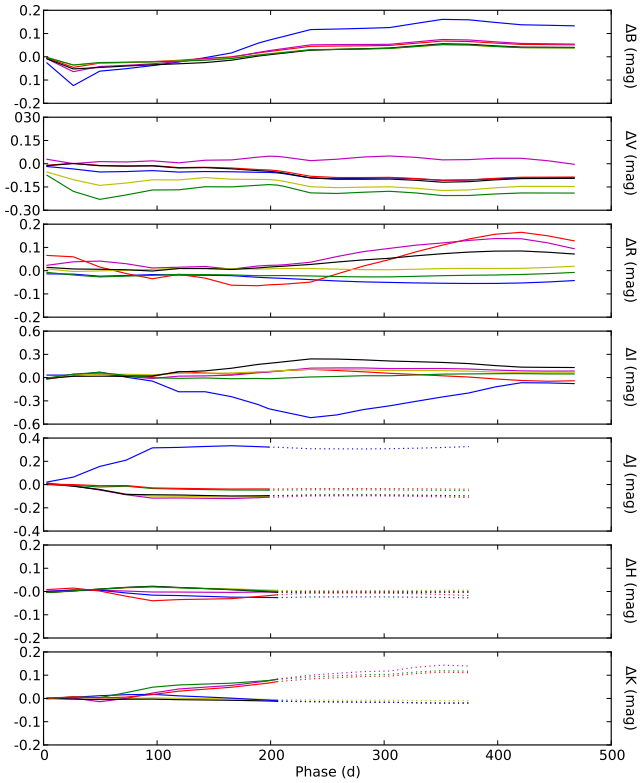

Fig. A.1. Difference between JC *BVRI* colour and S-corrections for NOT/ALFOSC (black), LT/RATCam (red), CA-2.2m/CAFOS (blue), TNG/LRS (green), AS-1.82m/AFOSC (yellow) and AS-Schmidt (magenta), and difference between 2MASS *JHK* colour and S-corrections for NOT/NOTCAM (black), TCS/CAIN (red), CA-3.5m/O2000 (blue), TNG/NICS (green), WHT/LIRIS (yellow) and UKIRT/WFCAM (magenta). Results based on extrapolated 2MASS S-corrections are shown as dotted lines.

modest. The accuracy of the S-corrections can be estimated by comparing S-corrected photometry obtained with different telescope/instrument combinations. The late time JC and Sloan Digital Sky Survey (SDSS) photometry were mainly obtained with the NOT, but comparisons between S-corrected NOT/ALFOSC, LT/RATCam and CA-2.2m/CAFOS JC and SDSS observations at ~300 days, show differences at the 5 percent level, suggesting that the precision from the <100 days period is maintained (E14a). The late time 2MASS photometry was obtained with a number of different telescopes, and although the sampling is sparse, the shape of the lightcurves suggests that the errors in the S-corrections are modest. Additional filter response functions for AT and UKIRT have been constructed as outlined in E14a.

Appendix A.2.1: Post 600 days optical observations

The results for the post 600 days observations have been adopted from the pre-explosion difference imaging presented in E14a, assuming that the remaining flux at the position of the progenitor originates solely from the SN. The observations were S-corrected using the 678 day spectrum of SN 2011dh presented by Shivvers et al. (2013). Comparing to results from PSF photometry, where we iteratively fitted the PSF subtracted background, we find differences of $\lesssim$0.1 mag. Given that the pre-explosion magnitudes (which were measured with PSF photometry) are correctly measured, the difference based magnitudes are likely

to have less uncertainty. On the other hand, the PSF photometry does not depend on the uncertainty in the pre-explosion magnitudes. The good agreement found using these two, partly independent methods gives confidence in the results. Further confidence is gained by comparing the S-corrected NOT and HST (Van Dyk et al. 2013) V-band observations, for which we find a difference of $\lesssim$0.2 mag. We are assuming that the flux at the position of the progenitor originates solely from the SN, which should be kept in mind. There is support for this assumption, though, from the depth of absorption features and the line dominated nature of the 678 days spectrum presented by Shivvers et al. (2013).

Appendix A.2.2: Spitzer Telescope observations

For the >100 days photometry we used a small aperture with a 3 pixel radius, and a correction to the standard aperture given in the IRAC Instrument Handbook determined from the images. All images were template subtracted using archival images as described in (E14a). After 100 days, background contamination becomes important, and template subtraction is necessary to obtain precision in the photometry. The <700 days photometry previously published by Helou et al. (2013) agrees very well with our photometry, the differences being mostly $\lesssim$5 percent.

Appendix B: Line measurements

Appendix B.1: Line emitting regions

To estimate the sizes of the line emitting regions, we fit the line profile of a spherically symmetric region of constant line emissivity, optically thin in the line (no line scattering contribution) and with a constant absorptive continuum opacity, to the observed, continuum subtracted (Sect. B.3) line profile. The fitting is done by an automated least-square based algorithm. The absorptive continuum opacity is included to reproduce the blueshifts observed in some line profiles. This method gives a rough estimate of the size of the region responsible for the bulk of the line emission, and is not applied if scattering appears to contribute significantly to the line profile. Some lines arise as a blend of more than one line, which has to be taken into account. The [O I] 6300 Å flux was calculated by iterative subtraction of the [O I] 6364 Å flux, from the left to the right, using $F_{6300}(\lambda) = F_{6300,6364}(\lambda) - F_{6300}(\lambda - \Delta\lambda)/R$, where $\Delta\lambda$ is the wavelength separation between the [O I] 6300 Å and 6364 Å lines and R the [O I] 6300,6364 Å line ratio. This ratio was assumed to be 3, as is supported by the preferred J14 steady-state NLTE model and estimates based on small scale fluctuations in the line profiles (Sect. 3.6). For all other blended lines, we make a simultaneous fit with the line ratios as free parameters, assuming a common size of the line emitting regions.

Appendix B.2: Line asymmetries

To estimate the asymmetry of a line we calculate the first wavelength moment of the flux (center of flux) for the continuum subtracted (Sect. B.3) line profile. The rest wavelength is assumed to be 6316 Å and 7304 Å for the [O I] 6300,6364 Å and [Ca II] 7291,7323 Å lines, respectively, as is appropriate for optically thin emission if we assume the upper levels of the [Ca II] 7291,7323 Å line to be populated as in local thermal equilibrium (LTE). Optically thin emission for these lines is supported by the preferred J14 steady-state NLTE model, the absence of absorption features in the observed spectra and the [O I] 6300,6364 Å line ratio (Sect. 3.6). The rest wavelength is assumed to be 5896 Å and 8662 Å for the Na I 5890,5896 Å and Ca II 8498,8542,8662 Å lines, respectively, as is appropriate for optically thick emission, where emission from the blue lines will eventually scatter in the reddest line. Optically thick emission for the Na I 5896 Å line is supported by the preferred J14 steady-state NLTE model and the observed P-Cygni profile. For the Ca II 8662 Å line this assumption is more doubtful.

Appendix B.3: Continuum subtraction

Before fitting the line emitting region or calculating the center of flux, the (quasi) continuum is subtracted. The continuum level is determined by a linear interpolation between the minimum flux levels on the blue and red sides of the smoothed line profile. The search region is set to ±6000 km s^{-1} for most of the lines, ±10000 km s^{-1} for the Ca II 8662 Å line and ±3000 km s^{-1} for the [Fe II] 7155 Å line.

Appendix C: NLTE model parameters.

Here we discuss the effects of the model parameters on the model lightcurves for the J14 steady-state NLTE models. We also describe the treatment of molecule cooling and dust, whereas the other model parameters are described in detail in J14. To analyse the lightcurves, we make use of a split into a bolometric lightcurve and a bolometric correction (BC). In terms of these quantities, the photometric and pseudo-bolometric magnitudes are given by M=M_{Bol}-BC (where pseudo-bolometric magnitude refer to the pseudo-bolometric luminosity on the bolometric magnitude system). This split is most useful for the analysis of the model lightcurves, as the bolometric lightcurve depends only on the deposition of radioactive decay energy, whereas the BCs depend on how this energy is processed. There is a subtlety here though, as even in steady-state the bolometric luminosity does not equal the energy deposition, because some energy is lost due to scattering in the ejecta. This difference is small (<0.05 mag) and will be ignored in the subsequent discussion. As the bolometric lightcurves depend only on the energy deposition, they are independent of molecule cooling and dust, which only affects the processing of the deposited energy. As discussed in Sects. C.3 and C.4, within the parameter space covered by the J14 models, the bolometric lightcurves are only weakly dependent on the density contrast and the positron trapping. Therefore, the bolometric lightcurves depend significantly only on the initial mass and the macroscopic mixing, whereas the BCs may depend on all model parameters. Figure C.1 shows the 100-500 days bolometric lightcurves for the J14 model families differing in initial mass and macroscopic mixing. The bolometric lightcurves have been normalized with the decay chain luminosity of the mass of ^{56}Ni. This is convenient as the bolometric lighcurves then become independent of this parameter. The mass of ^{56}Ni is not varied in the J14 models, as it mainly affects the bolometric lightcurve and, to first order, corresponds to a scaling of the pseudo-bolometric and photometric lightcurves. Figures C.2 and C.3 shows the pseudo-bolometric and photometric BCs for the J14 models. The optical to MIR BCs show small differences (<±0.1 mag) during the 100-400 days period, but these subsequently increase towards ±0.25 mag at 500 days. At 100 days the optical to MIR BC is >−0.15 mag, and it is likely that this holds at <100 days as well. The optical BCs, on the other hand, show larger differences, mainly because molecule cooling

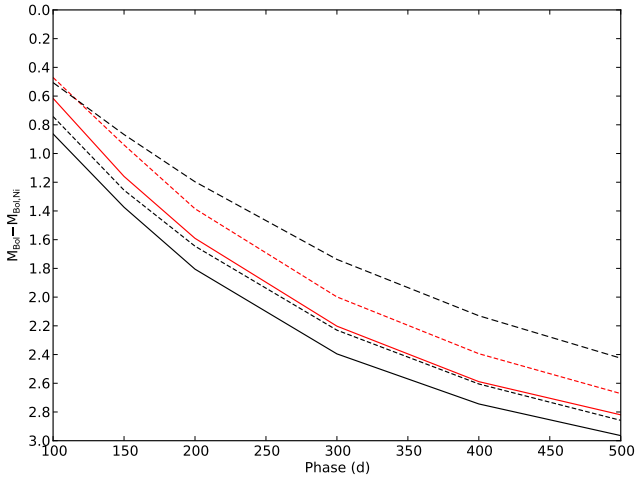

Fig. C.1. 100-500 days bolometric lightcurves for the J14 model normalized to the radioactive decay chain luminosity of 0.075 $M_\odot$ of ^{56}Ni. The model families differing in initial mass and macroscopic mixing are displayed as follows: 12 $M_\odot$ (solid lines), 13 $M_\odot$ (short dashed lines), 17 $M_\odot$ (long dashed lines), medium mixing (red), strong mixing (black).

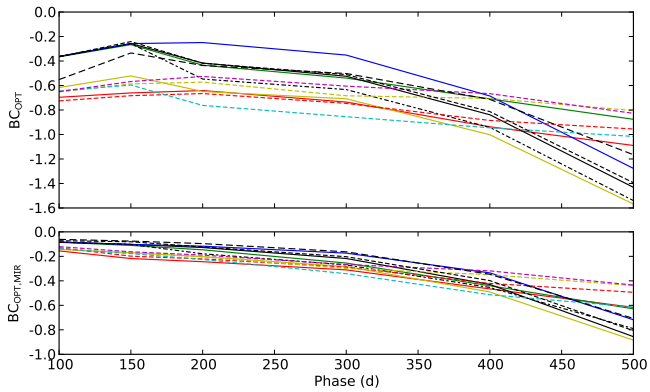

Fig. C.2. 100-500 days optical (upper panel) and optical to MIR (lower panel) BCs for the J14 models. The models are displayed as follows; 12A (red solid line), 12B (green solid line), 12C (black solid line), 12D (yellow solid line), 12E (blue solid line), 12F (black dashed-dotted line), 13A (red short-dashed line), 13C (yellow short-dashed line), 13D (cyan short-dashed line), 13E (magenta short-dashed line), 13G (black short-dashed line), 17A (black long-dashed line).

and dust affects the distribution of the flux between the optical and the MIR.

Appendix C.1: Effect of initial mass

The initial mass may affect both the energy deposition (bolometric lightcurve) and the way this energy is processed (BC). Comparing the bolometric lightcurves and the pseudo-bolometric BCs for models 12C, 13G and 17A, which differ only in the initial mass, we find that the average difference in the bolometric lightcurve is 0.62 mag, whereas the average differences in the optical to MIR and optical BCs are 0.08 and 0.11 mag, respectively. There is an increasing spread in the optical to MIR and optical BCs developing with time though, and at 500 days the differences are 0.18 and 0.31 mag, respectively.

The average difference in the photometric BCs is 0.23 mag, but varies quite a lot with band and phase and the maximum difference is 1.01 mag. As discussed in J14, the [O I] 6300,6364 Å line is particularly sensitive to the initial mass. The fraction of the *R*-band flux originating from [O I] 6300,6364 Å line is <0.38, <0.49 and <0.67 in model 12C, 13G and 17A, respectively. The difference in $BC_{6300,6364}$ between model 12C and 17A is ~1 mag, and the corresponding difference in BC_R is <0.41 mag. There is also a degeneracy with the effects of positron trapping and molecule cooling on BC_R (Appendices C.4 and C.6), which are of similar magnitude. The difference in [O I] 6300,6364 Å flux between model 12C and 17A is ~1.5 mag, and the corresponding difference in the *R*-band magnitudes ~1 mag. This difference is larger than the difference in the bolometric lightcurve and, provided the mass of ^{56}Ni is known, *R*-band magnitudes might prove useful to constrain the initial mass.

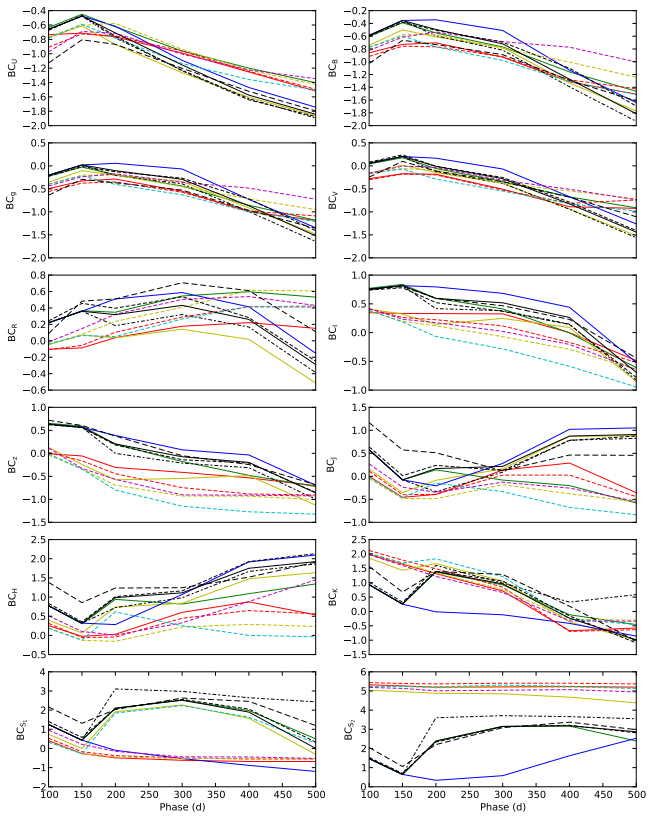

Fig. C.3. 100-500 days photometric BCs for the J14 models. The models are displayed as in Fig. C.2.

Appendix C.2: Effect of macroscopic mixing

The macroscopic mixing may affect both the energy deposition (bolometric lightcurve) and the way this energy is processed (BC). Comparing the bolometric lightcurves and the pseudo-bolometric BCs for models 13A and 13C, which differ only in the macroscopic mixing, we find that the average difference in the bolometric lightcurve is 0.29 mag, whereas the average differences in the optical to MIR and optical BCs are 0.04 and 0.12 mag, respectively.

The average difference in the photometric BCs is 0.14 mag, but varies quite a lot with band and phase and the maximum difference is 0.42 mag. There is a general trend in the BCs corresponding to bluer emission for model 13C (strong mixing). This is a bit surprising, as the lower energy deposition per mass in

strongly mixed models naively would result in lower temperatures and redder emission. However, although the temperature decrease in the core zones, the increased energy deposition in the helium envelope, which has a higher temperature and also bluer non-thermal emission, seems to counterweight this effect, and the end result is bluer emission.

Appendix C.3: Effect of density contrast

The density contrast may affect both the energy deposition (bolometric lightcurve) and the way this energy is processed (BC). However, in the J14 models, the energy deposition is only weakly dependent of the contrast factor, as the optical depths to γ-rays and non-locally trapped positrons for individual Fe/Co/He clumps are $\ll$1, when these are contributing substantially to the energy deposition. Comparing models 13C and 13E, that differ only in the density contrast, the difference in energy deposition is <0.03 mag. Furthermore, there are reasons to suspect that the differences in the BCs are small as well, as the fraction of the deposited energy going into heating, ionization and excitation is not particularly sensitive to the density (Kozma & Fransson 1992). Comparing the pseudo-bolometric BCs of models 13C and 13E, these are indeed very similar, but show a small (<0.08 mag) difference.

As discussed in J14 the Mg I] 4571 Å line is sensitive to the density contrast and the fractional flux differs with ~1 mag at 300 days between model 13C and 13E. However, the fractional Mg I] 4571 Å flux in the B band is <0.09 and <0.24 for model 13C and 13E, respectively, so the difference in BC_B is only <0.24 mag. As seen in Fig. C.3, there is a strong difference in BC_H developing at >300 days, and at 500 days the difference is ~1.2 mag. Inspection of the models reveals that this difference is caused by the [Si I] 16450 Å line, which becomes very strong in high density contrast models.

Appendix C.4: Effect of positron trapping

The positron trapping may affect both the energy deposition (bolometric lightcurve) and the way this energy is processed (BC). However, in the J14 models, the energy deposition is (in most cases) independent of the positron trapping, as the optical depths to non-locally trapped positrons are (in most cases) $\gg$1. Exceptions are the strongly mixed models with non-locally trapped positrons, where a small (<0.05 mag) difference develops at late times. Positron trapping only affects the BCs when the contribution from positrons to the energy deposition becomes significant, and before this models with locally or non-locally trapped positrons are indistinguishable. Comparing models 12C and 12B, which differ only in the positron trapping, the pseudo-bolometric BCs for model 12C (local trapping) get increasingly smaller after ~300 days, when the contribution from positrons to the energy deposition starts to become significant. The reason for this is that locally trapped positrons deposit all their energy in the Fe/Co/He zone. This zone has a lower temperature than other zones, because of efficient cooling from the large number of iron lines, and the emission arising from this zone is redder. At 500 days the differences in the optical to MIR and optical BCs are 0.24 and 0.57 mag, respectively.

At late times, we expect the luminosity of lines originating from the Fe/Co/He zone to be boosted, and the luminosity of lines originating from other zones to be reduced, if the positrons are locally trapped. As discussed in J14, the [O I] 6300,6364 Å, [N II] 6548,6583 Å, [Fe II] 12567 Å, [Fe II] 12700-13200 Å and the [Fe II] 16440 Å lines are particularly sensitive to the positron trapping. Therefore we would expect BC_R, BC_J and BC_H to be particularly sensitive and, as seen in Fig. C.3, this is also the case. Comparing models 12C and 12B, BC_R, BC_J and BC_H start to diverge at >200 days, and at 500 days they differ with ~0.8, ~1.5 and ~0.6 mag, respectively.

Appendix C.5: Treatment of molecule cooling

Molecule cooling is included in the modelling in a simplified way, and is represented as the fraction of the (radiative and radioactive) heating emitted as molecule (CO and SiO) emission in the O/C and O/Si/S zones. This energy is then emitted as CO and SiO fundamental and first overtone band emission, represented as box line profiles between 2.25-2.45 (CO first overtone), 4.4-4.9 (CO fundamental) and 4.0-4.5 (SiO first overtone) μm. The CO first overtone band overlaps partly with the K band, and the CO fundamental and SiO first overtone bands overlap with the S_2 band, whereas the SiO fundamental band lies outside the U to S_2 wavelength range. The fundamental to first overtone band flux ratios are assumed to be the same as observed for CO in SN 1987A (Bouchet & Danziger 1993). We have used two configurations, one where the fraction of the heating emitted as molecule emission has been set to one, and one where this fraction has been set to zero.

Appendix C.6: Effect of molecule cooling

Molecule cooling only affects the way the deposited energy is processed (BC). Comparing models 12C and 12D, which only differ in the amount of molecule cooling, the optical BC for model 12D (complete cooling) are 0.1-0.3 mag smaller. The optical to MIR BCs, on the other hand, are similar. This reflects the fact that most of the molecule emission falls within the U to S_2 wavelength range and the flux is mainly redistributed within this wavelength range.

The effect of molecule cooling is strong in the S_2 band, which overlaps with the CO fundamental band and the SiO first overtone band, but less so in the K band, which overlaps partly with the CO first overtone band. CO fundamental band emission dominates the contribution to the S_2 band in all models at all times. This is because the O/Si/S to O/C zone mass ratio and the CO and SiO fundamental to overtone band ratios are all $\lesssim$1, decreasing with increasing initial mass and with time, respectively. BC_{S_2} is 2-4 mag larger for model 12D (complete cooling) as compared to model 12C whereas BC_K is less affected, being $\lesssim$1 mag larger for model 12D at early times. Molecule cooling also determines the fraction of the (radiative and radioactive) heating going into line emission in the O/C and O/Si/S zones. Therefore we expect thermally excited lines in these zones to be sensitive to the amount of molecule cooling. In particular, CO cooling affects the [O I] 6300,6364 Å and [C I] 8727 Å lines, whereas SiO cooling affects the [Ca II] 7291,7323 Å and [S I] 10820 Å lines and, at early times, the Ca II 8498,8542,8662 Å line. BC_I and BC_z differ at <400 days and are ~0.5 mag smaller at <200 days for model 12D (complete cooling). BC_R differs throughout the evolution and is ~0.3 mag smaller at <300 days for model 12D.

Appendix C.7: Treatment of dust

Dust is included in the modelling in a simplified way, and is represented as a grey absorptive opacity in the core. The absorbed luminosity is re-emitted as blackbody emission with a tempera-

ture determined from fits to the photometry. The dust emission is treated separately from the modelling, and is added by post-processing of the model spectra. All the models presented in J14 have the same optical depth and dust temperature, determined from the pseudo-bolometric optical lightcurve and fits to the H, K and S_1 photometry, as described below. In addition we have constructed two new models, 12E which differs from 12C only in the absence of dust and 12F, which differs from 12C only in the optical depth and the method to determine the temperature.

The J14 models have an optical depth of 0.25, turned on at 200 days, which approximately match the behaviour of the optical pseudo-bolometric lightcurve. The temperature is constrained to scale as for a homologously expanding surface, representing a large number of optically thick dust clouds (J14). Minimizing the sum of squares of the relative flux differences of model and observed H, K and S_1 photometry at 200, 300 and 400 days (including H only at 200 days), we find temperatures of 2000, 1097 and 668 K at 200, 300 and 400 days, respectively, given the constraint $T_{dust} < 2000$ K. The S_2 band was excluded as this band might have a contribution from molecule emission, whereas we know that the contribution from CO first overtone emission to the K band at 206 days is negligible. However, the fractional area of the emitting surface (x_{dust}), turns out to be ~20 times smaller than the fractional area needed to reproduce the optical depth, so the derived temperature is not consistent with the assumptions made.

Model 12F has an optical depth of 0.44, turned on at 200 days, which better match the behaviour of the optical pseudo-bolometric lightcurve. The constraint on the temperature evolution used for the J14 models has been abandoned, and fitting the H, K and S_1 photometry as described above, we find temperatures of 1229, 931 and 832 K at 200, 300 and 400 days respectively. This shows that, in addition to the inconsistency between the absorbing and emitting area, the scaling of temperature is not well reproduced by the J14 models. Due to the better reproduction of the optical pseudo-bolometric lightcurve, and the problems with the temperature scaling used for the J14 models, we will use model 12F, instead of model 12C, as our preferred model in this paper. Abandoning all attempts to physically explain the temperature, leaves us with black box model, parametrized with the optical depth and the temperature. This is a caveat, but also fair, as the original model with homologously expanding dust clouds, is not self-consistent.

Appendix C.8: Effect of dust

Dust only affects the way the deposited energy is processed (BC). Comparing models 12E and 12F, which only differ in the presence of dust after 200 days, the optical BC for model 12F (with dust) becomes 0.3 mag smaller at 200 days, roughly corresponding to the optical depth of the dust. The optical to MIR BCs are the same until ~300 days, and then slowly becomes smaller for model 12F (with dust), reflecting the decreasing temperature of the dust. The effect of dust (emission) is strong on BC_K and the MIR BCs which at 200 days become ~1 and ~3 mag larger, respectively, for model 12F (with dust) and then slowly evolve according to the decreasing temperature of the dust.

Appendix D: HYDE and the model grid

Here we provide a summary of HYDE and the grid of SN models constructed with this code and MESA STAR (Paxton et al. 2011). A detailed description is provided in E14b, where we also provide tests of HYDE and a detailed analysis of the behaviour of the model grid.

HYDE Is a one-dimensional Lagrangian hydrodynamical code based on the flux limited diffusion approximation, following the method described by Falk & Arnett (1977), and adopting the flux limiter given by Bersten et al. (2011). The opacity is calculated from the OPAL opacity tables (Iglesias & Rogers 1996), complemented with the low temperature opacities given by Alexander & Ferguson (1994). In addition we use an opacity floor set to 0.01 cm^2 $gram^{-1}$ in the hydrogen envelope and 0.025 cm^2 $gram^{-1}$ in the helium core, following Bersten et al. (2012, private communication), who calibrated these values by comparison to the STELLA hydrodynamical code (Blinnikov et al. 1998). The electron density, needed in the equation of state, is calculated by solving the Saha equation using the same atomic data as in Jerkstrand et al. (2011, 2012). The transfer of the gamma-rays and positrons emitted in the decay chain of ^{56}Ni is calculated with a Monte-Carlo method, using the same grey opacities, luminosities and decay times as in Jerkstrand et al. (2011, 2012).

The model grid Is based on non-rotating solar metallicity helium cores, evolved to the verge of core-collapse with MESA STAR (Paxton et al. 2011). The configuration used was the default one, and a central density limit of $10^{9.5}$ gram cm^{-3} was used as termination condition. The evolved models spans M_{He}=4.0-5.0 $M_\odot$ in 0.25 $M_\odot$ steps and M_{He}=5.0-7.0 $M_\odot$ in 0.5 $M_\odot$ steps. Below 4.0 $M_\odot$, stellar models were constructed by a scaling of the 4.0 $M_\odot$ density profile. The SN explosion was parametrized with the injected explosion energy (E), the mass of the ^{56}Ni (M_{Ni}) and the distribution of it. The mass fraction of ^{56}Ni (X_{Ni}) was assumed to be a linearly declining function of the ejecta mass (m_{ej}) becoming zero at some fraction of the total ejecta mass (Mix_{Ni}), expressed as $X_{Ni} \propto 1 - m_{ej}/(Mix_{Ni}M_{ej}), X_{Ni} \geq 0$. Note that this expression allows $Mix_{Ni} > 1$, although the interpretation then becomes less clear. The total volume of parameter space spanned is M_{He}=2.5-7.0 $M_\odot$, E=0.2-2.2×10^{51} erg, M_{Ni}=0.015-0.250 $M_\odot$ and Mix_{Ni}=0.6-1.6 using a 12×16×13×9 grid. A mass cut with zero velocity was set at 1.5 $M_\odot$, the material below assumed to form a compact remnant, although fallback of further material onto this boundary is not prohibited.

References

Alexander, D. R. & Ferguson, J. W. 1994, ApJ, 437, 879
Arcavi, I., Gal-Yam, A., Yaron, O., et al. 2011, ApJ, 742, L18
Benvenuto, O. G., Bersten, M. C., & Nomoto, K. 2013, ApJ, 762, 74
Bersten, M. C., Benvenuto, O., & Hamuy, M. 2011, ApJ, 729, 61
Bersten, M. C., Benvenuto, O. G., Nomoto, K., et al. 2012, ApJ, 757, 31
Blinnikov, S. I., Eastman, R., Bartunov, O. S., Popolitov, V. A., & Woosley, S. E. 1998, ApJ, 496, 454
Bouchet, P. & Danziger, I. J. 1993, A&A, 273, 451
Chugai, N. N. 1994, ApJ, 428, L17
Ergon, M., Sollerman, J., Fraser, M., et al. 2014a, A&A, 562, A17
Ergon, M., Sollerman, J., Jerkstrand, A., & Fransson, C. 2014b, In preparation
Falk, S. W. & Arnett, W. D. 1977, ApJS, 33, 515
Filippenko, A. V. & Sargent, W. L. W. 1989, ApJ, 345, L43
Fox, O. D., Azalee Bostroem, K., Van Dyk, S. D., et al. 2014, ArXiv e-prints
Gerardy, C. L., Fesen, R. A., Nomoto, K., et al. 2002, PASJ, 54, 905
Griga, T., Marulla, A., Grenier, A., et al. 2011, Central Bureau Electronic Telegrams, 2736, 1
Helou, G., Kasliwal, M. M., Ofek, E. O., et al. 2013, ApJ, 778, L19
Hunter, D. J., Valenti, S., Kotak, R., et al. 2009, A&A, 508, 371
Iglesias, C. A. & Rogers, F. J. 1996, ApJ, 464, 943
Iwamoto, K., Young, T. R., Nakasato, N., et al. 1997, ApJ, 477, 865
Jerkstrand, A., Ergon, M., Smartt, S., et al. 2014, In preparation
Jerkstrand, A., Fransson, C., & Kozma, C. 2011, A&A, 530, A45

Jerkstrand, A., Fransson, C., Maguire, K., et al. 2012, A&A, 546, A28
Kozma, C. & Fransson, C. 1992, ApJ, 390, 602
Kozma, C. & Fransson, C. 1998a, ApJ, 496, 946
Kozma, C. & Fransson, C. 1998b, ApJ, 497, 431
Lavaux, G. & Hudson, M. J. 2011, MNRAS, 416, 2840
Matheson, T., Filippenko, A. V., Ho, L. C., Barth, A. J., & Leonard, D. C. 2000, AJ, 120, 1499
Matthews, K., Neugebauer, G., Armus, L., & Soifer, B. T. 2002, AJ, 123, 753
Maund, J. R., Fraser, M., Ergon, M., et al. 2011, ApJ, 739, L37
Maund, J. R., Smartt, S. J., Kudritzki, R. P., Podsiadlowski, P., & Gilmore, G. F. 2004, Nature, 427, 129
Maurer, I., Mazzali, P. A., Taubenberger, S., & Hachinger, S. 2010, MNRAS, 409, 1441
Milisavljevic, D., Fesen, R. A., Gerardy, C. L., Kirshner, R. P., & Challis, P. 2010, ApJ, 709, 1343
Paxton, B., Bildsten, L., Dotter, A., et al. 2011, ApJS, 192, 3
Paxton, B., Cantiello, M., Arras, P., et al. 2013, ApJS, 208, 4
Podsiadlowski, P., Hsu, J. J. L., Joss, P. C., & Ross, R. R. 1993, Nature, 364, 509
Sahu, D. K., Anupama, G. C., & Chakradhari, N. K. 2013, MNRAS, 433, 2
Shetty, R., Vogel, S. N., Ostriker, E. C., & Teuben, P. J. 2007, ApJ, 665, 1138
Shigeyama, T., Suzuki, T., Kumagai, S., et al. 1994, ApJ, 420, 341
Shivvers, I., Mazzali, P., Silverman, J. M., et al. 2013, ArXiv e-prints
Spyromilio, J. 1994, MNRAS, 266, L61
Spyromilio, J., Meikle, W. P. S., Learner, R. C. M., & Allen, D. A. 1988, Nature, 334, 327
Stancliffe, R. J. & Eldridge, J. J. 2009, MNRAS, 396, 1699
Stathakis, R. A., Dopita, M. A., Cannon, R. D., & Sadler, E. M. 1991, Supernovae, 649
Suntzeff, N. B. & Bouchet, P. 1990, AJ, 99, 650
Taubenberger, S., Navasardyan, H., Maurer, J. I., et al. 2011, MNRAS, 413, 2140
Taubenberger, S., Valenti, S., Benetti, S., et al. 2009, MNRAS, 397, 677
Tsvetkov, D. Y., Volkov, I. M., Baklanov, P., Blinnikov, S., & Tuchin, O. 2009, Peremennye Zvezdy, 29, 2
Tsvetkov, D. Y., Volkov, I. M., Sorokina, E., et al. 2012, Peremennye Zvezdy, 32, 6
Tully, R. B. 1974, ApJS, 27, 449
Tully, R. B., Shaya, E. J., Karachentsev, I. D., et al. 2008, ApJ, 676, 184
Van Dyk, S. D., Li, W., Cenko, S. B., et al. 2011, ApJ, 741, L28
Van Dyk, S. D., Zheng, W., Clubb, K. I., et al. 2013, ApJ, 772, L32
Woosley, S. E. & Heger, A. 2007, Phys. Rep., 442, 269
Yaron, O. & Gal-Yam, A. 2012, PASP, 124, 668

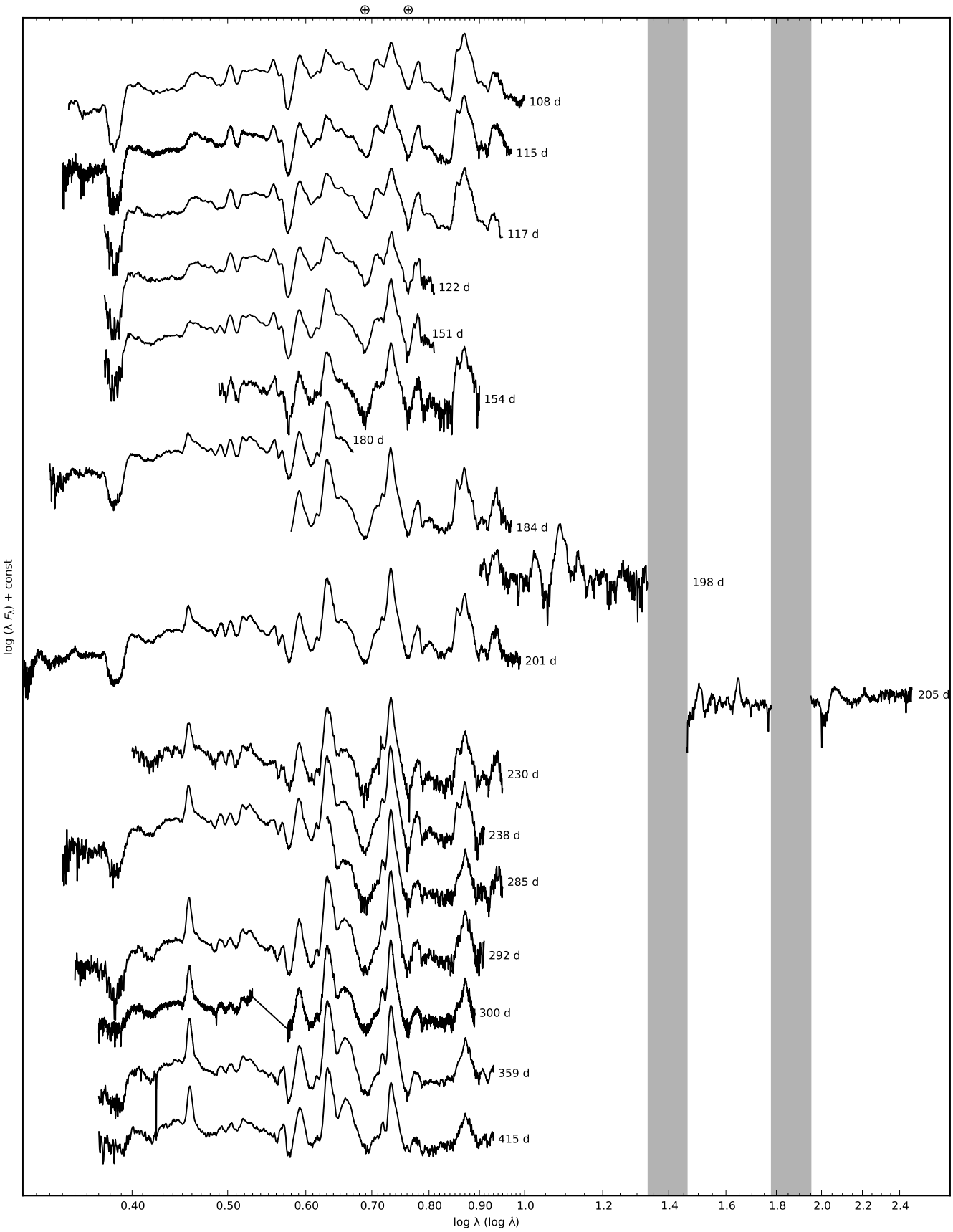

Fig. 7. Sequence of the observed late-time (100-415 days) spectra for SN 2011dh. Spectra obtained on the same night using the same telescope and instrument have been combined and each spectra have been labelled with the phase of the SN. Telluric absorption bands are marked with a ⊕ symbol in the optical and shown as grey regions in the NIR.

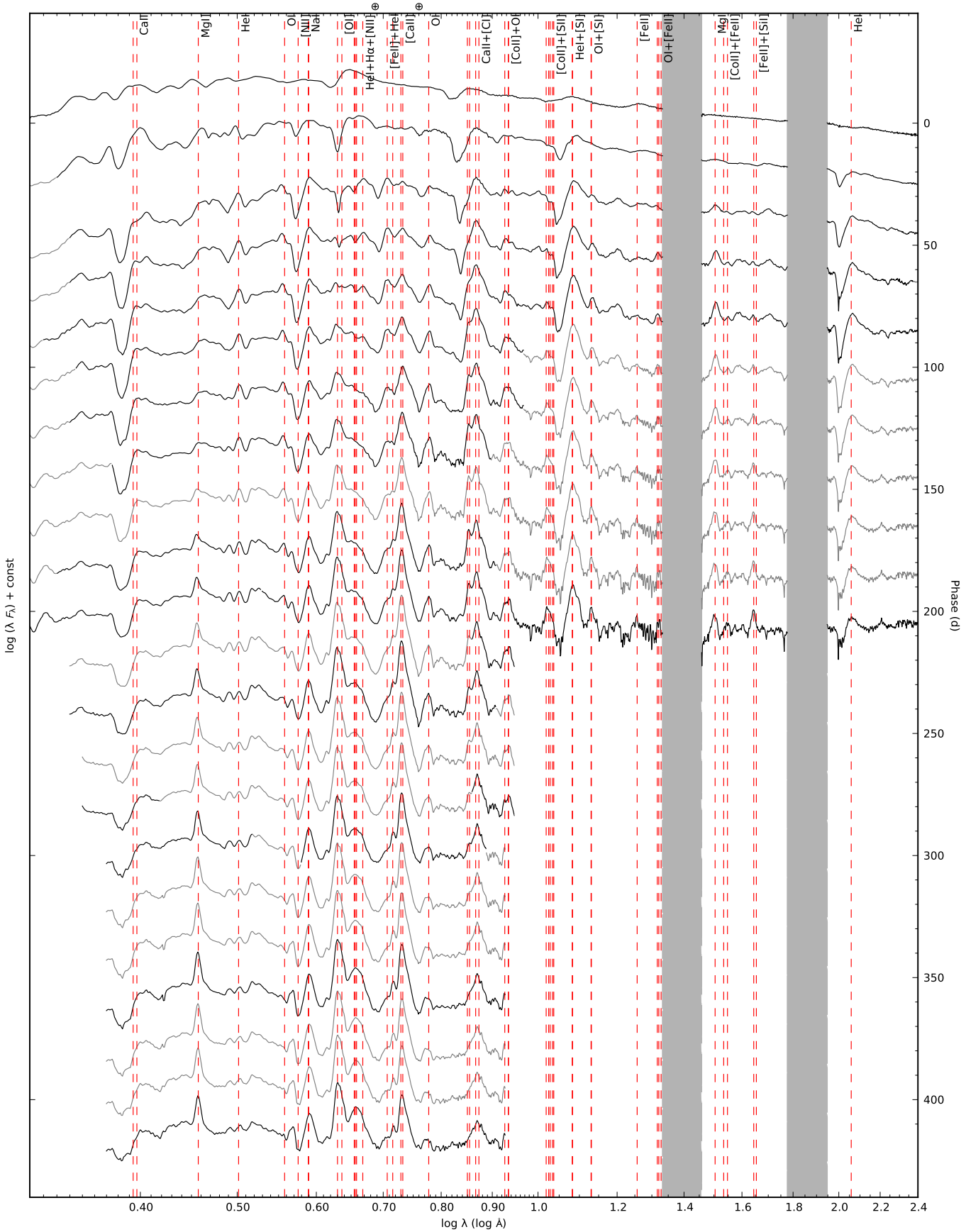

Fig. 8. Optical and NIR (interpolated) spectral evolution for SN 2011dh for days 5−425 with a 20-day sampling. Telluric absorption bands are marked with a ⊕ symbol in the optical and shown as grey regions in the NIR.

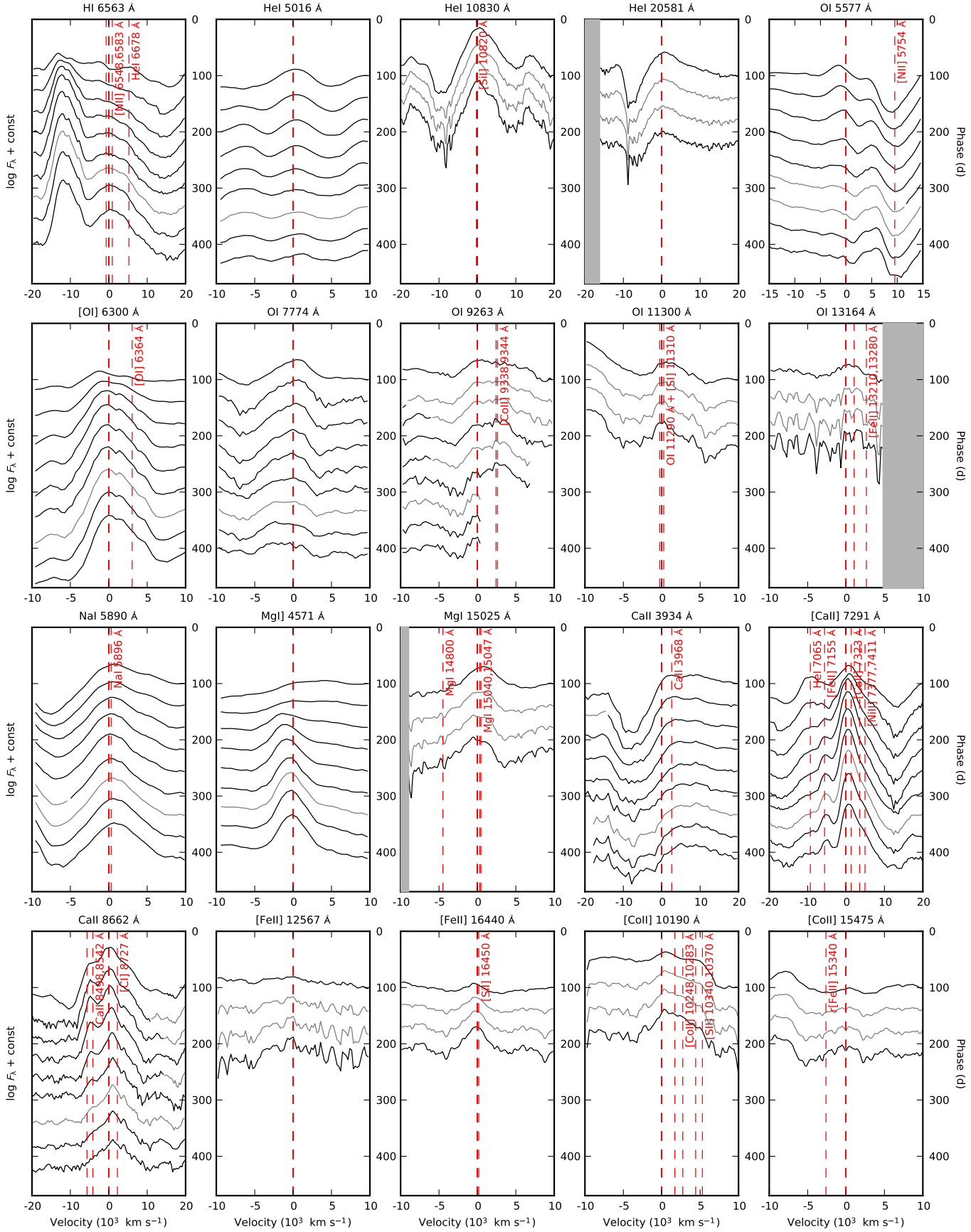

Fig. 9. Spectral evolution of all identified lines. Multiple or blended lines are marked with red dashed lines and telluric absorption bands in the NIR shown as grey regions.

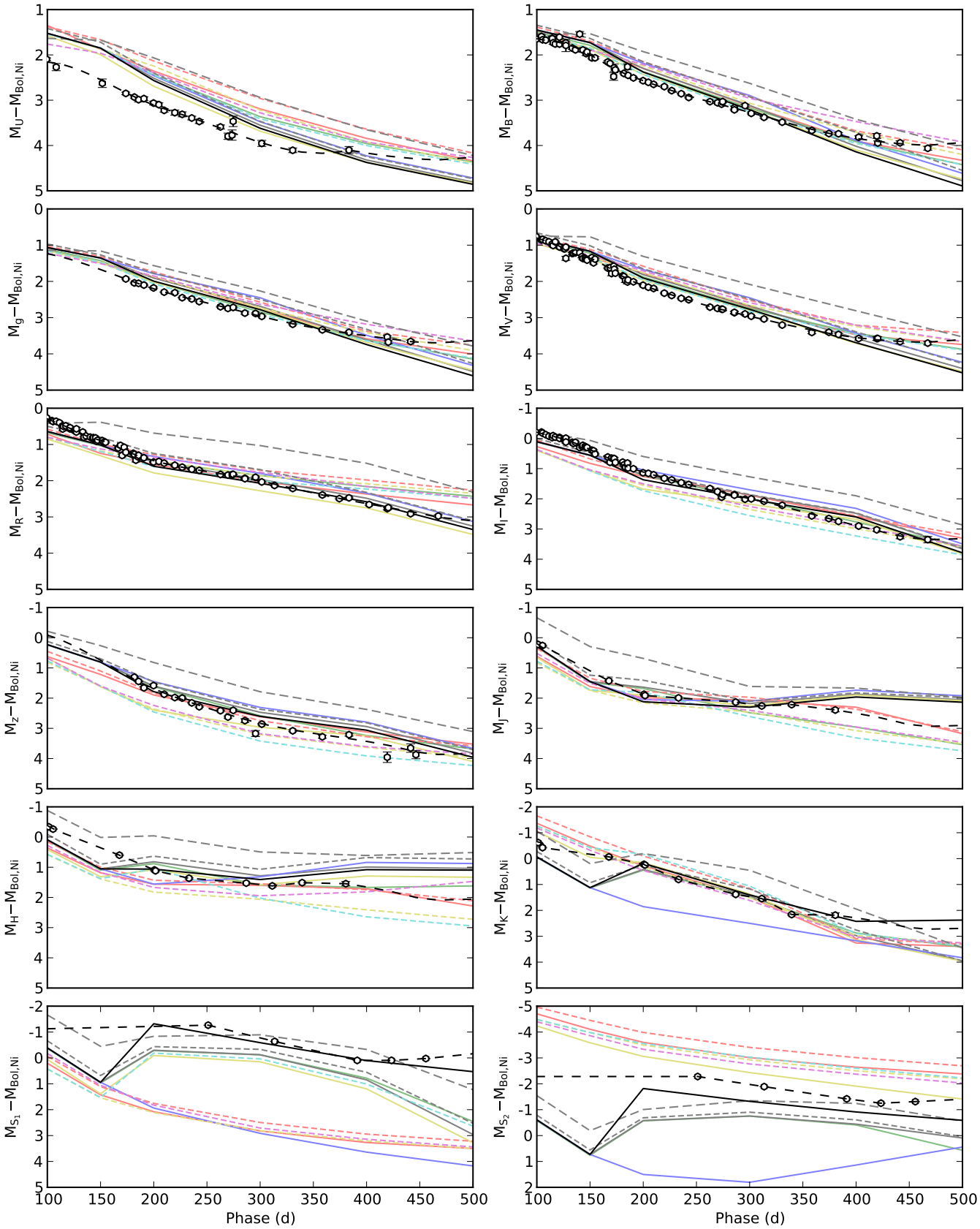

Fig. 20. The 100-500 days observed (black circles) and J14 model optical, NIR and MIR (absolute) magnitudes normalized to the radioactive decay chain luminosity of 0.075 $M_\odot$ of ^{56}Ni. The preferred model (12F) is shown in full colour and all other models in shaded colour. The models are displayed as follows; 12A (red solid line), 12B (green solid line), 12C (black solid line), 12D (yellow solid line), 12E (blue solid line), 12F (black solid line), 13A (red short-dashed line), 13C (yellow short-dashed line), 13D (cyan short-dashed line), 13E (magenta short-dashed line), 13G (black short-dashed line), 17A (black long-dashed line).

Table 4. Optical colour-corrected JC *U* and S-corrected JC *BVRI* magnitudes for SN 2011dh. Errors are given in parentheses. For completeness data for the first 100 days already published in E14a are included.

JD (+2400000) (d)	Phase (d)	*U* (mag)	*B* (mag)	*V* (mag)	*R* (mag)	*I* (mag)	Telescope (Instrument)
55716.43	3.43	14.99 (0.03)	15.35 (0.02)	14.92 (0.02)	14.55 (0.01)	14.42 (0.02)	LT (RATCam)
55716.43	3.43	15.15 (0.08)	15.39 (0.02)	14.95 (0.02)	14.58 (0.01)	14.47 (0.01)	TNG (LRS)
55717.43	4.43	15.03 (0.03)	15.14 (0.02)	14.67 (0.03)	14.26 (0.01)	14.26 (0.03)	LT (RATCam)
55717.48	4.48	15.17 (0.09)	15.21 (0.03)	14.63 (0.03)	14.24 (0.01)	14.23 (0.02)	AS-1.82m (AFOSC)
55717.48	4.48	...	15.12 (0.03)	14.63 (0.02)	14.28 (0.01)	14.28 (0.02)	CANTAB (BIGST8)
55718.48	5.48	...	14.84 (0.01)	14.28 (0.02)	13.95 (0.01)	13.94 (0.01)	LT (RATCam)
55718.57	5.57	14.68 (0.06)	14.84 (0.02)	14.24 (0.02)	13.92 (0.01)	14.05 (0.01)	CA-2.2m (CAFOS)
55720.42	7.42	14.42 (0.02)	14.25 (0.01)	13.75 (0.03)	13.42 (0.01)	13.43 (0.02)	LT (RATCam)
55721.42	8.42	14.28 (0.10)	14.02 (0.01)	13.48 (0.01)	13.23 (0.01)	13.24 (0.02)	LT (RATCam)
55721.43	8.43	14.07 (0.07)	14.06 (0.01)	13.60 (0.04)	13.27 (0.02)	13.34 (0.02)	NOT (ALFOSC)
55722.42	9.42	...	13.86 (0.01)	13.29 (0.01)	13.06 (0.01)	13.07 (0.01)	LT (RATCam)
55723.41	10.41	13.98 (0.06)	13.71 (0.01)	13.16 (0.01)	12.89 (0.01)	12.89 (0.01)	LT (RATCam)
55724.41	11.41	13.91 (0.08)	13.61 (0.01)	13.03 (0.01)	12.80 (0.01)	12.77 (0.01)	LT (RATCam)
55725.39	12.39	...	...	12.94 (0.02)	12.67 (0.01)	...	MONTCAB (BIGST8)
55725.43	12.43	13.88 (0.07)	13.52 (0.02)	12.92 (0.04)	12.68 (0.01)	12.68 (0.01)	LT (RATCam)
55726.36	13.36	...	13.52 (0.01)	12.91 (0.02)	12.60 (0.01)	...	MONTCAB (BIGST8)
55728.40	15.40	...	13.39 (0.01)	12.78 (0.01)	12.45 (0.01)	...	MONTCAB (BIGST8)
55729.39	16.39	13.65 (0.01)	13.34 (0.01)	12.77 (0.06)	12.40 (0.01)	12.34 (0.02)	LT (RATCam)
55730.40	17.40	13.64 (0.03)	13.33 (0.01)	12.66 (0.01)	12.37 (0.01)	12.32 (0.01)	LT (RATCam)
55731.41	18.41	13.74 (0.09)	13.30 (0.01)	12.60 (0.02)	12.32 (0.01)	12.27 (0.01)	LT (RATCam)
55731.82	18.82	...	...	...	12.33 (0.02)	12.25 (0.01)	FTN (FS02)
55732.40	19.40	...	13.35 (0.03)	12.61 (0.01)	12.28 (0.01)	12.21 (0.01)	CANTAB (BIGST8)
55732.41	19.41	13.44 (0.06)	13.36 (0.02)	12.64 (0.02)	12.34 (0.02)	12.31 (0.02)	NOT (ALFOSC)
55732.46	19.46	13.71 (0.07)	13.31 (0.01)	12.58 (0.01)	12.29 (0.02)	12.22 (0.01)	LT (RATCam)
55733.45	20.45	13.67 (0.07)	...	...	12.27 (0.01)	12.20 (0.02)	LT (RATCam)
55734.52	21.52	13.37 (0.05)	13.33 (0.01)	12.58 (0.01)	12.26 (0.01)	12.29 (0.01)	CA-2.2m (CAFOS)
55735.44	22.44	13.91 (0.04)	...	...	12.27 (0.01)	12.15 (0.01)	LT (RATCam)
55736.44	23.44	14.13 (0.08)	...	...	12.27 (0.01)	12.16 (0.01)	LT (RATCam)
55737.39	24.39	...	13.65 (0.01)	12.73 (0.01)	...	...	LT (RATCam)
55738.42	25.42	14.50 (0.04)	13.78 (0.02)	12.81 (0.01)	12.33 (0.02)	12.22 (0.01)	LT (RATCam)
55738.51	25.51	14.20 (0.04)	13.77 (0.02)	12.83 (0.01)	12.39 (0.01)	12.26 (0.01)	NOT (ALFOSC)
55739.43	26.43	14.73 (0.04)	13.95 (0.02)	12.88 (0.01)	12.39 (0.01)	12.23 (0.01)	LT (RATCam)
55740.36	27.36	...	14.08 (0.04)	12.94 (0.01)	12.46 (0.01)	12.29 (0.01)	MONTCAB (BIGST8)
55740.43	27.43	14.91 (0.03)	14.11 (0.01)	12.98 (0.01)	12.49 (0.01)	12.29 (0.01)	LT (RATCam)
55740.44	27.44	...	...	12.97 (0.01)	12.48 (0.01)	...	TJO (MEIA)
55741.44	28.44	...	...	...	12.55 (0.01)	12.31 (0.01)	LT (RATCam)
55742.49	29.49	15.33 (0.01)	...	...	12.63 (0.01)	12.40 (0.01)	LT (RATCam)
55743.41	30.41	...	14.52 (0.01)	13.27 (0.02)	...	...	LT (RATCam)
55743.42	30.42	15.18 (0.05)	14.51 (0.02)	...	12.66 (0.01)	12.53 (0.01)	CA-2.2m (CAFOS)
55743.42	30.42	15.43 (0.05)	14.52 (0.01)	13.26 (0.03)	12.69 (0.01)	12.49 (0.01)	NOT (ALFOSC)
55745.39	32.39	15.74 (0.03)	14.73 (0.01)	13.44 (0.01)	12.79 (0.01)	12.56 (0.01)	NOT (ALFOSC)
55745.44	32.44	15.93 (0.04)	...	...	12.82 (0.01)	12.53 (0.01)	LT (RATCam)
55745.80	32.80	...	...	...	12.80 (0.01)	12.51 (0.01)	FTN (FS02)
55746.45	33.45	16.07 (0.04)	14.86 (0.03)	13.51 (0.01)	12.84 (0.01)	12.55 (0.02)	LT (RATCam)
55747.44	34.44	16.12 (0.04)	...	...	12.89 (0.01)	12.59 (0.01)	LT (RATCam)
55748.43	35.43	16.02 (0.02)	14.95 (0.01)	13.63 (0.01)	12.90 (0.01)	12.65 (0.01)	NOT (ALFOSC)
55748.44	35.44	16.27 (0.04)	...	...	12.95 (0.01)	12.62 (0.01)	LT (RATCam)
55750.40	37.40	16.20 (0.04)	15.09 (0.01)	13.74 (0.01)	13.04 (0.01)	12.73 (0.01)	NOT (ALFOSC)
55750.42	37.42	16.41 (0.14)	15.10 (0.02)	13.78 (0.03)	13.04 (0.01)	12.73 (0.02)	LT (RATCam)
55751.41	38.41	...	15.13 (0.01)	13.81 (0.01)	13.10 (0.01)	12.73 (0.01)	TJO (MEIA)
55751.43	38.43	...	...	...	13.12 (0.01)	12.76 (0.01)	LT (RATCam)
55752.45	39.45	16.54 (0.16)	...	...	13.14 (0.01)	12.74 (0.01)	LT (RATCam)

Table 4. Continued.

JD (+2400000) (d)	Phase (d)	*U* (mag)	*B* (mag)	*V* (mag)	*R* (mag)	*I* (mag)	Telescope (Instrument)
55753.42	40.42	...	15.28 (0.01)	13.91 (0.02)	...	...	LT (RATCam)
55753.46	40.46	16.45 (0.05)	15.23 (0.01)	13.86 (0.01)	13.17 (0.01)	12.81 (0.01)	NOT (ALFOSC)
55755.40	42.40	16.42 (0.04)	15.29 (0.01)	13.97 (0.01)	13.24 (0.01)	12.89 (0.01)	NOT (ALFOSC)
55756.44	43.44	...	15.26 (0.02)	13.99 (0.02)	13.30 (0.02)	12.86 (0.01)	AS-Schmidt (SBIG)
55756.45	43.45	...	15.37 (0.02)	13.98 (0.01)	13.28 (0.03)	12.92 (0.01)	LT (RATCam)
55757.43	44.43	16.42 (0.04)	15.37 (0.01)	14.05 (0.01)	13.30 (0.01)	12.97 (0.01)	NOT (ALFOSC)
55759.45	46.45	...	15.43 (0.01)	14.07 (0.02)	...	...	LT (RATCam)
55761.40	48.40	...	15.42 (0.01)	14.18 (0.01)	13.46 (0.01)	13.03 (0.01)	AS-Schmidt (SBIG)
55762.41	49.41	...	15.44 (0.01)	14.17 (0.01)	13.46 (0.01)	13.06 (0.01)	NOT (ALFOSC)
55762.78	49.78	...	...	...	13.44 (0.01)	13.03 (0.01)	FTN (FS02)
55763.44	50.44	...	15.45 (0.01)	14.22 (0.01)	13.49 (0.01)	13.10 (0.01)	AS-Schmidt (SBIG)
55765.43	52.43	16.44 (0.03)	15.51 (0.01)	14.26 (0.01)	13.57 (0.01)	13.17 (0.01)	NOT (ALFOSC)
55767.43	54.43	16.50 (0.05)	...	...	13.59 (0.01)	13.17 (0.02)	LT (RATCam)
55768.45	55.45	16.48 (0.04)	...	...	13.60 (0.02)	13.19 (0.02)	LT (RATCam)
55771.40	58.40	16.37 (0.03)	15.58 (0.01)	14.33 (0.01)	13.64 (0.01)	13.29 (0.01)	CA-2.2m (CAFOS)
55773.39	60.39	16.45 (0.04)	15.59 (0.01)	14.39 (0.01)	13.72 (0.01)	13.32 (0.01)	NOT (ALFOSC)
55776.38	63.38	16.47 (0.04)	15.63 (0.01)	14.46 (0.01)	13.79 (0.01)	13.36 (0.01)	NOT (ALFOSC)
55777.33	64.33	...	15.50 (0.03)	14.46 (0.02)	13.79 (0.02)	13.35 (0.02)	AS-Schmidt (SBIG)
55780.40	67.40	16.42 (0.03)	15.65 (0.01)	14.51 (0.01)	13.86 (0.01)	13.43 (0.01)	NOT (ALFOSC)
55782.38	69.38	16.31 (0.07)	...	...	13.89 (0.01)	13.47 (0.01)	LT (RATCam)
55783.43	70.43	16.41 (0.03)	15.70 (0.01)	14.58 (0.01)	13.95 (0.01)	13.51 (0.01)	NOT (ALFOSC)
55784.33	71.33	...	15.65 (0.02)	14.59 (0.01)	...	13.43 (0.02)	AS-Schmidt (SBIG)
55784.39	71.39	16.45 (0.04)	15.66 (0.01)	14.52 (0.02)	13.91 (0.01)	13.48 (0.02)	CA-2.2m (CAFOS)
55784.77	71.77	...	...	...	13.93 (0.02)	13.45 (0.01)	FTN (FS02)
55785.36	72.36	...	15.69 (0.02)	14.62 (0.01)	13.97 (0.01)	13.46 (0.01)	AS-Schmidt (SBIG)
55788.41	75.41	...	...	...	14.03 (0.02)	13.52 (0.01)	AS-Schmidt (SBIG)
55790.38	77.38	16.45 (0.09)	...	...	14.04 (0.01)	13.61 (0.01)	LT (RATCam)
55793.37	80.37	16.55 (0.07)	15.79 (0.01)	14.75 (0.01)	14.14 (0.01)	13.68 (0.01)	NOT (ALFOSC)
55795.35	82.35	16.40 (0.04)	15.78 (0.01)	14.76 (0.01)	14.14 (0.01)	13.69 (0.01)	CA-2.2m (CAFOS)
55797.37	84.37	...	15.81 (0.02)	14.82 (0.01)	...	...	AS-Schmidt (SBIG)
55797.76	84.76	...	...	...	14.22 (0.01)	13.68 (0.01)	FTN (FS02)
55798.36	85.36	16.50 (0.03)	15.83 (0.01)	14.84 (0.01)	14.26 (0.01)	13.65 (0.02)	NOT (ALFOSC)
55799.33	86.33	...	15.81 (0.01)	14.87 (0.01)	...	...	AS-Schmidt (SBIG)
55801.36	88.36	16.44 (0.04)	15.88 (0.01)	14.90 (0.01)	14.32 (0.01)	13.81 (0.01)	NOT (ALFOSC)
55801.40	88.40	...	15.79 (0.02)	14.90 (0.01)	...	...	AS-Schmidt (SBIG)
55803.35	90.35	...	15.86 (0.02)	14.91 (0.01)	14.34 (0.01)	13.80 (0.01)	AS-Schmidt (SBIG)
55805.33	92.33	...	15.85 (0.02)	14.97 (0.02)	14.38 (0.01)	13.84 (0.01)	AS-Schmidt (SBIG)
55810.34	97.34	16.68 (0.06)	15.99 (0.01)	15.11 (0.01)	14.53 (0.01)	14.03 (0.01)	NOT (ALFOSC)
55812.33	99.33	16.51 (0.03)	16.01 (0.01)	15.06 (0.01)	14.51 (0.01)	14.01 (0.01)	CA-2.2m (CAFOS)
55817.35	104.35	...	16.00 (0.03)	15.20 (0.02)	14.64 (0.02)	14.04 (0.02)	AS-Schmidt (SBIG)
55818.33	105.33	...	16.08 (0.02)	15.19 (0.02)	14.68 (0.01)	14.09 (0.01)	AS-Schmidt (SBIG)
55821.31	108.31	16.77 (0.08)	16.12 (0.02)	15.26 (0.01)	14.70 (0.01)	14.17 (0.01)	CA-2.2m (CAFOS)
55824.32	111.32	...	...	15.31 (0.02)	14.77 (0.03)	14.25 (0.03)	AS-Schmidt (SBIG)
55827.33	114.33	...	16.14 (0.03)	15.42 (0.01)	14.88 (0.02)	14.28 (0.01)	AS-Schmidt (SBIG)
55827.48	114.48	...	16.15 (0.06)	15.41 (0.03)	14.97 (0.05)	14.32 (0.05)	AT (ANDOR)
55828.27	115.27	...	16.25 (0.03)	15.46 (0.02)	14.91 (0.01)	14.27 (0.01)	AT (ANDOR)
55830.28	117.28	...	16.30 (0.02)	15.38 (0.01)	14.91 (0.01)	14.34 (0.01)	AS-1.82m (AFOSC)
55834.26	121.26	...	16.18 (0.03)	15.55 (0.03)	15.03 (0.01)	14.38 (0.02)	AT (ANDOR)
55834.31	121.31	...	16.34 (0.02)	15.56 (0.01)	15.00 (0.02)	14.42 (0.02)	AS-Schmidt (SBIG)
55838.34	125.34	...	...	15.64 (0.02)	15.12 (0.03)	14.49 (0.01)	AS-Schmidt (SBIG)
55839.28	126.28	...	16.37 (0.03)	15.65 (0.02)	15.13 (0.02)	14.52 (0.02)	AS-Schmidt (SBIG)
55840.26	127.26	...	16.37 (0.03)	15.62 (0.02)	15.18 (0.02)	14.47 (0.02)	AT (ANDOR)
55840.30	127.30	...	16.42 (0.14)	15.93 (0.06)	15.09 (0.04)	14.60 (0.04)	AS-Schmidt (SBIG)

Table 4. Continued.

JD (+2400000) (d)	Phase (d)	*U* (mag)	*B* (mag)	*V* (mag)	*R* (mag)	*I* (mag)	Telescope (Instrument)
55846.26	133.26	...	16.54 (0.03)	15.85 (0.03)	15.24 (0.02)	14.66 (0.02)	AT (ANDOR)
55847.30	134.30	...	...	15.85 (0.03)	15.39 (0.02)	14.71 (0.02)	AT (ANDOR)
55849.26	136.26	...	16.61 (0.04)	15.86 (0.03)	15.38 (0.02)	14.69 (0.02)	AT (ANDOR)
55853.27	140.27	...	16.30 (0.06)	15.90 (0.05)	15.45 (0.05)	14.91 (0.04)	AS-Schmidt (SBIG)
55855.38	142.38	...	...	16.02 (0.03)	15.50 (0.03)	14.89 (0.03)	AT (ANDOR)
55856.24	143.24	...	16.68 (0.05)	16.08 (0.03)	15.49 (0.02)	14.86 (0.02)	AT (ANDOR)
55858.29	145.29	...	...	16.10 (0.03)	15.52 (0.02)	14.92 (0.03)	AT (ANDOR)
55859.23	146.23	...	16.79 (0.04)	16.14 (0.03)	15.62 (0.03)	14.96 (0.03)	AT (ANDOR)
55860.22	147.22	...	16.76 (0.04)	16.17 (0.04)	15.60 (0.02)	14.97 (0.02)	AT (ANDOR)
55864.69	151.69	17.55 (0.09)	16.94 (0.02)	16.14 (0.01)	15.65 (0.01)	15.10 (0.01)	AS-1.82m (AFOSC)
55866.28	153.28	...	...	16.30 (0.03)	15.71 (0.02)	15.14 (0.02)	AT (ANDOR)
55867.70	154.70	...	16.97 (0.02)	16.22 (0.03)	15.73 (0.02)	15.26 (0.02)	CA-2.2m (CAFOS)
55879.66	166.66	...	17.17 (0.03)	16.58 (0.02)	16.00 (0.02)	15.48 (0.02)	AS-Schmidt (SBIG)
55881.74	168.74	...	17.23 (0.02)	16.59 (0.02)	15.95 (0.01)	15.67 (0.03)	CA-2.2m (CAFOS)
55883.24	170.24	...	...	16.76 (0.06)	16.24 (0.04)	15.55 (0.03)	AT (ANDOR)
55885.21	172.21	...	17.55 (0.08)	16.58 (0.04)	16.04 (0.04)	15.58 (0.03)	AT (ANDOR)
55885.73	172.73	...	17.36 (0.08)	16.67 (0.02)	...	15.59 (0.03)	AS-1.82m (AFOSC)
55886.75	173.75	17.99 (0.03)	17.42 (0.01)	16.79 (0.01)	16.19 (0.01)	15.72 (0.01)	NOT (ALFOSC)
55893.71	180.71	...	...	16.93 (0.02)	16.29 (0.01)	15.78 (0.02)	AS-Schmidt (SBIG)
55894.76	181.76	18.15 (0.02)	17.57 (0.01)	16.96 (0.01)	16.33 (0.01)	15.88 (0.01)	NOT (ALFOSC)
55896.20	183.20	...	...	17.08 (0.06)	16.50 (0.05)	15.97 (0.04)	AT (ANDOR)
55898.19	185.19	...	17.46 (0.06)	17.14 (0.05)	16.43 (0.04)	15.86 (0.03)	AT (ANDOR)
55898.73	185.73	18.24 (0.05)	17.65 (0.01)	17.09 (0.01)	16.39 (0.01)	16.03 (0.01)	NOT (ALFOSC)
55903.76	190.76	18.27 (0.04)	17.76 (0.02)	17.19 (0.02)	16.51 (0.02)	16.10 (0.02)	NOT (ALFOSC)
55912.79	199.79	18.46 (0.04)	17.91 (0.02)	17.37 (0.02)	16.72 (0.01)	16.32 (0.01)	NOT (ALFOSC)
55917.79	204.79	18.54 (0.04)	17.99 (0.01)	17.48 (0.01)	16.75 (0.01)	16.39 (0.01)	NOT (ALFOSC)
55922.76	209.76	18.71 (0.04)	18.09 (0.01)	17.56 (0.01)	16.84 (0.01)	16.48 (0.01)	NOT (ALFOSC)
55932.79	219.79	18.86 (0.06)	18.23 (0.01)	17.79 (0.02)	17.00 (0.02)	16.70 (0.02)	NOT (ALFOSC)
55939.73	226.73	18.97 (0.05)	18.39 (0.01)	17.92 (0.02)	17.12 (0.01)	16.82 (0.01)	NOT (ALFOSC)
55948.73	235.73	19.14 (0.04)	18.55 (0.01)	18.09 (0.02)	17.26 (0.01)	17.00 (0.01)	NOT (ALFOSC)
55955.76	242.76	19.28 (0.04)	18.70 (0.01)	18.19 (0.01)	17.36 (0.01)	17.13 (0.01)	NOT (ALFOSC)
55975.69	262.69	19.60 (0.05)	18.98 (0.01)	18.59 (0.01)	17.67 (0.01)	17.45 (0.01)	NOT (ALFOSC)
55982.74	269.74	19.87 (0.07)	19.08 (0.02)	18.69 (0.02)	17.75 (0.01)	17.62 (0.01)	NOT (ALFOSC)
55986.62	273.62	19.88 (0.11)	19.15 (0.03)	18.75 (0.03)	17.78 (0.02)	17.85 (0.03)	CA-2.2m (CAFOS)
55987.62	274.62	19.59 (0.12)	19.10 (0.02)	18.77 (0.02)	17.78 (0.01)	17.76 (0.01)	LT (RATCam)
55998.66	285.66	...	19.34 (0.04)	18.97 (0.04)	18.00 (0.02)	17.88 (0.02)	LT (RATCam)
55998.67	285.67	...	19.39 (0.02)	18.96 (0.02)	18.01 (0.01)	17.90 (0.01)	NOT (ALFOSC)
56008.66	295.66	...	19.39 (0.03)	19.10 (0.03)	18.07 (0.02)	18.13 (0.03)	LT (RATCam)
56014.51	301.51	20.34 (0.07)	19.62 (0.01)	19.22 (0.02)	18.25 (0.01)	18.17 (0.01)	NOT (ALFOSC)
56026.49	313.49	...	19.83 (0.02)	19.41 (0.02)	18.47 (0.01)	18.37 (0.02)	NOT (ALFOSC)
56043.59	330.59	20.77 (0.05)	20.10 (0.02)	19.75 (0.02)	18.72 (0.01)	18.67 (0.02)	NOT (ALFOSC)
56071.42	358.42	...	20.55 (0.02)	20.22 (0.03)	19.17 (0.02)	19.29 (0.03)	NOT (ALFOSC)
56087.43	374.43	...	20.78 (0.02)	20.37 (0.03)	19.42 (0.02)	19.54 (0.02)	NOT (ALFOSC)
56096.48	383.48	21.28 (0.08)	20.87 (0.03)	20.52 (0.03)	19.49 (0.02)	19.72 (0.03)	NOT (ALFOSC)
56115.44	402.44	...	21.13 (0.03)	20.82 (0.04)	19.86 (0.02)	20.06 (0.04)	NOT (ALFOSC)
56132.43	419.43	...	21.27 (0.05)	20.99 (0.05)	20.14 (0.03)	20.35 (0.05)	NOT (ALFOSC)
56133.40	420.40	...	21.43 (0.05)	20.99 (0.05)	20.12 (0.03)	...	NOT (ALFOSC)
56154.39	441.39	...	21.63 (0.04)	21.28 (0.05)	20.49 (0.03)	20.79 (0.06)	NOT (ALFOSC)
56180.37	467.37	...	22.01 (0.04)	21.58 (0.05)	20.81 (0.03)	21.14 (0.11)	NOT (ALFOSC)
56313.73	600.73	...	...	22.44 (0.10)	...	...	NOT (ALFOSC)
56353.50	640.50	...	...	23.02 (0.00)	...	22.58 (0.00)	HST (ACS)
56371.69	658.69	...	23.42 (0.32)	...	...	...	NOT (ALFOSC)
56397.64	684.64	...	...	23.20 (0.20)	...	...	NOT (ALFOSC)
56445.43	732.43	...	23.96 (0.50)	...	...	...	NOT (ALFOSC)

Table 5. Optical colour-corrected SDSS *u* and S-corrected SDSS *griz* magnitudes for SN 2011dh. Errors are given in parentheses. For completeness data for the first 100 days already published in E14a are included.

JD (+2400000) (d)	Phase (d)	*u* (mag)	*g* (mag)	*r* (mag)	*i* (mag)	*z* (mag)	Telescope (Instrument)
55716.47	3.47	15.86 (0.04)	15.08 (0.01)	14.69 (0.01)	14.80 (0.01)	14.76 (0.02)	LT (RATCam)
55717.46	4.46	15.99 (0.03)	14.80 (0.01)	14.39 (0.01)	14.61 (0.01)	14.58 (0.02)	LT (RATCam)
55718.53	5.53	...	14.44 (0.04)	14.06 (0.01)	14.27 (0.01)	...	LT (RATCam)
55720.44	7.44	15.39 (0.02)	13.97 (0.01)	13.53 (0.01)	13.72 (0.02)	13.87 (0.01)	LT (RATCam)
55721.44	8.44	15.08 (0.02)	13.78 (0.01)	13.34 (0.01)	13.51 (0.01)	13.64 (0.01)	LT (RATCam)
55722.44	9.44	...	13.59 (0.01)	13.18 (0.01)	13.34 (0.01)	13.49 (0.01)	LT (RATCam)
55723.41	10.41	14.80 (0.03)	...	13.03 (0.01)	13.16 (0.01)	13.34 (0.01)	LT (RATCam)
55724.41	11.41	14.70 (0.02)	...	12.93 (0.01)	13.05 (0.01)	13.22 (0.01)	LT (RATCam)
55725.43	12.43	14.72 (0.04)	...	12.83 (0.01)	12.93 (0.01)	13.10 (0.01)	LT (RATCam)
55729.39	16.39	14.56 (0.03)	13.10 (0.01)	12.56 (0.01)	12.61 (0.01)	12.81 (0.01)	LT (RATCam)
55730.40	17.40	14.45 (0.03)	13.07 (0.01)	12.51 (0.01)	12.56 (0.01)	12.78 (0.01)	LT (RATCam)
55731.41	18.41	14.54 (0.04)	13.02 (0.01)	12.46 (0.01)	12.50 (0.01)	12.72 (0.01)	LT (RATCam)
55731.82	18.82	...	13.07 (0.01)	12.46 (0.01)	12.50 (0.01)	12.65 (0.01)	FTN (FS02)
55732.46	19.46	14.57 (0.02)	12.99 (0.03)	12.43 (0.01)	12.47 (0.01)	12.68 (0.01)	LT (RATCam)
55733.45	20.45	14.53 (0.05)	13.02 (0.01)	12.42 (0.01)	12.44 (0.01)	12.65 (0.01)	LT (RATCam)
55735.44	22.44	14.77 (0.04)	13.12 (0.01)	12.43 (0.01)	12.41 (0.01)	12.60 (0.01)	LT (RATCam)
55736.44	23.44	14.99 (0.03)	13.19 (0.02)	12.46 (0.01)	12.41 (0.01)	12.59 (0.02)	LT (RATCam)
55738.45	25.45	15.42 (0.03)	13.43 (0.01)	12.56 (0.01)	12.46 (0.01)	12.66 (0.01)	LT (RATCam)
55739.44	26.44	15.60 (0.03)	13.50 (0.03)	12.60 (0.01)	12.50 (0.01)	12.65 (0.01)	LT (RATCam)
55740.44	27.44	15.86 (0.03)	13.65 (0.01)	12.67 (0.01)	12.54 (0.01)	12.70 (0.01)	LT (RATCam)
55741.44	28.44	...	13.75 (0.02)	12.77 (0.01)	12.58 (0.02)	12.76 (0.01)	LT (RATCam)
55742.49	29.49	16.28 (0.04)	13.92 (0.01)	12.84 (0.01)	12.65 (0.01)	12.81 (0.01)	LT (RATCam)
55745.44	32.44	16.80 (0.06)	14.20 (0.02)	13.04 (0.01)	12.78 (0.01)	12.87 (0.03)	LT (RATCam)
55745.80	32.80	...	14.35 (0.04)	13.00 (0.01)	12.79 (0.01)	12.94 (0.01)	FTN (FS02)
55746.45	33.45	16.92 (0.05)	14.31 (0.01)	13.10 (0.01)	12.81 (0.01)	12.94 (0.01)	LT (RATCam)
55747.44	34.44	16.99 (0.05)	14.40 (0.02)	13.14 (0.01)	12.85 (0.01)	12.96 (0.01)	LT (RATCam)
55748.44	35.44	17.18 (0.06)	14.42 (0.02)	13.20 (0.01)	12.90 (0.01)	13.01 (0.01)	LT (RATCam)
55750.44	37.44	17.29 (0.11)	14.55 (0.02)	13.30 (0.01)	13.01 (0.02)	13.05 (0.04)	LT (RATCam)
55751.43	38.43	17.23 (0.04)	14.64 (0.03)	13.36 (0.01)	13.03 (0.01)	13.12 (0.01)	LT (RATCam)
55752.45	39.45	17.34 (0.08)	14.65 (0.01)	13.40 (0.01)	13.03 (0.01)	13.10 (0.01)	LT (RATCam)
55756.46	43.46	...	14.79 (0.01)	13.56 (0.01)	13.22 (0.01)	13.19 (0.01)	LT (RATCam)
55762.78	49.78	...	15.00 (0.02)	13.68 (0.01)	13.37 (0.01)	13.28 (0.01)	FTN (FS02)
55767.43	54.43	17.36 (0.03)	15.02 (0.01)	13.84 (0.01)	13.52 (0.01)	13.38 (0.02)	LT (RATCam)
55768.45	55.45	17.34 (0.03)	15.02 (0.01)	13.87 (0.01)	13.56 (0.01)	13.41 (0.01)	LT (RATCam)
55773.39	60.39	17.19 (0.04)	15.06 (0.01)	14.00 (0.01)	13.72 (0.01)	13.53 (0.02)	NOT (ALFOSC)
55776.38	63.38	17.27 (0.03)	15.12 (0.01)	14.04 (0.01)	13.76 (0.01)	13.55 (0.01)	NOT (ALFOSC)
55780.41	67.41	17.25 (0.03)	15.16 (0.01)	14.10 (0.01)	13.84 (0.01)	13.60 (0.01)	NOT (ALFOSC)
55782.38	69.38	17.17 (0.04)	15.19 (0.01)	14.15 (0.01)	13.86 (0.01)	13.62 (0.01)	LT (RATCam)
55783.44	70.44	17.19 (0.04)	15.18 (0.01)	14.20 (0.01)	13.94 (0.01)	13.66 (0.01)	NOT (ALFOSC)
55784.77	71.77	...	15.23 (0.02)	14.16 (0.01)	13.88 (0.01)	13.64 (0.01)	FTN (FS02)
55790.38	77.38	17.31 (0.03)	15.34 (0.04)	14.29 (0.01)	14.04 (0.01)	13.69 (0.02)	LT (RATCam)
55793.37	80.37	17.26 (0.03)	15.30 (0.01)	14.40 (0.01)	14.16 (0.01)	13.83 (0.01)	NOT (ALFOSC)
55797.76	84.76	...	15.38 (0.01)	14.42 (0.01)	14.18 (0.01)	13.82 (0.01)	FTN (FS02)
55798.37	85.37	17.28 (0.03)	15.37 (0.01)	14.51 (0.01)	14.26 (0.01)	13.86 (0.01)	NOT (ALFOSC)
55801.36	88.36	17.26 (0.02)	15.41 (0.01)	14.54 (0.01)	14.31 (0.01)	13.88 (0.01)	NOT (ALFOSC)
55810.34	97.34	17.41 (0.02)	15.55 (0.01)	14.76 (0.01)	14.56 (0.01)	14.09 (0.02)	NOT (ALFOSC)
55886.75	173.75	18.76 (0.04)	16.99 (0.01)	16.37 (0.01)	16.14 (0.01)	...	NOT (ALFOSC)
55894.76	181.76	18.92 (0.03)	17.18 (0.02)	16.51 (0.01)	16.27 (0.01)	16.29 (0.02)	NOT (ALFOSC)
55898.73	185.73	19.02 (0.04)	17.23 (0.01)	16.58 (0.01)	16.39 (0.01)	16.47 (0.02)	NOT (ALFOSC)
55903.76	190.76	19.13 (0.08)	17.33 (0.02)	16.70 (0.01)	16.45 (0.01)	16.73 (0.04)	NOT (ALFOSC)
55912.79	199.79	19.29 (0.06)	17.49 (0.02)	16.90 (0.01)	16.64 (0.01)	16.74 (0.04)	NOT (ALFOSC)

Table 5. Continued.

JD (+2400000) (d)	Phase (d)	u (mag)	g (mag)	r (mag)	i (mag)	z (mag)	Telescope (Instrument)
55922.77	209.77	19.47 (0.02)	17.71 (0.01)	17.03 (0.01)	16.79 (0.01)	17.13 (0.01)	NOT (ALFOSC)
55932.79	219.79	19.62 (0.05)	17.82 (0.02)	17.20 (0.02)	16.96 (0.02)	17.33 (0.04)	NOT (ALFOSC)
55939.74	226.74	19.76 (0.05)	18.03 (0.01)	17.31 (0.01)	17.07 (0.01)	17.42 (0.02)	NOT (ALFOSC)
55948.73	235.73	19.93 (0.03)	18.15 (0.01)	17.45 (0.01)	17.22 (0.01)	17.67 (0.01)	NOT (ALFOSC)
55955.76	242.76	20.08 (0.03)	18.29 (0.01)	17.56 (0.01)	17.34 (0.01)	17.86 (0.02)	NOT (ALFOSC)
55975.69	262.69	20.32 (0.04)	18.63 (0.01)	17.84 (0.01)	17.65 (0.01)	18.19 (0.02)	NOT (ALFOSC)
55982.74	269.74	20.68 (0.06)	18.74 (0.01)	17.94 (0.01)	17.83 (0.01)	18.47 (0.03)	NOT (ALFOSC)
55987.62	274.62	20.49 (0.11)	18.76 (0.01)	17.95 (0.01)	17.94 (0.01)	18.29 (0.03)	LT (RATCam)
55998.66	285.66	...	19.02 (0.03)	18.15 (0.02)	18.06 (0.02)	18.74 (0.06)	LT (RATCam)
56008.66	295.66	...	19.13 (0.02)	18.22 (0.01)	18.31 (0.03)	19.26 (0.10)	LT (RATCam)
56014.52	301.52	21.08 (0.05)	19.27 (0.01)	18.39 (0.01)	18.41 (0.01)	19.01 (0.02)	NOT (ALFOSC)
56043.60	330.60	21.53 (0.04)	19.77 (0.01)	18.81 (0.01)	18.91 (0.01)	19.51 (0.03)	NOT (ALFOSC)
56071.43	358.43	...	20.20 (0.02)	19.23 (0.02)	19.56 (0.03)	19.98 (0.05)	NOT (ALFOSC)
56096.49	383.49	22.07 (0.07)	20.51 (0.02)	19.52 (0.02)	20.00 (0.03)	20.16 (0.05)	NOT (ALFOSC)
56132.43	419.43	...	20.99 (0.03)	20.16 (0.02)	20.65 (0.04)	21.25 (0.17)	NOT (ALFOSC)
56133.41	420.41	...	21.14 (0.04)	20.13 (0.03)	20.78 (0.05)	...	NOT (ALFOSC)
56154.39	441.39	...	21.32 (0.04)	20.51 (0.03)	21.10 (0.06)	21.17 (0.14)	NOT (ALFOSC)
56159.38	446.38	...	...	...	...	21.43 (0.13)	NOT (ALFOSC)
56313.75	600.75	...	...	22.46 (0.11)	...	...	NOT (ALFOSC)
56428.46	715.46	...	...	23.10 (0.20)	...	...	NOT (ALFOSC)

Table 6. NIR S-corrected 2MASS JHK magnitudes for SN 2011dh. Errors are given in parentheses. For completeness data for the first 100 days already published in E14a are included.

JD (+2400000) (d)	Phase (d)	J (mag)	H (mag)	K (mag)	Telescope (Instrument)
55716.51	3.51	14.09 (0.01)	13.90 (0.01)	13.66 (0.01)	TNG (NICS)
55722.40	9.40	12.92 (0.02)	12.88 (0.01)	12.67 (0.01)	TNG (NICS)
55725.50	12.50	12.61 (0.04)	12.54 (0.01)	12.43 (0.02)	NOT (NOTCAM)
55730.51	17.51	12.07 (0.02)	12.08 (0.01)	11.94 (0.01)	TNG (NICS)
55737.72	24.72	11.96 (0.01)	11.90 (0.01)	11.72 (0.03)	LBT (LUCIFER)
55741.13	28.13	11.94 (0.01)	11.90 (0.02)	11.70 (0.05)	TCS (CAIN)
55748.43	35.43	12.14 (0.01)	12.00 (0.02)	11.77 (0.01)	TCS (CAIN)
55750.42	37.42	12.19 (0.01)	12.00 (0.01)	11.84 (0.04)	TCS (CAIN)
55751.42	38.42	12.29 (0.01)	12.01 (0.01)	11.84 (0.03)	TCS (CAIN)
55758.45	45.45	12.55 (0.01)	12.22 (0.01)	12.07 (0.01)	TNG (NICS)
55759.41	46.41	12.49 (0.03)	12.22 (0.03)	12.11 (0.04)	TCS (CAIN)
55762.41	49.41	12.57 (0.01)	12.26 (0.01)	12.17 (0.03)	TCS (CAIN)
55763.42	50.42	12.62 (0.02)	12.27 (0.04)	12.25 (0.06)	TCS (CAIN)
55765.45	52.45	12.78 (0.01)	12.37 (0.01)	12.24 (0.01)	TNG (NICS)
55769.41	56.41	12.77 (0.01)	12.48 (0.06)	12.40 (0.03)	TCS (CAIN)
55773.37	60.37	12.98 (0.04)	12.58 (0.01)	12.42 (0.01)	TNG (NICS)
55774.40	61.40	12.90 (0.01)	12.55 (0.03)	12.43 (0.04)	TCS (CAIN)
55776.40	63.40	13.00 (0.01)	12.64 (0.01)	12.53 (0.02)	TCS (CAIN)
55781.41	68.41	13.23 (0.01)	12.76 (0.01)	12.66 (0.01)	WHT (LIRIS)
55787.44	74.44	13.56 (0.03)	13.03 (0.02)	12.95 (0.02)	NOT (NOTCAM)
55794.41	81.41	...	13.18 (0.01)	...	TNG (NICS)
55801.36	88.36	13.90 (0.01)	13.41 (0.01)	13.18 (0.01)	TNG (NICS)
55804.34	91.34	14.10 (0.01)	13.50 (0.01)	13.26 (0.01)	CA-3.5m (O2000)
55814.32	101.32	14.38 (0.01)	13.80 (0.01)	13.50 (0.01)	CA-3.5m (O2000)
55818.36	105.36	14.45 (0.02)	13.91 (0.01)	13.74 (0.01)	NOT (NOTCAM)
55880.72	167.72	16.23 (0.01)	15.38 (0.01)	14.70 (0.01)	CA-3.5m (O2000)
55913.68	200.68	17.00 (0.01)	16.19 (0.02)	15.31 (0.02)	CA-3.5m (O2000)
55914.66	201.66	17.05 (0.01)	16.23 (0.02)	15.35 (0.02)	CA-3.5m (O2000)
55946.13	233.13	17.43 (0.02)	16.78 (0.02)	16.21 (0.02)	UKIRT (WFCAM)
55999.91	286.91	18.10 (0.02)	17.47 (0.02)	17.31 (0.02)	UKIRT (WFCAM)
56024.38	311.38	18.46 (0.03)	17.80 (0.03)	17.71 (0.04)	WHT (LIRIS)
56052.47	339.47	18.69 (0.02)	17.96 (0.02)	18.60 (0.03)	WHT (LIRIS)
56093.48	380.48	19.27 (0.06)	18.40 (0.07)	19.02 (0.09)	WHT (LIRIS)

Table 7. MIR Spitzer S_1 and S_2 magnitudes for SN 2011dh. Errors are given in parentheses. For completeness data for the first 100 days already published in E14a are included.

JD (+2400000) (d)	Phase (d)	S_1 (mag)	S_2 (mag)	Telescope (Instrument)
55731.21	18.21	11.826 0.001	11.479 0.001	SPITZER (IRAC)
55737.06	24.06	11.661 0.001	11.314 0.001	SPITZER (IRAC)
55744.32	31.32	11.659 0.001	11.301 0.001	SPITZER (IRAC)
55751.46	38.46	11.684 0.001	11.300 0.001	SPITZER (IRAC)
55758.75	45.75	11.788 0.001	11.316 0.001	SPITZER (IRAC)
55766.45	53.45	11.958 0.001	11.340 0.001	SPITZER (IRAC)
55772.33	59.33	12.109 0.001	11.378 0.001	SPITZER (IRAC)
55779.12	66.12	12.295 0.001	11.432 0.001	SPITZER (IRAC)
55785.60	72.60	12.504 0.001	11.498 0.001	SPITZER (IRAC)
55798.28	85.28	12.837 0.002	11.665 0.002	SPITZER (IRAC)
55964.14	251.14	14.300 0.002	13.280 0.002	SPITZER (IRAC)
56026.63	313.63	15.536 0.007	14.280 0.003	SPITZER (IRAC)
56104.23	391.23	17.025 0.012	15.507 0.005	SPITZER (IRAC)
56136.41	423.41	17.337 0.014	15.988 0.006	SPITZER (IRAC)
56168.69	455.69	17.581 0.014	16.241 0.008	SPITZER (IRAC)
56337.59	624.59	18.517 0.083	17.537 0.056	SPITZER (IRAC)
56360.27	647.27	18.675 0.045	17.663 0.030	SPITZER (IRAC)
56477.83	764.83	18.833 0.047	18.047 0.039	SPITZER (IRAC)
56742.28	1029.28	...	18.506 0.091	SPITZER (IRAC)
56742.30	1029.30	...	18.410 0.075	SPITZER (IRAC)
56771.67	1058.67	18.858 0.077	18.543 0.070	SPITZER (IRAC)
56773.84	1060.84	...	18.364 0.058	SPITZER (IRAC)

Table 8. List of late-time (100-415 days) optical and NIR spectroscopic observations.

JD (+2400000) (d)	Phase (d)	Grism	Range (Å)	Resolution	Resolution (Å)	Telescope (Instrument)
55821.33	108.33	b200	3300-8700	...	12.0	CA-2.2m (CAFOS)
55821.33	108.33	r200	6300-10500	...	12.0	CA-2.2m (CAFOS)
55828.35	115.35	R300B	3200-5300	...	4.1	WHT (ISIS)
55828.35	115.35	R158R	5300-10000	...	7.7	WHT (ISIS)
55830.25	117.25	Grism 4	3500-8450	292	19.9	AS 1.82m (AFOSC)
55830.28	117.28	Grism 2	3720-10200	191	37.6	AS 1.82m (AFOSC)
55835.25	122.25	Grism 4	3500-8450	292	19.9	AS 1.82m (AFOSC)
55864.65	151.65	Grism 4	3500-8450	292	19.9	AS 1.82m (AFOSC)
55867.71	154.71	g200	4900-9900	...	12.0	CA-2.2m (CAFOS)
55893.76	180.76	Grism 3	3200-6700	345	12.4	NOT (ALFOSC)
55897.76	184.76	Grism 5	5000-10250	415	16.8	NOT (ALFOSC)
55911.20	198.20	zJ	8900-15100	700	...	WHT (LIRIS)
55914.70	201.70	R300B	3200-5300	...	8.2	WHT (ISIS)
55914.70	201.70	R158R	5300-10000	...	15.4	WHT (ISIS)
55918.69	205.69	HK	14000-25000	333	...	TNG (NICS)
55941.72	228.72	R150V	4000-9500	...	12.9	INT (IDS)
55942.73	229.73	R150V	4000-9500	...	12.9	INT (IDS)
55944.75	231.75	R150V	4000-9500	...	12.9	INT (IDS)
55951.64	238.64	Grism 4	3200-9100	355	16.2	NOT (ALFOSC)
55998.68	285.68	r200	6300-10500	...	12.0	CA-2.2m (CAFOS)
56002.58	289.58	Grism 4	3200-9100	355	16.2	NOT (ALFOSC)
56005.62	292.62	Grism 4	3200-9100	355	16.2	NOT (ALFOSC)
56006.60	293.60	Grism 4	3200-9100	355	16.2	NOT (ALFOSC)
56013.14	300.14	R600B	3680-5300	...	5.7	WHT (ISIS)
56013.14	300.14	R316R	5756-8850	...	3.0	WHT (ISIS)
56071.56	358.56	R500B	3440-7600	322	15.0	GTC (OSIRIS)
56072.61	359.61	R500R	4800-10000	352	20.8	GTC (OSIRIS)
56128.47	415.47	R300B	3600-7000	270	16.7	GTC (OSIRIS)

Table 9. Pseudo-bolometric 3-400 days UV to MIR lightcurve for SN 2011dh calculated from spectroscopic and photometric data with a 1-day sampling between 3 and 50 days and a 5-day sampling between 50 and 400 days. Random errors are given in the first parentheses and systematic lower and upper errors (arising from the distance and extinction) respectively in the second parentheses.

JD (+2400000) (d)	Phase (d)	L (log erg s^{-1})	JD (+2400000) (d)	Phase (d)	L (log erg s^{-1})
55717.00	4.00	41.464 (0.001) (0.098,0.186)	55823.00	110.00	41.244 (0.002) (0.094,0.164)
55718.00	5.00	41.552 (0.001) (0.097,0.181)	55828.00	115.00	41.204 (0.002) (0.094,0.164)
55719.00	6.00	41.653 (0.001) (0.097,0.179)	55833.00	120.00	41.163 (0.002) (0.094,0.164)
55720.00	7.00	41.747 (0.001) (0.097,0.178)	55838.00	125.00	41.121 (0.002) (0.094,0.164)
55721.00	8.00	41.835 (0.001) (0.097,0.178)	55843.00	130.00	41.078 (0.002) (0.094,0.164)
55722.00	9.00	41.909 (0.001) (0.097,0.178)	55848.00	135.00	41.033 (0.002) (0.094,0.165)
55723.00	10.00	41.969 (0.001) (0.097,0.177)	55853.00	140.00	40.990 (0.002) (0.094,0.165)
55724.00	11.00	42.018 (0.001) (0.097,0.176)	55858.00	145.00	40.948 (0.002) (0.094,0.165)
55725.00	12.00	42.057 (0.001) (0.097,0.176)	55863.00	150.00	40.906 (0.002) (0.094,0.165)
55726.00	13.00	42.089 (0.001) (0.096,0.175)	55868.00	155.00	40.863 (0.002) (0.094,0.165)
55727.00	14.00	42.117 (0.001) (0.096,0.174)	55873.00	160.00	40.818 (0.002) (0.094,0.165)
55728.00	15.00	42.142 (0.001) (0.096,0.174)	55878.00	165.00	40.773 (0.002) (0.094,0.164)
55729.00	16.00	42.163 (0.001) (0.096,0.173)	55883.00	170.00	40.728 (0.002) (0.094,0.164)
55730.00	17.00	42.182 (0.001) (0.096,0.173)	55888.00	175.00	40.683 (0.002) (0.094,0.164)
55731.00	18.00	42.197 (0.001) (0.096,0.173)	55893.00	180.00	40.639 (0.001) (0.094,0.164)
55732.00	19.00	42.208 (0.001) (0.096,0.172)	55898.00	185.00	40.597 (0.001) (0.094,0.164)
55733.00	20.00	42.214 (0.001) (0.096,0.172)	55903.00	190.00	40.555 (0.001) (0.094,0.164)
55734.00	21.00	42.215 (0.001) (0.096,0.171)	55908.00	195.00	40.516 (0.001) (0.094,0.164)
55735.00	22.00	42.211 (0.001) (0.095,0.171)	55913.00	200.00	40.477 (0.001) (0.094,0.164)
55736.00	23.00	42.200 (0.001) (0.095,0.170)	55918.00	205.00	40.438 (0.001) (0.094,0.164)
55737.00	24.00	42.184 (0.001) (0.095,0.168)	55923.00	210.00	40.403 (0.001) (0.094,0.164)
55738.00	25.00	42.164 (0.001) (0.095,0.167)	55928.00	215.00	40.368 (0.001) (0.094,0.164)
55739.00	26.00	42.141 (0.001) (0.094,0.166)	55933.00	220.00	40.334 (0.001) (0.094,0.164)
55740.00	27.00	42.116 (0.001) (0.094,0.165)	55938.00	225.00	40.300 (0.001) (0.094,0.164)
55741.00	28.00	42.090 (0.001) (0.094,0.164)	55943.00	230.00	40.267 (0.001) (0.094,0.164)
55742.00	29.00	42.064 (0.001) (0.094,0.163)	55948.00	235.00	40.235 (0.001) (0.094,0.163)
55743.00	30.00	42.039 (0.001) (0.094,0.162)	55953.00	240.00	40.204 (0.001) (0.094,0.163)
55744.00	31.00	42.016 (0.001) (0.093,0.162)	55958.00	245.00	40.172 (0.001) (0.094,0.163)
55745.00	32.00	41.995 (0.001) (0.093,0.161)	55963.00	250.00	40.139 (0.001) (0.094,0.163)
55746.00	33.00	41.976 (0.001) (0.093,0.161)	55968.00	255.00	40.106 (0.001) (0.094,0.163)
55747.00	34.00	41.959 (0.001) (0.093,0.160)	55973.00	260.00	40.072 (0.001) (0.094,0.163)
55748.00	35.00	41.942 (0.001) (0.093,0.160)	55978.00	265.00	40.039 (0.002) (0.094,0.163)
55749.00	36.00	41.927 (0.001) (0.093,0.160)	55983.00	270.00	40.005 (0.002) (0.094,0.163)
55750.00	37.00	41.913 (0.001) (0.093,0.159)	55988.00	275.00	39.972 (0.002) (0.094,0.163)
55751.00	38.00	41.899 (0.001) (0.093,0.159)	55993.00	280.00	39.939 (0.002) (0.094,0.163)
55752.00	39.00	41.885 (0.001) (0.093,0.159)	55998.00	285.00	39.906 (0.002) (0.094,0.163)
55753.00	40.00	41.873 (0.001) (0.093,0.159)	56003.00	290.00	39.872 (0.002) (0.094,0.163)
55754.00	41.00	41.859 (0.001) (0.093,0.159)	56008.00	295.00	39.838 (0.002) (0.094,0.163)
55755.00	42.00	41.846 (0.001) (0.093,0.159)	56013.00	300.00	39.804 (0.002) (0.094,0.163)
55756.00	43.00	41.834 (0.001) (0.093,0.159)	56018.00	305.00	39.770 (0.002) (0.094,0.163)
55757.00	44.00	41.822 (0.002) (0.093,0.159)	56023.00	310.00	39.737 (0.002) (0.094,0.163)
55758.00	45.00	41.811 (0.002) (0.093,0.159)	56028.00	315.00	39.703 (0.002) (0.094,0.163)
55759.00	46.00	41.800 (0.001) (0.093,0.159)	56033.00	320.00	39.670 (0.002) (0.094,0.163)
55760.00	47.00	41.790 (0.001) (0.093,0.159)	56038.00	325.00	39.638 (0.002) (0.094,0.163)
55761.00	48.00	41.781 (0.001) (0.093,0.159)	56043.00	330.00	39.605 (0.002) (0.094,0.163)
55762.00	49.00	41.771 (0.002) (0.093,0.159)	56048.00	335.00	39.572 (0.002) (0.094,0.163)
55763.00	50.00	41.762 (0.002) (0.093,0.159)	56053.00	340.00	39.540 (0.002) (0.094,0.163)
55768.00	55.00	41.715 (0.002) (0.093,0.159)	56058.00	345.00	39.508 (0.002) (0.094,0.163)
55773.00	60.00	41.669 (0.002) (0.093,0.159)	56063.00	350.00	39.476 (0.002) (0.094,0.163)
55778.00	65.00	41.627 (0.002) (0.093,0.160)	56068.00	355.00	39.445 (0.002) (0.094,0.163)
55783.00	70.00	41.585 (0.002) (0.093,0.160)	56073.00	360.00	39.413 (0.002) (0.094,0.163)
55788.00	75.00	41.544 (0.002) (0.093,0.161)	56078.00	365.00	39.382 (0.002) (0.094,0.163)
55793.00	80.00	41.501 (0.002) (0.093,0.162)	56083.00	370.00	39.351 (0.002) (0.094,0.163)
55798.00	85.00	41.458 (0.002) (0.094,0.162)	56088.00	375.00	39.320 (0.002) (0.094,0.163)
55803.00	90.00	41.415 (0.002) (0.094,0.162)	56093.00	380.00	39.289 (0.002) (0.094,0.163)
55808.00	95.00	41.372 (0.002) (0.094,0.163)	56098.00	385.00	39.255 (0.002) (0.094,0.163)
55813.00	100.00	41.330 (0.002) (0.094,0.163)	56103.00	390.00	39.220 (0.002) (0.094,0.163)
55818.00	105.00	41.287 (0.002) (0.094,0.163)	56108.00	395.00	39.186 (0.002) (0.094,0.164)